
Electronic Thesis and Dissertation Repository

4-23-2019 10:00 AM

High Molecular-Weight Hyaluronan Prevents Basal Cell Carcinoma Via Promoting Apoptosis In Cancer-Initiating Adult Stem Cells

Violet Liu, *The University of Western Ontario*

Supervisor: Turley, Eva, *London Regional Cancer Program, Lawson Health Research Institute, London, ON, Canada*

A thesis submitted in partial fulfillment of the requirements for the Master of Science degree in Biochemistry

© Violet Liu 2019

Follow this and additional works at: <https://ir.lib.uwo.ca/etd>

 Part of the [Biochemistry Commons](#)

Recommended Citation

Liu, Violet, "High Molecular-Weight Hyaluronan Prevents Basal Cell Carcinoma Via Promoting Apoptosis In Cancer-Initiating Adult Stem Cells" (2019). *Electronic Thesis and Dissertation Repository*. 6186.
<https://ir.lib.uwo.ca/etd/6186>

This Dissertation/Thesis is brought to you for free and open access by Scholarship@Western. It has been accepted for inclusion in Electronic Thesis and Dissertation Repository by an authorized administrator of Scholarship@Western. For more information, please contact wlsadmin@uwo.ca.

Abstract

Basal cell carcinoma (BCC), a keratinocyte cancer, is the most common human neoplasm worldwide. Although rarely metastatic, BCC is associated with high morbidity rates with globally rising incidence rates. Accompanying the increase in newly diagnosed cases, the societal cost for BCC treatment in Canada is also expected to inflate, exceeding over \$900 million/year by 2031. Chronic UVB exposure has been identified as the primary carcinogen that causes activating mutations in the hedgehog signaling pathway. However, there are no effective preventative methods against BCC, since meta-analyses report sunscreen application does not reduce BCC in compliant patients. The native high molecular-weight hyaluronan (HMW-HA) was recently reported to confer tumor resistance to carcinogens including UVB in naked mole-rats (*Heterocephalus glaber*). We therefore prepared phosphatidylethanolamine-linked HMW-HA polymers (HA-PE) for topical application in UVB-induced, BCC susceptible *Ptch*^{+/*LacZ*}/*Hr*^{-/-} mice. HA-PE formed detectable HA coats around epidermal and hair follicle keratinocytes, and prevented histologically-detectable keratinocyte tumor formation, verified by reduced *Ptch1* promoter activity indicating oncogenic hedgehog pathway shutdown. Further evidence of signaling inactivation by HA-PE includes strong suppression of the expression of hedgehog pathway gene targets in both the epidermis and hair follicles. Surprisingly, HA-PE did not prevent UVB/ROS-induced DNA damage. However, HA-PE promoted quiescence in the hair follicle bulge and selective apoptosis of K15⁺ stem cells that are BCC initiating in the *Ptch1*^{+/*LacZ*}/*Hr*^{-/-} susceptibility model. Consistent with this finding, the K15⁺ stem cells population decreased from hair follicles between 4-26 weeks of treatment. These results provide evidence of a novel mechanism for HA-mediated tumor resistance and implicate HA-PE as a promising BCC prophylactic. This knowledge will also provide a model for probing the interplay between the microenvironment and oncogenic mutations that permit or restrain tumor initiation.

Keywords

Hyaluronan, CD44, basal cell carcinoma, apoptosis, stem cell, cytokeratin 15

Co-Authorship Statement

The initial discovery and experiments related to the formulation of HWM-hyaluronan-phosphatidylethanolamine polymers (HA-PE) was accomplished by Dr. Eva Turley, Dr. Cornelia Tolg, and Dr. Jenny Ma. HA-PE is patented worldwide and most recently in the USA (patent number: *US20130059769A1*; E. Turley, WorldDiscoveries), which provided the foundation of this research project. The experiments and analysis related to animal studies (including genotyping, treatment and collection of skin tissue samples) was conducted by Katelyn Cousteils, the previous M.Sc. student leading this research project. The immunohistochemistry experiments and analysis of Ki67 expression in the interfollicular epidermis of susceptible mice following 26 of irradiation were also conducted by Katelyn Cousteils, and reported in her dissertation in contribution to a degree in Master of Science. In this study, the author conducted the analysis of Ki67 expression in the hair follicles of susceptible mice following 4 weeks of irradiation. Sectioning and fixation of all paraffin-embedded tissue samples in this study were conducted by Carl Postenka. Yiyong Liu assisted in the technical replicate quantification process of GLI1, cyclin D1, and vertical lineage tracing of γ -H2AX. All other experiments and analyses described in this study were performed by the author.

Acknowledgments

First and foremost, I would like to thank Dr. Eva Turley for this wonderful opportunity to explore my research interests. Your enthusiasm and creativity are truly inspiring, and I am indebted to you for your guidance in science and beyond. This project would not have been possible without you.

I also wish to express gratitude to my committee members, Dr. Paul Walton and Dr. Murray Junop. Thank you for your continuous guidance throughout the research process. Your valuable inputs and insights are crucial to the completion of this dissertation.

To all the past and present members of the Turley Lab: Conny, Jenny, Khandakar, Kitty, Joselia, Tony, Stephanie, Alaa, Elizabeth, and Hannah, thank you for making my experience here so wonderful. I have thoroughly enjoyed my time here in the lab and I have each of you to thank for this memorable experience. Special thanks to Conny, for always willing to share her expertise and experience with me, and for laughs shared in between experiments and during lunch. To Jenny, thank you so much for supporting and watching out for me throughout my time here in the Turley lab, I miss you already.

On a personal note, my deepest gratitude to my family, friends, and boyfriend for all their unwavering support throughout this process. To my parents, thank you for your endless encouragement along the way. Any accomplishment I achieve pale in comparison to your love.

Table of Contents

Abstract.....	i
Co-Authorship Statement.....	ii
Acknowledgments.....	iii
Table of Contents.....	iv
List of Tables.....	vii
List of Figures.....	viii
List of Appendices.....	x
List of Abbreviations.....	xi
1 Introduction.....	1
1.1 Basal cell carcinoma.....	1
1.1.1 Molecular mechanisms of BCC tumorigenesis.....	2
1.2 Pathophysiology of BCC.....	4
1.2.1 Anatomy of skin.....	4
1.2.2 Cancer-initiating cells in BCC.....	7
1.2.3 UV radiation and DNA damage.....	8
1.3 Naked mole-rats in cancer research.....	9
1.4 Hyaluronan.....	10
1.4.1 HA receptors and signaling.....	12
1.4.2 The hyaluronome in carcinogenesis.....	13
1.4.3 Phosphatidylethanolamine-linked high molecular-weight hyaluronan.....	15
1.5 Animal models in BCC research.....	16
1.6 Hypothesis and objectives.....	17
2 Materials and methods.....	19
2.1 Animal studies.....	19

2.2 Immunohistochemistry	20
2.2.1 Image analysis.....	21
2.2.2 Vertical lineage tracing.....	21
2.3 Immunofluorescence and image analysis	21
2.4 Detection of HA in tissue sections and analysis	24
2.5 RT-qPCR.....	24
2.5.1 Total RNA extraction from tissue.....	24
2.5.2 In vitro reverse transcription.....	25
2.5.3 PCR reactions and analysis.....	25
2.5.4 Real-time PCR reactions and analysis	26
2.6 Enzyme-linked immunosorbent assays.....	28
2.6.1 DNA extraction from tissue.....	28
2.6.2 8-oxo-2'-deoxyguanosine ELISA.....	28
2.6.3 Cyclobutane pyrimidine dimer ELISA	29
2.7 Terminal deoxynucleotidyl transferase dUTP nick end labeling (TUNEL) assay.....	30
2.8 Hyaluronidase activity ELISA-like assay.....	31
2.9 HA size determination by agarose gel	32
2.9.1 HA isolation from tissue.....	32
2.9.2 Gel electrophoresis and visualization	33
2.10 Statistical analyses	34
3 Results.....	35
3.1 HA-PE application promotes epidermal HA accumulation.....	35
3.2 Suppressive effects of HA-PE on sonic hedgehog signaling.....	38
3.3 HA- PE restricts cell cycle progression in susceptible mice.....	42
3.4 CD44 and RHAMM expression in HA-PE treated skin.....	45

3.5	Effects of HA-PE on NF-κB signaling	48
3.6	Keratinocytes are not protected from DNA damage by HA-PE in susceptible mice.....	50
3.7	HA-PE application promotes selective apoptosis in hair follicles.....	53
3.8	Immunohistochemical analysis of UVB-induced BCC tumors in <i>Ptch</i> ^{+/<i>LacZ</i>/<i>Hr</i>^{-/-} mice}	58
4	Discussion	61
4.1	HA-PE phenocopies the cancer-resistant naked mole-rat to prevent carcinogenesis in susceptible mice	61
4.2	HA-PE mediated suppression is not orchestrated through canonical NF-κB signaling.....	64
4.3	HA-PE promotes apoptosis of DNA-damaged K15 ⁺ cancer-initiating stem cells in hair follicles	65
4.4	Future directions	68
5	Conclusions	70
	References or Bibliography	71
	Appendix A: Supplemental materials	89
	Curriculum Vitae	91
	Muhan Liu.....	91

List of Tables

Table 1: Antibodies and buffers used in immunohistochemistry and immunofluorescence of paraffin-embedded tissue sections.....	23
Table 2: Primers used in RT-qPCR and RT-PCR.....	27

List of Figures

Figure 1: Sonic hedgehog signaling pathway.....	3
Figure 2: Anatomy of the human skin.....	6
Figure 3: Detection of HA content in the interfollicular epidermis and hair follicles of UVB-exposed mice.....	36
Figure 4: Effects of topical HA-PE administration on hyaluronidase expression and activity.....	37
Figure 5: Suppressive effect of HA-PE application on UVB-induced BCC initiation using E.coli LacZ expression as a marker in susceptible mice.....	40
Figure 6: HA-PE prevents oncogenic sonic hedgehog activation in UVB-exposed murine epidermis.....	41
Figure 7: HA-PE promotes keratinocyte quiescence.....	43
Figure 8: Immunohistochemistry analysis of Ki67 after HA-PE application.....	44
Figure 9: CD44 and RHAMM expression in UVB-exposed epidermis following HA-PE application.....	46
Figure 10: Alterations in HA receptor mRNA expression after HA-PE treatment.....	47
Figure 11: NF κ B activation in UVB-exposed epidermis.....	49
Figure 12: HA-PE does not alter the double-stranded breaks in UVB-exposed epidermis.....	51
Figure 13: ROS- and UVB-induced DNA damages are not altered by HA-PE application.....	52
Figure 14: HA-PE reduces pro-survival BCL2 expression in the interfollicular epidermis and hair follicles.....	54

Figure 15: HA-PE enhances apoptosis in the outer root sheath and bulge region of hair follicles.....55

Figure 16: HA-PE enhances apoptosis in K15+ adult stem cells in hair follicles.57

Figure 17: Immunohistochemistry analyses of UVB-induced BCC tumors..60

List of Appendices

Appendix A: Animal studies.....	89
Appendix B: Supplemental materials	89

List of Abbreviations

8-oxo-dG	8-oxo-2'-deoxyguanoine
BCA	Bicinchoninic acid assay
BCC	Basal cell carcinoma
BSA	Bovine serum albumin
BuSC	Bulge stem cell
CD44s	Standard form of CD44
CD44v	Variant isoforms of CD44
CPD	Cyclobutane pyrimidine dimer
DAB	3,3'-diaminobenzidine
DSBs	Double-stranded breaks
dsDNA	Double-stranded DNA
ECI	Early contact inhibition
HMW-HA	Extremely high molecular-weight hyaluronan
GAG	Glycosaminoglycan
GLI	Glioma-associated oncogene
HA	Hyaluronan
HA-PE	Hyaluronan-phosphatidylethanolamine
HARE	Human hyaluronan receptor for endocytosis
HAS	Hyaluronan synthase
HMW-HA	High molecular-weight hyaluronan
Hr	Hairless
HYAL	Hyaluronidase
IFE	Interfollicular epidermis
IRS	Inner root sheath
K14	Cytokeratin-14
K15	Cytokeratin-15
LMW-HA	Low molecular-weight hyaluronan
NGS	Next generation deep sequencing

NF- κ B	nuclear factor kappa-light-chain-enhancer of activated B cells
ORS	Outer root sheath
PBS	Phosphate-buffered saline
PTCH	Patched
RHAMM	Receptor for hyaluronan-mediated motility
ROS	Reactive oxygen species
SC	Stem cell
SCC	Squamous cell carcinoma
SEM	Standard error of the mean
SHH	Sonic hedgehog
SMA	Smooth Muscle Actin
SMO	Smoothened
ssDNA	Single-stranded DNA
TAE	Tris-acetate-EDTA
TBS	Tris-buffered saline
TE	Tris-EDTA
TLR	Toll-like receptors
TUNEL	Terminal deoxynucleotidyl transferase dUTP nick end labelling
UV	ultraviolet
β -gal	β -galactosidase

Chapter 1

1 Introduction

1.1 Basal cell carcinoma

Basal cell carcinoma (BCCs) are locally aggressive keratinocyte tumors with a recurrence rate of 50% in 5 years following diagnosis. BCC is the most common form of neoplasm in adults^{1,2,3}, accounting for 70% of all keratinocyte tumors and 90% of all malignant skin diseases. Chronic exposure to ultraviolet (UV) radiation has been identified as the primary risk factor for BCC⁴. Historically, BCC occurs more frequently in fair-skinned populations and in males due to increased sun-exposure in workplaces⁵⁻⁹. However, this regional and sex difference is decreasing due to steady depletion of the protective ozone layer and enhanced UV exposure in all populations¹⁰⁻¹². Although BCC was originally considered as a malignancy of the older population (>65 years of age), epidemiological studies report a dramatic increase in BCC incidence in younger populations during the last decade due to tanning bed usage^{5-7,12-14}. BCC rarely metastasizes, but is locally aggressive and causes dermal tissue destruction, thus resulting in high morbidity rates¹⁵. Moreover, a history of non-melanoma skin cancer is associated with increased risk of developing secondary tumors prone to metastasis, such as breast, prostate and colon cancers¹⁶⁻¹⁸. Currently, societal cost for BCC treatment and related expenses in Canada is approximately \$34.6 million (www.iwh.on.ca) and is expected to exceed over \$900 million by 2031 (Canadian Partnership Against Cancer, 2010).

Common treatments of BCC include non-specific surgical removal of tumors, application of oncogenic pathway inhibitors, and radiotherapy^{19,20}. However, surgical excisions often contribute to patient morbidity as they are visibly scarring, while inhibitor treatment is associated with increased risk of developing secondary low-grade keratinocyte tumors^{20,21}. Moreover, multiple tumor recurrences are common following surgical excisions and targeted therapy (up to 7% within 5 years)²²⁻²⁴, contributing to the accumulation of healthcare cost and deterioration of quality of life. In addition, radiotherapy is commonly

recommended as a palliative treatment in elderly patients²⁵, and is associated with higher cost and recurrence (85% within 3 years)^{26,27}.

1.1.1 *Molecular mechanisms of BCC tumorigenesis*

Advancement in the past decade has identified aberrant activation of the sonic hedgehog signaling as the primary cause of BCC pathogenesis^{28,29,30-32}. Hedgehog signaling plays a pivotal role in embryogenesis through orchestrating cell-cell communication of the epidermis and neural patterning³¹. During morphogenesis, sonic hedgehog signaling promotes proliferation, differentiation, and vascularization³³, all of which are employed by tumor cells for growth and metastasis. In post-natal skin, hedgehog signaling promotes active growth of hair (anagen) and is required for hair follicle-resident multipotent stem cell proliferation^{29,34}. The pathway is activated when the extracellular ligand sonic hedgehog (SHH) binds and inhibits the transmembrane receptor Patched1 (PTCH1), triggering rapid endocytosis of the PTCH-SHH complex^{33,35}. The internalization of PTCH1 releases its suppression of Smoothed (SMO), cumulating in the activation and nuclear translocation of the GLI family of transcriptional factors (Figure 1). Specifically, GLI2 and GLI3 accumulate in the nucleus and induce target gene expression in the presence of SHH. In contrast, GLI1 expression can only be induced by activated GLI2/3 and is dependent on active sonic hedgehog signaling. Thus, GLI1 is a reliable molecular marker of hedgehog activation, and its overexpression is characteristic of sporadic BCC²⁹. Other target genes of the sonic hedgehog pathway include *Ptch1*, a negative regulator that dampens the signal transduction of this pathway, and various regulators of cell cycle and apoptosis, such as *Bcl-2* and *Ccnd1/2*.^{29,36} Since PTCH1 and GLI1 are both regulators and target genes of hedgehog signaling, they are often used as markers to examine hedgehog signaling activation³⁷⁻³⁹.

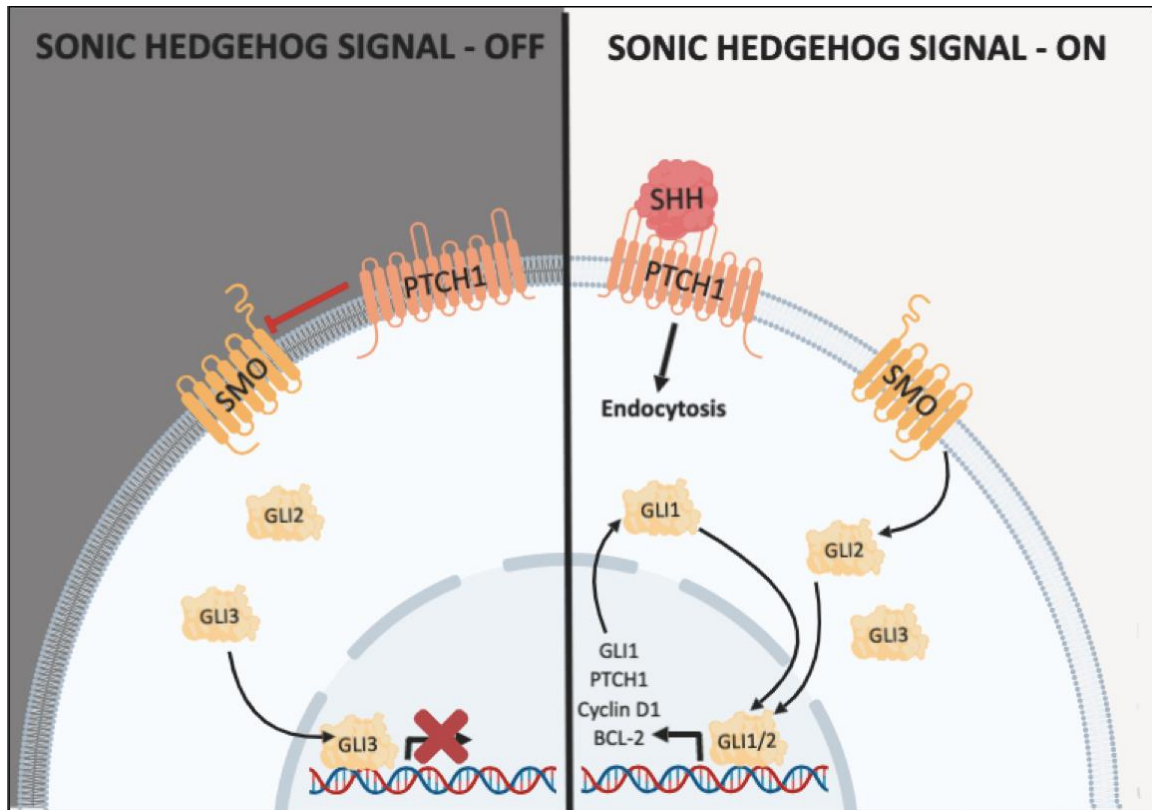


Figure 1: Sonic hedgehog signaling pathway. When the sonic hedgehog ligand (SHH) is absent, the pathway is inactivated. Tumor-suppressor Patched 1 (PTCH1) inhibits downstream Smoothed (SMO). However, PTCH1 is inactivated with SHH binding, allowing SMO to activate the transcriptional factor family GLI to induce target gene expression. GLI1 expression relies on GLI2/3 activation, therefore its expression level is often used as an indicator of the overall signaling activity in the sonic hedgehog pathway.

Pathogenic activation of the sonic hedgehog pathway can occur through sustaining inactivation mutations in *Ptch1*, thus abolishing its inhibition of SMO. Genetic studies report over 90% of sporadic BCC patients sustain *Ptch1* mutations, marking *Ptch1* as the most commonly disrupted gene underlying BCC tumorigenesis^{40,41,42}. *Ptch1* in BCC patients also contain a high level of UV-signature mutations, suggesting chronic exposure to environmental UV as the primary risk factor in sporadic BCC⁴³. Mutations in other genes of the pathway can also lead to BCC pathogenesis and additional neoplasms. For instance, ligand-independent activating mutations in *Smo* have been found in 6-21% of sporadic BCCs^{29,42}, while *Gli2* overexpression induces BCC tumorigenesis in UVB-exposed murine models⁴⁴.

In addition, sonic hedgehog signaling is reported to regulate stem cell lineage maintenance and cancer stem cell renewal *in vivo*^{45,46}. Overexpression of SHH in post-natal mice resulted in increased stem cells and atypical proliferation, whereas blockage abolished this effect^{46,47}. Clinical and molecular evidence suggest BCC carcinogenesis is preceded by inappropriate hyperactivation of the hedgehog pathway, which normally regulates stem cell renewal, proliferation, and appropriate hair follicle cycling in post-natal epidermis^{33,46,48}. Since BCC is a malignancy that originates from epidermal and hair follicle stem cells, investigating sonic hedgehog signaling in the epidermal stem cell niche is pivotal to understanding BCC pathogenesis.

1.2 Pathophysiology of BCC

1.2.1 Anatomy of skin

In human, the skin is divided into three layers: the epidermis, dermis, and hypodermis. The epidermis is further separated into distinct layers based on keratinocyte differentiation. The basal layer (stratum basale) contains progenitor cells that rapidly proliferate, giving rise to differentiated keratinocytes in the suprabasal layers (stratum corneum, stratum lucidum, stratum granulosum, and stratum spinosum)³³. New daughter keratinocytes continuously migrate upward, which is terminated at the stratum corneum where matured keratinocytes keratinize and undergo apoptosis (Figure 2).

Similar to the human integument system, murine epidermis and related appendages are renewed independently from distinct niches of adult stem cells^{49,50}. Rapid turnover of the interfollicular epidermis (IFE) is maintained by epidermal stem cells in stratum basale through mitotic division. In contrast, multipotent cytokeratin-15-expressing (K15) adult stem cells residing in the bulge region and outer root sheath (ORS) of hair follicles are responsible for the renewal of the follicles and associated glands^{51,52}. These bulge stem cells (BuSCs) are slow-cycling and are quiescent until activated by sonic hedgehog signaling^{29,34,53,54}. Daughter cells from BuSC give rise to transiently-amplifying progenitor cells, which then rapidly divide symmetrically to renew multiple compartments of the hair follicle, such as the inner root sheath (IRS) and hair shaft (Figure 2). Transiently-amplifying cells in the hair matrix are defined by their more limited plasticity and proliferative properties than BuSCs⁴⁸. Deprivation of sonic hedgehog signaling results in BuSC quiescence and interferes with appropriate progression through hair cycle, since BuSCs proliferation is essential for anagen^{55,56}. As observed after administration of hedgehog inhibitors such as vismodegib and sonidegib, loss of sonic hedgehog signals prevents BuSC proliferation and telogen-to-anagen transition, resulting in alopecia of human patients⁵⁷. Interestingly, neural-derived sonic hedgehog signal also triggers transient participation of BuSCs in wound healing by stimulating their migration upward into the epidermis, where they differentiate into multipotent progenitor cells to renew the IFE^{49,54}.

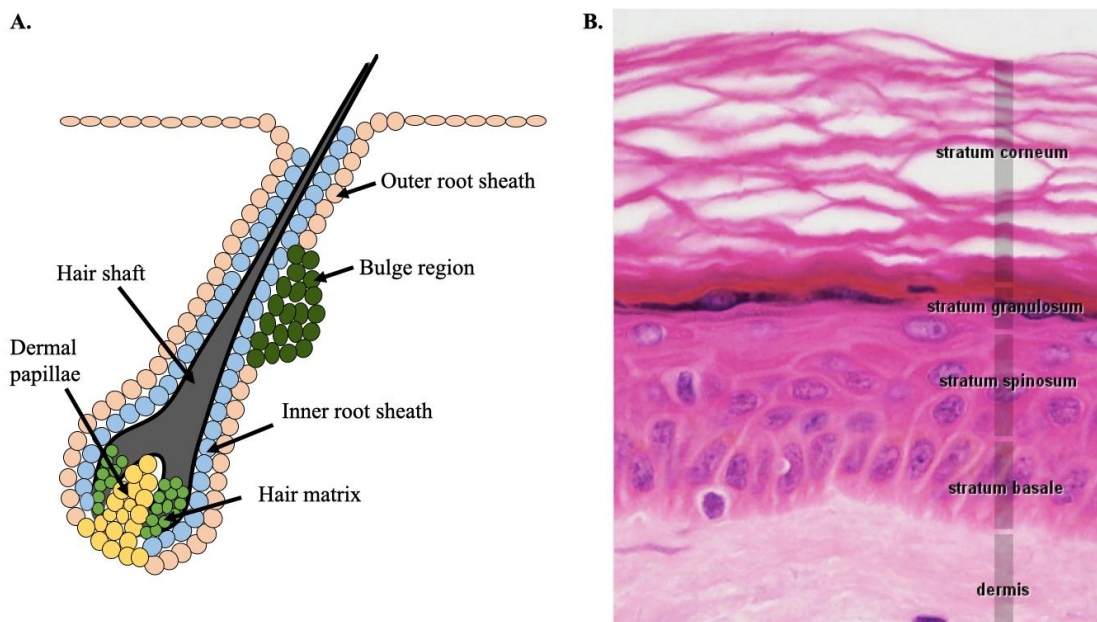


Figure 2: Anatomy of the human skin. **A.** Hair follicle structure in human. Multipotent adult stem cells reside within the bulge (green), which is a specialized portion of the outer root sheath (light orange). Upon stimulation by sonic hedgehog signaling, adult stem cells proliferate and daughter cells constitute the outer root sheath, eventually differentiating into transiently-amplifying cells residing within the hair matrix (light green), which flanks the dermal papillae (yellow). These multipotent progenitors then give rise to the hair shaft (grey) and the inner root sheath (blue). **B.** Layers of the epidermis. Interfollicular epidermis renewal depends on the mitotic division of progenitor cells in stratum basale, with newly differentiated keratinocytes in the suprabasal layers (stratum spinosum, granulosum, lucidum, and corneum). The figure is adapted from Blue Histology, University of Western Australia (<http://www.lab.anhb.uwa.edu.au/mb140/>).

1.2.2 Cancer-initiating cells in BCC

Previous *in vivo* studies report BCC commonly arise from SCs residing within the hair follicles and the IFE. Aberrant activation of sonic hedgehog signaling causes SCs to enter a hyperproliferative state and result in neoplastic outgrowths^{58–61}, whereas its inhibition reduces tumor growth in susceptible mouse models and humans. However, the plasticity of epithelial SCs adds an additional layer of complexity to the cell origin and epidermal compartment of BCC initiation. For example, constitutive sonic hedgehog activation driven by *Ptch1* loss produces micronodular BCCs arising from the bulge and ORS regions in hair follicles. Cell fate tracking of IR-induced BCCs in *Ptch*^{+/-} mice demonstrate these keratinocyte tumors originate exclusively from the K15⁺ BuSCs^{58,60,62}, or from their progeny in follicles⁴⁴. In contrast, hedgehog dysregulation resulting from overexpression of downstream components, such as mutant SMO (*SmoM2*) and GLI2 (*GLI2*ΔN), result in BCC tumors arising from the IFE^{59,61}. The multipotent K14-expressing adult stem cells in stratum basale give rise to BCCs associated with the epidermis. The consensus in the field for this discrepancy is that the loss of tumor-inhibitor PTCH1 and the overexpression of mutant SMO may produce different biological effects^{58,59}. The surprising resistance against SMO/GLI2-driven tumorigenesis in follicles also suggests the stem cell niche may act as a key regulator of the tumorigenic potential of BuSCs in BCC initiation^{58,59}.

Clinical and genetic studies conclude *Ptch1* inactivation is the most prominent oncogenic driver mutation in nodular and micronodular BCC, which are the most prevalent and high-risk histopathological subtype in sporadic BCC patients respectively^{63,64}. These tumors are characterized by cell nests encircled by scant stroma that is prominently separated from the surrounding tissue^{63–65}, consistent with tumors arising from the hair follicles due to *Ptch1* loss. In contrast, superficial BCC originates from the IFE in human patients⁶⁴, consistent with tumors driven by mutant SMO and GLI2 overexpression in murine models^{59,61}. Since over 90% of sporadic BCC patients contain *Ptch1* inactivating mutation^{40,43,66}, focus has been placed on the role of PTCH1 inactivation and downstream consequences in the context of BCC initiation.

1.2.3 *UV radiation and DNA damage*

Neoplastic formation induced by chronic UV exposure is widely accepted as the predominant paradigm in skin carcinogenesis⁶⁷⁻⁷¹. A strong causal link exists between prolonged UV radiation and BCC, as epidemiological and molecular studies report approximately 90% of non-melanoma skin cancer are associated with UV exposure^{8,43, 72}. UV radiation can introduce inactivating mutations in tumor-suppressors and inappropriately activate oncogenes, resulting in aberrant proliferation and evasion of apoptosis in keratinocytes sustaining these mutations. UVB (290 - 320nm) is the most carcinogenic UV radiation^{67,69}. Prolonged UVB exposure results in direct DNA damages in the form of cyclobutane pyrimidine dimers (CPD), and is associated with the accumulation of double-stranded breaks (DSBs) in keratinocytes due to the collapse of replication forks^{67,69}. The bulky photodimers interfere with the spatial structure of DNA and proper replication, whereas DSBs possess greater risks of losing of genetic materials if not repaired effectively. Moreover, evidence suggests chronic UVB exposure augments skin carcinogenesis through altering immune cell function in the tumor microenvironment, thus promoting sustained inflammatory response and evasion of immune surveillance^{69,73-75}. Constant production of reactive oxygen species (ROS) by recruited immune cells further contributes to neoplastic initiation in a re-modeled microenvironment⁷⁶. Since the epidermis is constantly exposed to environmental UVB, adult stem cells in the stratum basale and hair follicles pose as vulnerable targets to damage and carcinogenesis. Next-generation deep sequencing (NGS) demonstrates that BCC contains a high mutational load compared to metastatic cancer types, such as breast, lung, and ovarian cancers⁷⁷⁻⁷⁹. Interestingly, this high mutational load does not always affect keratinocyte tumor initiation, which is defined as the irreversible process of a normal cell in acquiring the capacity for tumor formation, commonly through oncogenic pathway activation and subsequent clonal expansion. NGS analyses detected expanded clonal patches of keratinocytes carrying driver mutations in photo-aged skin without histologically-detectable tumors⁷⁹⁻⁸³. These driver mutations, such as mutational inactivation of *TP53*, in UVB-exposed skin occur at a high frequency that is similar to many malignant cancers and appear to be under strong positive selection, yet the skin remains physiologically normal. Moreover, *in vivo* studies of human keratinocytes suggest *TP53* mutations conferring to

increased proliferative capacity are not sufficient to initiate keratinocyte tumors, as they were unable to escape the stem cell compartment within the hair follicles to initiate clonal expansion⁸⁴. The central role of DNA damage and related repair mechanisms in skin carcinogenesis is undisputed. However, this combination of experimental and genetic evidence suggests the existence of an internal barrier, such as tissue architecture or microenvironmental signal⁸⁵⁻⁸⁷, that serves as an additional barrier in preventing skin tumorigenesis originating from the follicles.

Currently, there are no effective prophylactics for UVB-induced BCC. Physicians have long recommended sun-blocks as the primary preventative method against non-melanoma cancer. However, meta-analyses and longitudinal studies report only a slight reduction in SCC occurrence, with no significant BCC reduction in compliant patients⁸⁸⁻⁹⁰. Therefore, development of preventative measures specific for BCC is imperative.

1.3 Naked mole-rats in cancer research

Recent research of cancer-resistant long-lived species yielded potential clues to preventative medicine against skin carcinogenesis. Naked mole-rats (*Heterocephalus glaber*) are long-lived rodents (> 30 years in captivity) that display extraordinary longevity comparing to mammalian species with similar body mass (i.e: house mouse, 4 years in captivity). Aside from their exceptional longevity, naked mole-rats also display surprising resistance against carcinogen-induced tumorigenesis⁹¹. Only four cases of cancer have been reported in these long-lived rodents since captivity, with no reported tumors arising from keratinocytes⁹². Seluanov *et al.* (2009) have attributed this cancer resistance to the hypersensitivity towards contact inhibition (early contact inhibition, ECI). Naked mole-rat fibroblasts do not form a confluent monolayer in culture, instead ceasing their proliferative activities upon few cell-cell contacts. ECI contributes to cancer resistance by promoting cell cycle arrest through inducing p16^{INK4A} expression⁹³.

The accumulation of epidermal high molecular-weight HA (HMW-HA) has been established as the extracellular signal that triggers ECI⁹⁴. HMW-HA accumulation is attributed to two mechanisms in naked mole-rats: enhanced synthesis (enhanced HAS2 levels) and reduced degradation (low hyaluronidase expression). Importantly, mutant fibroblast cell lines lacking the ECI phenotype (p16^{INK4A-/-}) still exhibited continuous

production of HMW-HA while wild-type fibroblasts treated with hyaluronidase displayed no ECI, therefore placing HA production and signaling upstream of p16^{INK4A}-induced cell cycle arrest. Moreover, the ECI response mediated by HMW-HA is transmitted through CD44 binding. Upon blocking CD44 with an antibody, naked mole-rat fibroblasts lost ECI and reached a higher density in culture. Transformation resistance observed in wild-type naked mole-rat fibroblasts was lost upon hyaluronidase and anti-CD44 treatments, producing anchorage-independent growth in culture. Decreased expression of p16^{INK4A} is also observed in hyaluronidase-treated fibroblasts, implicating that the ECI phenotype is modulated by HA/CD44 signaling.

Recently, HMW-HA accumulation has been reported to induce apoptosis in breast cancer cells in 2D culture⁹⁵. Overexpression of naked mole-rat HAS2 and exogenous HMW-HA treatment elevated cytoplasmic cytochrome C expression, caspase activity, ROS generation and apoptosis in breast cancer cells. This promotion of apoptosis is associated with inhibition of spheroid growth and tumor formation *in vivo*, along with downregulated gene expression involved in proliferation. CD44 expression was significantly upregulated in 2D, 3D and *in vivo* models with the elevation of HMW-HA. Taken together, this suggests the interaction between CD44 and large HA polymers mediates cancer cell apoptosis and restricts cell cycle progression as a mechanism of cancer resistance in naked mole-rats⁹³⁻⁹⁵.

1.4 Hyaluronan

Although the central role of oncogenic driver mutations in carcinogenesis is indispensable, mutations alone appear to be insufficient for tumor initiation. Instead, experimental data predict the microenvironment can permit or suppress the tumorigenic potential of mutations^{87,96,97}. The glycosaminoglycan, hyaluronan (HA), is an example of a microenvironmental agent that regulates tumor initiation and progression⁹⁸⁻¹⁰⁰. Interestingly, HA of different polymer sizes has distinctive biological functions. High molecular-weight HA (>500 kDa), such as those observed in naked mole-rats, suppress proliferation, migration, and other functions that support tumor growth^{101,102}. In contrast, low molecular-weight HA (<200 kDa; LMW-HA) promote cell proliferation and invasion, thus potentiating tumor progression¹⁰³. HMW-HA also predominates during tissue

homeostasis, while LMW-HA accumulates during wound repair and tissue remodeling processes^{100,103,104}. Thus, the bio-information of HA is encoded within its polymer size, instead of its chemical structure¹⁰⁵.

HA is an anionic, linear, non-sulphated glycosaminoglycan (GAGs) composed of repeating disaccharide units of glucuronic acid and N-acetylglucosamine. It facilitates tissue hydration via retaining large volumes of water molecules, and participates in regulation of tissue homeostasis and biomechanical integrity^{106,107}. HA is ubiquitously present but especially abundant in skin, accounting for approximately 50% of the total body HA¹⁰⁸. It is also present in vitreous of the eye and articular cartilage, where it provides viscoelasticity and lubrication^{106,107}. As a crucial component in the microenvironment, HA forms a pericellular matrix that is essential for proper ECM assembly and tissue architecture by acting as a platform for protein-protein interaction and cell migration¹⁰⁶.

Unlike other GAGs, unmodified HA is synthesized on the interior of the plasma membrane. Membrane-associated hyaluronan synthase (HAS) alternatively add UDP-GluUA and UDP-GlcNAc substrates to the elongating HA molecule on the inner leaflet of the plasma membrane. Elongating HA molecule protrudes through the cell membrane and remain attached via a UDP-anchor, forming a peri-cellular coat following post-translational modifications. Mammals express three predominate HAS isoforms (HAS1, 2, and 3), which are encoded on different chromosomes and exhibit distinct enzymatic properties¹⁰⁹⁻¹¹¹. Both HAS1 and HAS2 synthesize large HA polymers (1×10^6 - 1×10^7 Da), while HAS3 preferentially produce smaller sized HA (1×10^5 Da).

HA facilitates complex physiochemical functions despite its simple chemical structure. The high molecular-weight native HA polymers (>500 kDa) preferentially produced by HAS2 contributes to architectural maintenance and hydration of homeostatic adult tissues^{101,102,111}. However, it can be depolymerized enzymatically by hyaluronidases (HYAL1-3) into low molecular-weight polymers (<200 kDa) that promote proliferation, migration, and inflammation¹⁰³. Amongst all hyaluronidases, HYAL2 is often overexpressed in the peri-tumor stroma, during damage responses and tissue-remodeling processes¹⁰⁴. HYAL2 is an extracellular GPI-anchored protein that targets native HA for degradation, producing HA fragments of an intermediate size (~20kDa)^{112,113}. The resulting HA fragments are then endocytosed and delivered to the lysosome, where

HYAL1,3 further process HA into smaller oligomers (<10kDa, hexasaccharides and tetrasaccharides). HYAL1, 3 can also be present in the stroma, and are active in a low-pH microenvironment to facilitate extracellular HYAL-mediated HA degradation¹⁰³.

Under homeostatic conditions, native HA has a rapid turnover rate of under 24 hours in skin¹⁰⁸. This rapid turnover rate may be required due to the protective functions of HA, as it acts as a free radical scavenger under inflammatory conditions¹¹⁴⁻¹¹⁶. Native HA can also be depolymerized by free radicals, such as ROS produced during inflammation and exposure to environmental carcinogens (i.e: UV radiation)¹¹⁷. Excessive degradation by ROS and decrease in total skin HA may weaken the protective function of HA, such as observed after UVB radiation and in BCC¹¹⁸⁻¹²⁰. A homeostatic environment is only maintained when the rate of synthesis keeps pace with degradation. When degradation exceeds the rate of synthesis, HA fragments accumulate to a significant level, resulting in altered microenvironmental signaling¹²¹⁻¹²³. LMW-HA polymers interfere with protein-protein interactions in the pericellular microenvironment, thus jeopardizing the biomatrix integrity^{124,125}. LMW-HA can also outcompete HMW-HA binding with surface receptors to alter membrane receptor clustering and downstream intracellular signaling^{126,127}. The fragments resulting from native HA degradation are a signal for cellular stress and tissue damage. Their presence has been proposed to initiate responses designed to repair tissue damage by promoting inflammation and repair. However, cancer cells often upregulate the production of LMW-HA in an autocrine/paracrine process that promotes stromal remodeling and tumor progression^{123,128-130}.

1.4.1 *HA receptors and signaling*

Native HA and LMW-HA bind to various cell surface receptors, including CD44, Receptor for HA-Mediated Motility (RHAMM), Toll-Like Receptors (TLR), and Human Hyaluronan Receptor for Endocytosis (HARE)^{100,131}. In keratinocytes, CD44 and RHAMM are the two major receptors for surface HA¹²⁶. CD44 is an integral membrane protein that is involved in cell-matrix adhesion, cell-cell adhesion and migration. It contains an HA-binding region in the extracellular domain, while its cytoplasmic tail regulates intracellular protein signaling¹²⁶. The common standard form of CD44 contains no extra exons, however the insertion of 10 variable exons (exon 6-15) by alternative

splicing can generate different isoforms (CD44v1-10) with different physiological signaling effects and cellular consequences¹³². CD44v3-10 predominate in keratinocytes, with CD44v3 as the characteristic isoform in homeostatic skin¹³³⁻¹³⁵. HA fragments display distinct signaling properties comparing to native HA due to their selectivity in receptor-binding^{136,137}. Studies report LMW-HA/CD44 binding induces ERK1/2 phosphorylation and triggers pro-inflammatory signaling^{138,139}. In contrast, HMW-HA promotes CD44 clustering at the cell membrane¹²⁷ but does not trigger ERK1/2 activation¹³⁶⁻¹³⁸. Instead, HMW-HA facilitates anti-proliferative and anti-inflammatory responses¹⁴⁰, such as competitively inhibiting the NFκB signaling induced by LMW-HA/TLR interaction^{139,141-144}.

In contrast to CD44, RHAMM is a multi-functional HA receptor that is not highly expressed in epidermis under homeostatic conditions. Its expression is typically restricted to stratum basale, where the proliferative adult stem cells reside, and sparsely scattered throughout the adjacent layer of stratum spinosum in homeostatic epidermis¹⁴⁵. Instead, RHAMM overexpression is associated with tumorigenesis and malignant behaviors¹⁴⁶⁻¹⁵⁰, specifically in human BCC¹⁵¹. Similar to CD44, RHAMM is capable of interacting with both HMW- and LMW-HA, but its protein structure dictates HA fragments with very low molecular-weights as its preferred binding partner^{126,146}. RHAMM often co-complexes with other HA-receptors on the plasma membrane, such as CD44 and TLR, to facilitate cell migration¹²⁶. However, the cellular consequences of RHAMM/HA signaling are highly cell-specific and context-dependent. The subcellular compartmentalization of RHAMM expression pattern also adds an additional layer of complexity when dissecting RHAMM-mediated signaling^{126,152}. Current literature suggests LMW-HA/RHAMM interactions have an instructive role in breast cancer initiation and metastasis^{148,150,153-155}, while RHAMM overexpression is found in nodular BCC of patients¹⁵¹. However, the precise molecular effects of HA/RHAMM interaction in BCC remains elusive.

1.4.2 *The hyaluronome in carcinogenesis*

HA synthases, hyaluronidases, and HA receptors on the plasma membrane such as CD44 and RHAMM constitute a complex “hyaluronome”, which regulates HA functions and

metabolism. Sustained HA fragmentation is an endogenous danger signal that participates in various tissue remodeling processes such as embryogenesis, wound repair, and tumorigenesis^{116,131,156}. Specifically, LMW-HA accumulation potentiates the invasive tumor phenotype^{121,156,157} by upregulating hyaluronidase expression and activities. HYAL1 overexpression correlates with bladder and prostate cancer progression^{158-161,162}, while HYAL2 upregulation is associated with malignant cutaneous melanoma and mammary gland tumor behavior^{163,164}. Tumor cells remodel the microenvironment via upregulating HAS2, HYAL1 or HYAL2, thus promoting excessive HA synthesis and sustained degradation to potentiate invasion and metastasis¹⁶⁵⁻¹⁶⁷. Clinical and experimental studies also report elevated LMW-HA polymers promote lymph node metastasis of breast and melanoma cells^{124,156}, while correlating with poor patient prognosis¹⁵⁶. Moreover, LMW-HA is a potent promoter of inflammation, which is a key aspect of the remodeled tumor microenvironment. Fragmented HA facilitates macrophage recruitment and differentiation into the tumorigenic M2 phenotype via regulating Th1/Th2 cytokine balance, thus enhancing local ROS production and further contribute to LMW-HA production¹⁶⁸. Fragmented HA also induces the phosphorylation and activation of the pro-inflammatory NFκB^{126,142}, which is critical in establishing a tumor-permissive microenvironment for skin carcinogenesis⁷⁵.

In contrast to LMW-HA, native HA restricts cell cycle progression^{98,127}. HAS2 overexpression and hyaluronidase knockdown reduce tumor growth rate in murine astrocytoma cell lines¹⁶⁹. Similarly, administration of HMW-HA post-chemotherapy significantly inhibits tumor regrowth in colon carcinoma xenograft mice¹⁷⁰. Native HA has also been reported to reduce the migratory capacity of aggressive cancer cell lines via strengthening the cell-cell junctions, thus decreasing the ECM permeability and preventing cancerous outgrowths¹²⁵. Moreover, native HA is a well-established microenvironmental anti-oxidant and ROS scavenger¹¹⁴⁻¹¹⁶. Recent findings report reduced γ-H2AX foci formation, a biomarker for DSB sites, corresponding to HMW-HA accumulation^{114,171,172,173}, thus suggesting HA-mediated genoprotection as a possible cancer-prevention mechanism. HMW-HA/CD44 interaction is also a well-established inhibitor of inflammation through its regulation of the canonical NFκB signaling^{121,140}. Mediated by p65/p50 heterodimers, NFκB is a pro-inflammatory pathway that promotes

the expression of SHH^{174,175}, the activating ligand in sonic hedgehog signaling, which drives BCC initiation.

Taken together, the current literature suggests that the continuous depolymerization of HA enhances the oncogenic potential of the microenvironment. In contrast, HMW-HA accumulation limits tumorigenicity by restricting proliferation, invasion, and provides genoprotection. However, further conceptual advancement is required to understand the distinct size-dependent biological effects of HA in the context of tumorigenesis, and to fully harvest the therapeutic potential of HA as a microenvironmental regulator.

1.4.3 *Phosphatidylethanolamine-linked high molecular-weight hyaluronan*

Although the accumulation of native HA is associated with offering protection against oncogenic assaults and tumorigenesis in mice^{157,176}, human^{140,171}, and naked mole-rats^{93,95}, the role of HMW-HA has not yet been described in keratinocyte tumors. Conceptual advancements in the past decade have identified the primarily oncogenic driver and the cancer-initiating cells in the epidermal microenvironment, and established well-characterized mouse models to study BCC. Thus, this keratinocyte cancer is an ideal disease model to interrogate the effects of microenvironmental agents on regulating the tumorigenic potential of cancer-initiating cells. Exogenous applications of HMW-HA have been reported to reduce inflammation *in vitro*¹⁷⁷ and restore skin homeostasis in aged mice by promoting epidermal barrier function¹⁷⁸, all are critical to suppressing tumorigenesis. Although promising, current delivery methods failed to reliably and efficiently distribute and retain HA with molecular weights greater than 50kDa in the epidermis and dermis^{179–181}. This failure is likely due to the large molecular weight and high hydrophilicity of native HA, resulting in poor absorption across the hydrophobic stratum corneum¹⁸². Rapid degradation of exogenous HA formulation by cells and the dependency of receptor expression for pericellular coat formation further contribute to the failure of sustained HMW-HA delivery into the epidermis¹⁸².

To address these issues, native hyaluronan polymers were linked to phosphatidylethanolamine (HA-PE) and incorporated into a topical formulation (patent number: US20130059769A1; E. Turley, WorlDiscoveries)¹⁸³. To further investigate the

role of HA in offering BCC protection, HA-PE was applied onto the dorsal skin of UVB-exposed *Ptch*^{+/*LacZ*}/*Hr*^{-/-} mice, which are susceptible to UVB-induced keratinocyte tumors^{184,185}. HA-PE allowed the formation of sustained HA-coats on epidermal keratinocytes and dermal fibroblasts upon topical application¹⁸³. Previously, we demonstrated that the formation of HA-coat was independent of major HA receptors on the plasma membrane, CD44, but instead was augmented by its linkage with phosphatidylethanolamine¹⁸³. The HA-coat sustained on cell membrane 72 hours post-administration, which exceeds the normal native hyaluronan half-life in the epidermis¹⁸³. This accumulation of epidermal HA was associated with no histologically-detectable keratinocyte tumor formation in BCC-susceptible mice, while control groups spontaneously developed keratinocyte tumors after UVB treatment.

1.5 Animal models in BCC research

An appropriate animal model should permit the analysis of the molecular pathogenesis underlying tumor initiation and allow for the assessment of preventative therapies. Key players in the sonic hedgehog pathway are ideal to study BCC in murine models since it is the primary oncogenic driver pathway in skin carcinogenesis. Mouse models carrying a heterozygous *Ptch1* knockout, overexpression of SHH, mutant active SMO, and GLI2 have been well-characterized as appropriate models to study sporadic development of BCC⁵⁸⁻⁶². Since inactivating mutations of PTCH1 is the most common genetic alteration in human BCCs and homozygous loss of *Ptch1* is embryonically lethal, *Ptch*^{+/-} mutants are the most appropriate model to study human BCC. A common *Ptch*^{+/-} model is established by the replacing exon 1 and 2 of the *Ptch1* allele with a *LacZ* gene, thus introducing an inactivating mutation¹⁸⁶. The *Ptch1*^{+/*LacZ*} genotype increases susceptibility of sporadic BCC development upon chronic UV exposure (up to 32 weeks) in mice, and allows the protein product, β-galactosidase (β-gal), to be used as a reporter for *Ptch1* expression¹⁸⁶.

Mice carrying homozygous mutational inactivation of *Hairless* (*Hr*^{-/-}), a transcriptional co-repressor essential for hair cycling and growth¹⁸⁷⁻¹⁸⁹, is another model commonly used in dermatologic research concerning keratinocyte tumorigenesis^{186,190}. More commonly used to study SCC initiation and progression, *Hr*^{-/-} mice exhibits disrupted hair follicles and the

hairless phenotype (alopecia) after one round of normal hair cycling in newborn litters^{189,191}. Biallelic *Hr* loss accelerates the keratinocyte tumor initiation process comparing to haired littermates, without altering the expression of sonic hedgehog and BCC-related oncogenic driver pathway components in mice¹⁸⁶. Although the morphology of hair follicles is disrupted, the cell compositions and functions in the hair follicles are not altered¹⁹¹. Hairless phenotype also allowed us to directly apply topical HA-PE cream to directly assess the protective effects of HMW-HA. At the molecular and histological levels, UV-induced skin neoplasms in *Hr*^{-/-} models closely resemble tumors in human patients^{186,190}, therefore representing an appropriate model to examine keratinocyte tumors in mice.

1.6 Hypothesis and objectives

Since both carcinogens and initiating driver pathway mutations of BCC are well-established in human and mice, we decided to interrogate the cancer resistant ability of HMW-HA in the context of BCC initiation. Previously, histopathological analyses reported the complete lack of keratinocyte neoplasm occurrence after HA-PE treatment in chronically UVB-exposed *Ptch*^{+/*LacZ*}/*Hr*^{-/-} mice. Here, I aim to identify the mechanisms of HA-mediated resistance against keratinocyte tumorigenesis. HA-PE treatment is hypothesized to offer resistance against BCC initiation through inhibiting the oncogenic driver, sonic hedgehog signaling pathway, in the epidermis and hair follicles of susceptible mice. Therefore, the following objectives were proposed to test this hypothesis.

Objective 1: Verify HA-PE mediated inhibition of BCC tumor initiation by assessing sonic hedgehog signaling in *Ptch*^{+/*LacZ*}/*Hr*^{-/-} mice.

We chose to investigate the sonic hedgehog pathway to assess tumor initiation, since its aberrant signaling is essential for BCC pathogenesis in human and mouse models^{29,32}. The overexpression of PTCH1 and GLI1 are well-established molecular markers for signaling activities since they are both target genes and regulator of this oncogenic pathway. Moreover, the insertion of a promoterless *E. coli LacZ* gene into *Ptch1* allows the usage of bacterial β -gal to measure *Ptch1* promoter activity. *LacZ* insertion also introduces a heterozygous loss-of-function mutation in *Ptch1*, thus mimicking the genotype of sporadic

BCC patients^{40,43,66}. Therefore, we used β -gal and GLI1 expression as a measurement of sonic hedgehog signaling and BCC initiation in *Ptch*^{+/*LacZ*/*Hr*^{-/-} mice.}

Objective 2: Determine the cellular consequences of HA-PE application in *Ptch*^{+/*LacZ*/*Hr*^{-/-} mice.}

To investigate the mechanisms that are responsible for the suppressive effects against UVB-induced BCC tumorigenesis, the cellular effects of HA-PE application on epidermal keratinocytes and hair follicle cells were examined. HMW-HA was reported to act as a genoprotective agent by acting as a free-radical scavenger¹¹⁴⁻¹¹⁶, thus the DNA damage in epidermis and hair follicles of UVB-exposed mice was assessed. Target genes of sonic hedgehog signaling (cyclin D1, BCL2) and associated cellular consequences (cell cycle progression and apoptosis) were also investigated in transgenic mice.

Aim 1: Assess if HA-PE application protected keratinocytes from UVB- and ROS-induced DNA damage.

Aim 2: Examine the effects of HA-PE on cell cycle progression and apoptosis in the epidermis of UVB-exposed mice.

Chapter 2

2 Materials and methods

2.1 Animal studies

Experiments were approved by and compliant with the standard operating procedures of the Animal Use Subcommittee at the University of Western Ontario (2009-060). All animal experiments were conducted by Katelyn Cousteils, with detailed breeding schemas and conditions reported previously¹⁹². Briefly, female *Hr*^{-/-}/SKH-1 mice (Strain 477, Charles River Laboratories, Wilmington, MA, USA) were crossed with *Ptch*^{+LacZ}/C57BL/6 male, haired mice (Stock number 003091, Jackson Laboratory, Bar Harbor, ME, USA). F1 litters between 14 to 21 days of age were genotyped for *Ptch*^{+/-} heterozygosity. F1 *Ptch*^{+/-}/*Hr*^{+/-} male mice were crossed with F1 *Ptch*^{+/-}/*Hr*^{+/-} female mice, and F2 *Ptch*^{+/-}/*Hr*^{-/-} mice were utilized for the study.

Ptch^{+/-}/*Hr*^{-/-} mice were separated into four experimental groups: no UVB control (No UVB, n= 5), UVB-only control (UVB, n=7), UVB with vehicle cream control (UVB + vehicle, n=10), and UVB with HA-PE cream (UVB+HA-PE, n=10). An UV-irradiation unit (Daavlin Co., Bryan, OH, USA) equipped with an electronic UV-dosage controller¹⁸⁶ was used to administer UV radiation. Litters between 6 to 7 weeks of age were selected and exposed to UV irradiation, which was composed of UVA of 315-400 nm, accounting for 20% of total energy; and UVB of 290-315 nm, accounting for 80% of total energy. Subjects were irradiated for 4 weeks and 26 weeks to study the acute and chronic effects of HA-PE on UVB-induced BCC, respectively. Litters received 180 mJ/cm² of UVB irradiation twice per week (Thursdays and Fridays) for 30 to 45 seconds, while vehicle or HA-PE cream was applied prior to UVB-irradiation, once daily for five days each week (Monday to Friday).

Lesions and skin abnormalities were measured using digital calipers (500-170-30, Aurora, IL, USA), excised using 8-mm punch biopsy from the dorsal back, and processed to be paraffin-embedded for histological analyses. Lesion-adjacent phenotypically-normal skin

was also excised using an 8-mm punch biopsy, frozen using 70% ethanol and dry ice and stored at -80°C.

Histopathology analysis of skin abnormalities was conducted at the Centre for Phenogenomics (Toronto, ON, CA) using paraffin-embedded slides stained with H&E. Neoplasia was identified by histological features characteristic of BCC (large nuclei, scant cytoplasm, mitotic features), cell morphology, and clonal expansion.

2.2 Immunohistochemistry

Immunohistochemistry of paraffin-embedded tissue was conducted as previously described¹⁹³. Briefly, sections were de-paraffinized through two passages of xylene for 15 minutes each wash and rehydrated through a descending ethanol series (100%, 95%, 70%) for 10 minutes each change. Slides were washed in buffer (Table 1) and one change of dH₂O for 5 minutes each. Antigen retrieval was performed using 10mM sodium citrate buffer (pH 6.0) in a standard microwave. Specimen were washed in the two changes of the appropriate buffer for 5 minutes each, and endogenous peroxidase activity was inhibited by incubating slides in 3% H₂O₂ for 20 minutes. Non-specific antibody binding was blocked by incubating slides in 3% bovine serum albumin (BSA) at room temperature for 1 hour. Diluted primary antibody was added to each slide and incubated at 4°C overnight in humidifying chambers, with non-immune anti-mouse immunoglobulin (IgG) incubated on the negative control (Table 1). Following two washes in the appropriate buffer solution, the slides were incubated with 1:100 biotinylated goat anti-rabbit secondary antibody (catalog number: E0432, Agilent Technologies, CA, USA) diluted in phosphate buffer saline (PBS: 137 mM NaCl, 12 mM phosphate, 2.7 mM KCl, pH 7.4) or Tris-buffer saline (TBS: 50 mM Tris-Cl, pH 7.5, 150 mM NaCl) at room temperature (approximately 25°C) for 2 hours in humidifying chambers. Streptavidin-conjugated horseradish-peroxidase (catalog number: ab7403, AbCam, MA, USA) was diluted in 1xPBS or TBS to 1:1000-fold and added onto each slide for 30 minutes at room temperature, followed by incubation with diaminobenzidine substrate (DAB, catalog number: K3467, Agilent Technologies, CA, USA). Counterstaining was carried out using hematoxylin diluted 1:10-fold in ddH₂O (10143-606, VWR, PA, USA). Sections were dehydrated by passaging through the ethanol

series (70%, 95%, 100%) and two changes of xylene. All slides were mounted using Cytoseal-60 (catalog number: 8310-16, ThermoFisher Scientific, MA, USA), and dried at room temperature.

2.2.1 *Image analysis*

All sections were scanned using Aperio ScanScope (Leica Biosystems, Wetzlar, Germany) and analyzed using ImageJ or QuPath. All quantifications were conducted on the epidermis of animal sections, and keratinocytes within the field of view were quantified according to their epidermal compartmentalization (suprabasal layer, stratum basale, and hair follicles). For intensity quantification, the DAB channel in each image was separated from the hematoxylin channel using the “Colour deconvolution” algorithm, and measured using the “Pixel measurement” algorithms in ImageJ. DAB-stained brown pixels in slides from all experimental groups were compared to the negative control, which was used as the threshold. Semi-automatic positive cell counts of all slides were conducted using the “Positive cell detection” algorithm from QuPath (v0.1.9) as previously described¹⁹⁴, and all algorithm-generated data were verified by manual counting.

2.2.2 *Vertical lineage tracing*

Vertical lineage tracing was conducted on γ -H2AX stained paraffin-embedded tissues. Daughter cells proliferating from progenitor cells in the stratum basale layer were identified, and the number of γ -H2AX positive daughter cells originating from the same progenitor cell was quantified through manual cell counting using ImageJ. All suprabasal keratinocytes and basal progenitor cells in images were quantified.

2.3 Immunofluorescence and image analysis

Immunofluorescence of paraffin-embedded tissue sections was conducted identically to the protocol for immunohistochemistry (section 2.2 and 2.2.1) described above, with the quenching of endogenous peroxidase omitted. After secondary antibody incubation using either Alexa 488-conjugated mouse anti-rabbit IgG (catalog number: A32731, Invitrogen, MA, USA) at 1:200-fold dilution or Alexa 555-conjugated mouse anti-mouse IgG (catalog

number: A32727, Invitrogen, MA, USA) at a 1:200-fold dilution, slides were washed in the appropriate buffer solution (Table 1). Sections were then mounted using DAPI-containing ProLong Gold anti-fade mounting reagent (catalog number: P36931, ThermoFisher Scientific, MA, USA).

All tissue sections were imaged using IX81 Olympus confocal microscope equipped with FV10-ASW 4.2 software at 20x or 40x magnifications. Images were saved in tiff format and quantified using ImageJ or QuPath as described above. Keratinocytes within the field of view were quantified according to their epidermal compartmentalization (suprabasal layer, stratum basale, and hair follicles). To quantify the intensity of antibody immunoreactivity, DAPI, FITC and TexasRed channels were first separated in ImageJ using the “Split channel” algorithm, and threshold against the negative control. Epidermal compartments in each field of view were selected manually, and the “Pixel measurement” algorithm was used to detect intensity. Similarly, individual colour channels were separated in QuPath and the “Positive cell detection” algorithm was used to detect keratinocytes positive for antibody staining as previously described¹⁹⁴, and all algorithm-generated counts were verified manually.

Table 1: Antibodies and buffers used in immunohistochemistry and immunofluorescence of paraffin-embedded tissue sections.

Primary antibody	Catalog number	Dilution	Wash buffer	Antigen retrieval buffer
β -galactosidase	A11132, Life Technologies Corporation, CA, USA	1:200	1xPBS	10 mM Sodium citrate, pH 6.0
GLI1	ab151796, Abcam, MA, USA	1:900	1xTBS	
CD44	553130, BD Biosciences, ON, CA	1:200	1xPBS	
RHAMM	ab124729, Abcam, MA, USA	1:50	1xPBS	
Phospho-histone H2AX (Ser139)	9718, Cell Signalling Technology, MA, USA	1:150	1xTBS	
Bcl-2	sc-492, Santa Cruz Biotechnology	1:300	1xPBS	
Cyclin D1	ab16663, Abcam, MA, USA	1:100	1xTBS	
Ki67	ab16667, Abcam, MA, USA	1:100	1xPBS	
NF κ B-p50	sc-114, Santa Cruz, Biotechnology	1:100	1xTBS	
NF κ B-p65	Sc-8008, Santa Cruz Biotechnology	1:100	1xTBS	
SMA	ab124964, Abcam, MA, USA	1:100	1xPBS	
Cleaved caspase 3 (Asp175)	9664, Cell Signalling Technology, MA, USA	1:50	1xTBS	10 mM Sodium citrate, 0.05%
Cytokeratin-15	ab80522, Abcam, MA, USA	1:100	1xTBS	Tween-20, pH 6.0

2.4 Detection of HA in tissue sections and analysis

HA detection in paraffin-embedded tissue sections was conducted similarly to the protocol for immunohistochemistry described above, with modifications stated below. Following de-paraffinization of slides, the antigen retrieval step was omitted. The primary antibody was replaced by an HA-binding biotinylated protein (catalog number: K-1203, Echelon Biosciences, UT, USA), and incubated at 37°C for 1 hour. Negative control was established by replacing the HA-binding biotinylated protein with 3% bovine serum albumin diluted in PBS. Slides were incubated in 3% H₂O₂ for 15 minutes at room temperature and incubated with HRP/streptavidin diluted to 1:1000-fold in 1xPBS. DAB reagents were added onto each slide for 20 minutes at room temperature, and counterstained with Harris' Hematoxylin (catalog number: 10143-606, VWR, PA, USA) at 1:10-fold diluted with dH₂O. All slides were washed in 1xPBS for 10 minutes between each step. Sections were dehydrated by passage through the ethanol series and xylene in reverse, and mounted in Cytoseal-60. Quantification of HA staining was carried identically to the protocols for immunohistochemistry quantification described above.

2.5 RT-qPCR

2.5.1 *Total RNA extraction from tissue*

RNA extraction from tissue was performed via standard trizol/chloroform extraction protocol. All equipment was cleaned with 70% ethanol and RNase-away solution (catalog number: 10328-011, Invitrogen, MA, USA). Briefly, approximately 1 gram of frozen skin biopsy and 500 µL of trizol (catalog number: 15596018, Life Technologies Corporation, CA, USA) were added into a micro-centrifuge tube, and homogenized using a hand-held Dounce homogenizer. Fresh 500µL of trizol were added to samples once they are adequately homogenized, followed by mixing by inversion and incubated at -20°C for 5 minutes. 200 µL of chloroform (catalog number: 423555000, Acros Organics, NJ, USA) was added to samples, vortexed for 10 seconds and incubated at room temperature for 3 minutes. Samples were centrifuged at 4°C for 15 minutes at 12,000 rpm, with the top

aqueous layer transferred into new tubes. Ice-cold isopropanol (500 μL) was added to samples and stored at -20°C overnight. Samples were centrifuged at 4°C for 30 minutes at 12,000 rpm, and supernatants were discarded with the pellets washed in ice-cold 70% ethanol. Samples were centrifuged at 4°C for 10 minutes at 7,500 rpm, and the supernatants were aspirated. Pellets were air-dried and resuspended in 20 μL of nuclease-free ddH₂O, with the RNA concentration measured via NanoDrop One/OneC (ThermoFisher Scientific, MA, USA). Samples with an A260/280 > 1.9 and A260/230 > 1.7 were used for further experiments, and stored at -80°C until further assays.

2.5.2 *In vitro reverse transcription*

Complementary DNA (cDNA) was synthesized using SuperScript IV VILO Master Mix kit (catalog number: 11756050, Invitrogen, MA, USA). 4 μL of SuperScript IV VILO master mix solution was incubated with 1 μg of RNA template and nuclease-free water for a final reaction volume of 20 μL . Samples were gently mixed and incubated at 25°C for 10 minutes to allow primer annealing, followed by incubation at 50°C for 1 hour to allow elongation. Samples were then heated to 85°C for 5 minutes to inactivate reverse transcriptase, briefly centrifuged and stored at -20°C until further assays were performed.

2.5.3 *PCR reactions and analysis*

RT-PCR was performed to analyze *CD44* expression in transgenic mice. Each PCR reaction consisted of 20 ng of cDNA template, 0.5 μL of 10 μM forward and reverse primers (Table 2), 0.5 μL of GC enhancer, 10 μL of AmpliTaq 360 master mix, and nuclease-free ddH₂O to reach a total volume of 25 μL . PCR reactions were carried out at 95°C for 10 minutes, 94°C for 30 seconds, 55°C for 30 seconds, 72°C for 30 seconds for 40 cycles, and a final elongation step at 72°C for 7 minutes using DNA Engine Tetrad 2 Thermocycler (Bio Rad, CA, USA). All target gene expression was compared with the house control gene GAPDH on a 1% agarose gel containing ethidium bromide, and imaged using ChemiDocTM XRS+ System (Bio Rad, CA, USA).

2.5.4 Real-time PCR reactions and analysis

RT-qPCR was performed to analyze the mRNA expression of *Hyal2*, *Hyal3*, *Hmnr*, *Shh*, *Ccncb1*, *Cdk4*, and *Gapdh* in transgenic mice. Each PCR reaction consisted of 20 ng of cDNA template, 0.5uL of 10uM forward and reverse primers (Table 2), 10 μ L of SYBR Green PCR Master Mix (catalog number: 4309155, Thermofisher Scientific, MA, USA), and nuclease-free ddH₂O to reach a total volume of 20 μ L. PCR reactions were carried out on a 96-well plate at 95°C for 3 minutes, 60°C for 10 seconds, and 72°C for 30 seconds for 40 cycles using Stratagene Mx3000P system (Agilent Technologies, Santa Clara, CA). Ct values were exported from the thermocycler and analyzed using excel according to the $2^{-\Delta CT}$ method.

Table 2: Primers used in RT-qPCR and RT-PCR.

Gene	Forward primer	Reverse primer
<i>Hyal2</i>	GCAGGACTAGGTCCCATCATC	TTCCATGCTACCACAAAGGGT
<i>Hyal2</i>	TCTGTGGTATGGAATGTACCCT	TGCACACCAAAATGGGCCTTA
<i>CD44s</i>	GCCTACTGGAGATCAGGATG	GATCCATGAGTCACAGTGCG
<i>CD44v3</i>	GCCTACTGGAGATCAGGATG	TCATTTTCCTCATTTGGCTCCC
<i>CD44v4</i>	GCCTACTGGAGATCAGGATG	TCTGGGTTTGAATGGTTTGGC
<i>CD44v8</i>	ACAACCCTTCAGCCTACTGC	GATCCATGAGTCACAGTGCG
<i>CD44 v10</i>	CCCAGTGACCCCTGCTAAAA	GATCCATGAGTCACAGTGCG
<i>Hmmr</i>	CCTTGCTTGCTTCGGCTAAAA	AGCAAAGCTCAATGCAGCAG
<i>Shh</i>	GGCAGATATGAAGGGAAGAT	ACTGCTCGACCCTCATAGTG
<i>Ccnb1</i>	AGCAAATATGAGGAGATGTACC	CGACTTTAGATGCTCTACGGA
<i>Cdk4</i>	AACTGATCGGGACATCAAGG	CAGGCCGCTTAGAAACTGAC
<i>Gapdh</i>	TGAGGCCGGTGCT GAGTATGTCG	CCACAGTCTTCTG GGTGGCAGTG

2.6 Enzyme-linked immunosorbent assays

2.6.1 DNA extraction from tissue

Approximately 1 gram of frozen tissue sample was incubated in lysis buffer (1M Tris, 0.5M EDTA, 10% SDS, 5M NaCl, pH 8.0) and 20 mg/mL proteinase K (Roche, Mannheim, Germany) overnight at 55°C with constant agitation. Samples were centrifuged at 200xg for 10 minutes at room temperature, and the supernatants in each sample were transferred into new tubes. 100 µL of Protein precipitation solution (catalog number: A975A, Promega Corporation, WI, USA) was added to samples and centrifuged at 14,000xg for 10 minutes. Supernatants were briefly chilled on ice followed by centrifugation at 14,000xg for 5 minutes, with pellets discarded. Immediately after, ice-cold isopropanol (500 µL) was added to supernatants, mixed by inversion five times and incubated at -20°C for 30 minutes. All samples were centrifuged at 14,000xg for 15 minutes, and pellets were washed with ice-cold 70% ethanol. After, samples were centrifuged at 14,000xg for 10 minutes again and washed pellets using ice-cold 70%. Resulting pellets were air-dried at room temperature and suspended in 20 µL of ddH₂O. Sample concentration were measured using NanoDrop One/One^C (ThermoFisher Scientific, MA, USA), and stored in -20°C until further use. Only samples with an A_{260/280} ratio between 1.8 to 1.9 were used in future experiments.

2.6.2 8-oxo-2'-deoxyguanosine ELISA

Nuclear ROS-adducts 8-oxo-2'-deoxyguanosine (8-oxo-dG) were detected using a commercially available ELISA kit (catalog number: 4380-096-K, Trevigen, MD, USA). DNA was extracted from frozen tissue as described in section 2.5.1. Samples were diluted in nuclease-free ddH₂O to 200 µg/mL, and 100X cations (catalog number: 4380-096-05) was added for a final 1X concentration. 0.8 µL of DNase I (catalog number: 4380-096-06, 5 U/uL) and alkaline phosphatase (catalog number: 4386-096-07) were added to each sample and incubated at 37°C for 1 hour separately. Digested samples were aliquoted and stored at -20°C until assayed. 8-oxo-dG standards (catalog number: 4380-096-01, 20 µM)

were serially diluted with assay diluent (catalog number: 4380-096-02) to construct a standard curve (200 nM, 100 nM, 50 nM, 25 nM, 12.5 nM, 6.25 nM, and 3.13 nM). 25 μ L of standards, blank and DNA samples were pipetted in triplicates into a 96-well plate pre-coated with 8-oxo-dG, with 25 μ L of anti-8-OHdG monoclonal antibody (catalog number: 4380-096-03, diluted 1:250-fold in assay diluent) added to each well. The plate was covered with a film sealer and incubated for 1 hour at 25°C. All wells were washed with 4 changes of 1xPBST (137 mM NaCl, 12 mM phosphate, 2.7 mM KCl, pH 7.4, 0.1% Tween-20) for 30 seconds, with excess liquid aspirated. Goat-anti-mouse IgG-HRP conjugate (catalog number: 4380-096-04, diluted 1:500-fold in assay diluent) was added to all wells, and incubated at 25°C for 1 hour. The plate was then washed with 4 changes of 1xPBST with excessive liquid aspirated. 50 μ L of room-temperature TACS-Sapphire colorimetric substrate (catalog number: 4822-096-08) was added to all wells, and incubated for 15 minutes at 25°C in the dark. The reactions were stopped by adding 50 μ L of 5% phosphoric acid to all wells, and absorbance was read immediately at 450 nm.

The average absorbance for all standards, samples and blanks were calculated, with the blank average subtracted from standard and sample averages to determine relative absorbance. The log of 8-oxo-dG standard concentration (ng/mL) was plotted against the relative absorbance to derive a standard curve, and 8-oxo-dG concentration in samples was calculated and interpolated from the standard curve.

2.6.3 *Cyclobutane pyrimidine dimer ELISA*

Protocol was carried as described by the manufacturer (catalog number: STA-322, Cell Biolabs). Briefly, genomic DNA (gDNA) was extracted from tissue samples as described in section 2.7.1, and incubated at 95°C for 10 minutes to denature double-stranded DNA (dsDNA) into single-stranded DNA (ssDNA). Samples were briefly chilled on ice, and diluted to 4 μ g/mL in ice-cold 1xTE buffer (10 mM Tris, pH 8.0, 1mM EDTA). Similarly, CPD-DNA standards and reduced DNA provided in the commercial kit were denatured into ssDNA via incubation at 95°C for 10 minutes. Standards were serially diluted to create a standard curve (0, 1.56, 3.13, 6.25, 12.5, 25, 50, 100 ng/mL) in ice-cold TE buffer. Samples and CPD-DNA standards were added to a 96-well plate, with an equal volume of

DNA binding solution added to each well and mixed thoroughly via pipetting. The plate was incubated at room temperature overnight with constant agitation. Solutions were aspirated and wells were washed twice with 1xPBS, with excess fluid removed by blotting. Assay diluent was added to each well to block non-specific binding at room temperature for 1 hour. After assay diluent was removed from well, anti-CPD antibody (catalog number: 232202, Cell Biolabs) were diluted 1:1000 in 1xTE buffer and added to each well and incubated at room temperature for 1 hour with constant agitation. All wells were washed five times with wash buffer and blotted to remove excess fluid, followed by incubation with secondary antibody-HRP conjugate (diluted 1:1000 in 1xTE buffer, catalog number:10902, Cell Biolabs) at room temperature for 1 hour on an orbital shaker. Plate was washed five times in wash buffer and excess fluid was removed. Substrate solution warmed to room temperature was incubated in each well for 20 minutes, stop solution was added to each well to stop the enzyme reaction. Absorbance of all wells was read using a microplate reader at 450 nm immediately after stop solution addition. Reduced DNA standard was used as an absorbance blank, and all DNA samples were assayed in triplicates. The average absorbance for all standards, samples and blanks was calculated, with the blank average subtracted from standard and sample averages to determine relative absorbance. The CPD-DNA standard concentration (ng/mL) was plotted against the relative absorbance at OD_{450nm} to derive a standard curve. The CPD concentration in extracted DNA was calculated and interpolated using the standard curve.

2.7 Terminal deoxynucleotidyl transferase dUTP nick end labeling (TUNEL) assay

Detection of apoptosis was carried out using ApopTag Fluorescein *In Situ* Apoptosis Detection Kit (S7110, EMD Millipore, MA, USA) following the protocol provided by the manufacturer. Briefly, slides were deparaffinized by passage through two changes of xylene (10 minutes each wash) and a descending series of ethanol (100%, 95%, and 70% for 5 minutes each wash), followed by one change of 1xPBS for 5 minutes. Slides were incubated in freshly diluted proteinase K (20 µg/mL) for 15 minutes at room temperature, and washed in 2 changes of 1xPBS for 2 minutes each wash. Equilibration buffer was

added to each specimen and incubated at room temperature for 30 minutes. Immediately afterward, 55uL of terminal deoxynucleotidyl transferase (catalog number: 90418, EMD Millipore, MA, USA) and reaction buffer (catalog number: 90417, EMD Millipore, MA, USA) mixture in 1:3 ratio was added to slides, and stored in humidified chambers at 37°C for 1 hour. Negative and positive controls were established by omitting the reaction buffer in the mixture and treatment with DNase I (catalog number: 4380-096-06, 5U/uL, Trevigan, MD, USA) at 37°C for 1 hour, respectively. Reaction was stopped by incubating in Stop Buffer (catalog number: 90419, EMD Millipore, MA, USA) at room temperature for 10 minutes, followed by 3 washes in 1xPBS for 1 minute each wash. Room-temperature mixture containing anti-digoxigenin conjugate (catalog number: 90426, EMD Millipore, MA, USA) and blocking solution (catalog number: 90425, EMD Millipore, MA, USA) was added to each specimen, and incubated at room temperature for 30 minutes in the dark. All slides were washed in 4 changes of 1xPBS for 2 minutes each wash, and counterstained with DAPI-containing ProLong Gold anti-fade mounting reagent. All specimens were stored at -20°C in the dark.

Images were captured on IX81 Olympus confocal microscope using the negative control as the minimal threshold for laser settings. All images were analyzed using ImageJ to manually count TUNEL-positive cells in each image (approximately 1000 cells per field), with the interfollicular epidermis and hair follicles quantified separately.

2.8 Hyaluronidase activity ELISA-like assay

Detection of hyaluronidase activity in whole skin samples was conducted as described previously^{195,196}. Briefly, 3 grams of tissue was suspended in ice-cold homogenization buffer (5 mM HEPES, pH 7.2; 1 mM benzamidine-HCl) and homogenized using a Dounce homogenizer (Ika Works Inc, Wilmington, NC). Lysate was centrifuged at 10,000xg for 30 minutes, with total protein concentration measured through BCA assay and compared to a BSA standard curve.

A 96-well plate was coated with high molecular-weight human umbilical hyaluronan (200 µg/mL, H1876, Sigma-Aldrich, MO, USA) diluted in 0.1M sodium bicarbonate solution

(pH 9.2) overnight at 4°C. HA-coated wells were washed three times in 1xPBST. Tissue samples were diluted in reaction buffer (0.1 M sodium acetate, 0.15 M NaCl, 0.2 mg/mL BSA, pH 5.3) and 10 µg of total protein was loaded in each well. Purified bovine hyaluronidase (catalog number: H3506-1G, Sigma-Aldrich, MO, USA) and an HA-coated well with only reaction buffer were used as the positive and negative control, respectively. The 96-well plate was incubated at 37°C for 6 hours to allow HA digestion. All wells were washed thrice in 1xPBST.

Using hyaluronan enzyme-linked immunosorbent assay kit (catalog number: K-1200, Echelon Biosciences Inc., UT, USA), the remainder of HA in each well detected as a measurement of hyaluronidase activity. HA detection was carried out according to the protocol provided by the manufacturer with modifications stated as below. 100 µL of biotinylated HA-binding protein (catalog number: K-1203, Echelon Biosciences Inc., UT, USA) was added to all wells and incubated at 37°C for 1 hour. Wells were aspirated and washed with 1xPBST three times, with excessive fluid blotted. Enzyme (catalog number: K-1206, Echelon Biosciences Inc., UT, USA) was diluted by adding 6 mL of diluent provided by the kit (catalog number: K-1204, Echelon Biosciences Inc., UT, USA), and added to each well and incubated at 37°C for 30 minutes. Wells were aspirated by blotting. Substrate buffer (catalog number: K-1208, Echelon Biosciences Inc., UT, USA) and one pellet of the substrate, p-nitrophenyl phosphate tablet, were mixed together and added to each sample and incubated at room temperature for 40 minutes in the dark. Plate was immediately read using a plate reader (Synergy H4 Hybrid Reader, BioTek, VT, USA) at 405 nm, with OD_{405nm} inversely proportional to the HA remaining in each well after hyaluronidase digestion.

2.9 HA size determination by agarose gel

2.9.1 *HA isolation from tissue*

HA extraction from tissue was conducted as described previously^{195,196}. Briefly, 3 grams of whole skin sample was incubated overnight at 50°C with constant agitation in digestion buffer (10 mM Tris-Cl, 25 mM EDTA, 100 mM NaCl, 0.5% SDS) and 20mg/mL

proteinase K. EDTA was chelated by adding 27 mM of MgCl₂, and proteinase K was inactivated at 95°C for 10 minutes. Nucleic acids were removed by benzonase nuclease (500 U/μL, catalog number: E1014, Sigma-Aldrich, MO, USA) digestion at 37°C overnight. The absence of nucleic acid was confirmed by running samples on 1% agarose gel stained with ethidium bromide at 100V for 40 minutes. Samples were purified through standard phenol/chloroform protocol followed by ethanol precipitation. Briefly, samples were mixed with 1:1 v/v phenol/chloroform, and centrifuged at 8,000xg for 15 minutes. The aqueous phase was transferred to a new tube, with an equal volume of chloroform added and centrifuged at 10,000xg for 15 minutes. This step was repeated twice, followed by the addition of 2.5 volumes of ice-cold 100% ethanol to the aqueous phase. Samples were stored at -20°C overnight to maximize precipitation. All samples were centrifuged for 10 minutes at 14,000xg and supernatants were discarded. Pellets were washed with 4 volumes of ice-cold 70% ethanol, and centrifuged for 10 minutes at 14,000xg. Pellets were air-dried at room temperature, and resuspended in 20 μL of 10 mM Tris-Cl (pH 8.5). Samples were stored at -20°C until gel electrophoresis.

2.9.2 *Gel electrophoresis and visualization*

The protocol of determining HA polymer size through gel electrophoresis was adapted from previous literature¹⁹⁵⁻¹⁹⁷. Briefly, agarose was diluted in 1xTAE buffer (40mM Tris, 20mM glacial acetate acid, 2mM EDTA, pH 8.5) and dissolved in a microwave, followed by incubation at 45°C for 15 minutes. Electrophoresis chambers were filled with 1xTAE and ran at 100V for 20 minutes to clear impurities from the agarose gel. Samples were separated into two reactions, with one reaction incubated with purified bovine hyaluronidase (catalog number: H2506, Sigma-Aldrich, MO, USA) at 37°C for 1 hour as a negative control. Loading dye (0.02% bromophenol blue, 85% glycerol) was added to both reactions. The HA polymer size in reactions was visualized on a 2.5% agarose gel, and gel electrophoresis was carried out at 90V for 1 hour, followed by 100V for 2.5 hours. Agarose gel was placed in staining solution (0.005% Stains-all, 50% ethanol) in the dark overnight at room temperature, then briefly de-stained in dH₂O for 20 minutes in the dark with constant agitation. Afterward, a freshly-diluted concentrated staining solution (0.01%

Stains-all, 50% ethanol) was incubated with the agarose gel for 40 minutes. The final de-staining step was carried out in dH₂O for 2 hours in the dark with constant agitation.

2.10 Statistical analyses

Experimental data are presented as mean \pm standard error mean (SEM), with significances detected at p-value < 0.05 . All immunofluorescence and immunohistochemistry experiments were performed with a sample size of n=3 animals per treatment group, 5 replicates per animal. All ELISA and RT-PCR experiments were conducted in triplicates. Significances were calculated using two-sample t-test or one-way ANOVA, followed by Tukey's test as post-hoc analyses in GraphPad Prism 7 (GraphPad Software, Ca, USA, www.graphpad.com) for quantitative analyses for immunohistochemistry.

Chapter 3

3 Results

3.1 HA-PE application promotes epidermal HA accumulation

To explore the potential role of HA in preventing skin tumorigenesis, HA-PE was topically applied onto the dorsal skin of UVB-exposed *Ptch*^{+/*Lacz*/*Hr*^{-/-} mice. HA-PE application significantly increased total HA in the epidermis, hair follicles and the dermis (Figure 3). This accumulation corresponded to significantly reduced hyaluronidase-2 (*Hyal2*) mRNA expression, an isoform that preferentially targets surface high molecular-weight HA for degradation. In contrast, the mRNA expression level of hyaluronidase-3 (*Hyal3*), a lysosomal isoform that promotes LMW-HA cleavage into oligosaccharides, remained unchanged (Figure 4.A). A significant decrease in total hyaluronidase activity in skin was also observed after HA-PE application, corresponding to the increased accumulation of epidermal HA (Figure 4.B). Since decreased hyaluronidase activity and enhanced HA accumulation are associated with reduced tumorigenicity in murine models^{157,198}, I next examined sonic hedgehog signaling, which is the primary oncogenic driver underlying BCC, in the interfollicular epidermis and hair follicles of UVB irradiated *Ptch*^{+/*Lacz*/*Hr*^{-/-} mice.}}

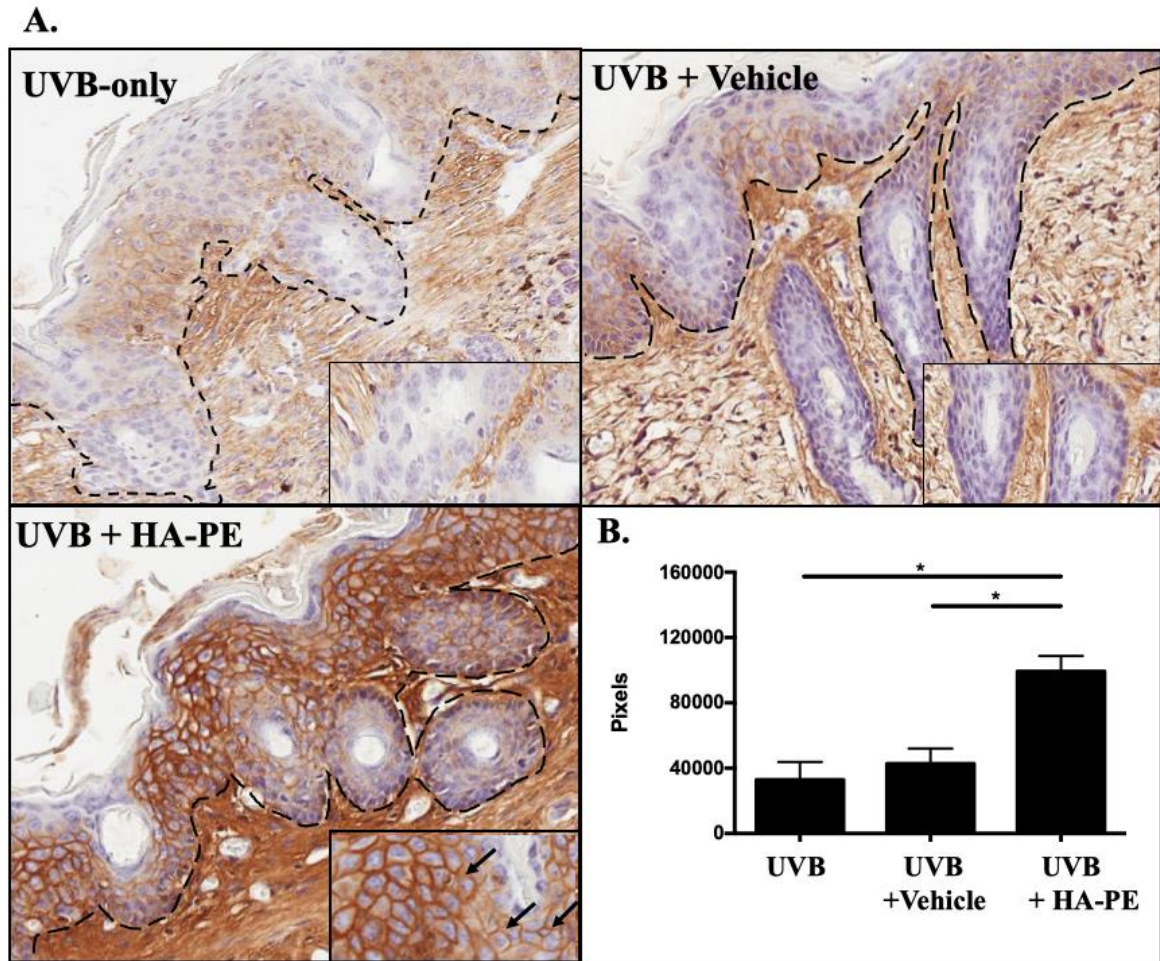


Figure 3: Detection of HA content in the interfollicular epidermis and hair follicles of *Ptch*^{+/LacZ}/*Hr*^{-/-} mice following 26 weeks of UVB exposure. A. HA-PE enhanced HA staining intensity in epidermal keratinocytes and hair follicle cells. Insets emphasize HA content in the hair follicles, with black arrowheads indicating HA expression on plasma membrane. Interfollicular epidermis and associated hair follicles are separated from the underlying dermis by the black dash line. HA content is detected using an HA-binding biotinylated protein and detected via DAB reagent (brown), followed by counterstaining with hematoxylin. **B.** Quantitative analysis of HA content detection in paraffin-embedded tissue sections. Intensity of immunoreactivity was measured using ImageJ and threshold against a negative control, established by omitting the HA-binding protein incubation, as a baseline. All values represent mean and SEM for a sample size of n=3 animals per group, with 5 replicates per animal (two-sample t test, * p<0.05).

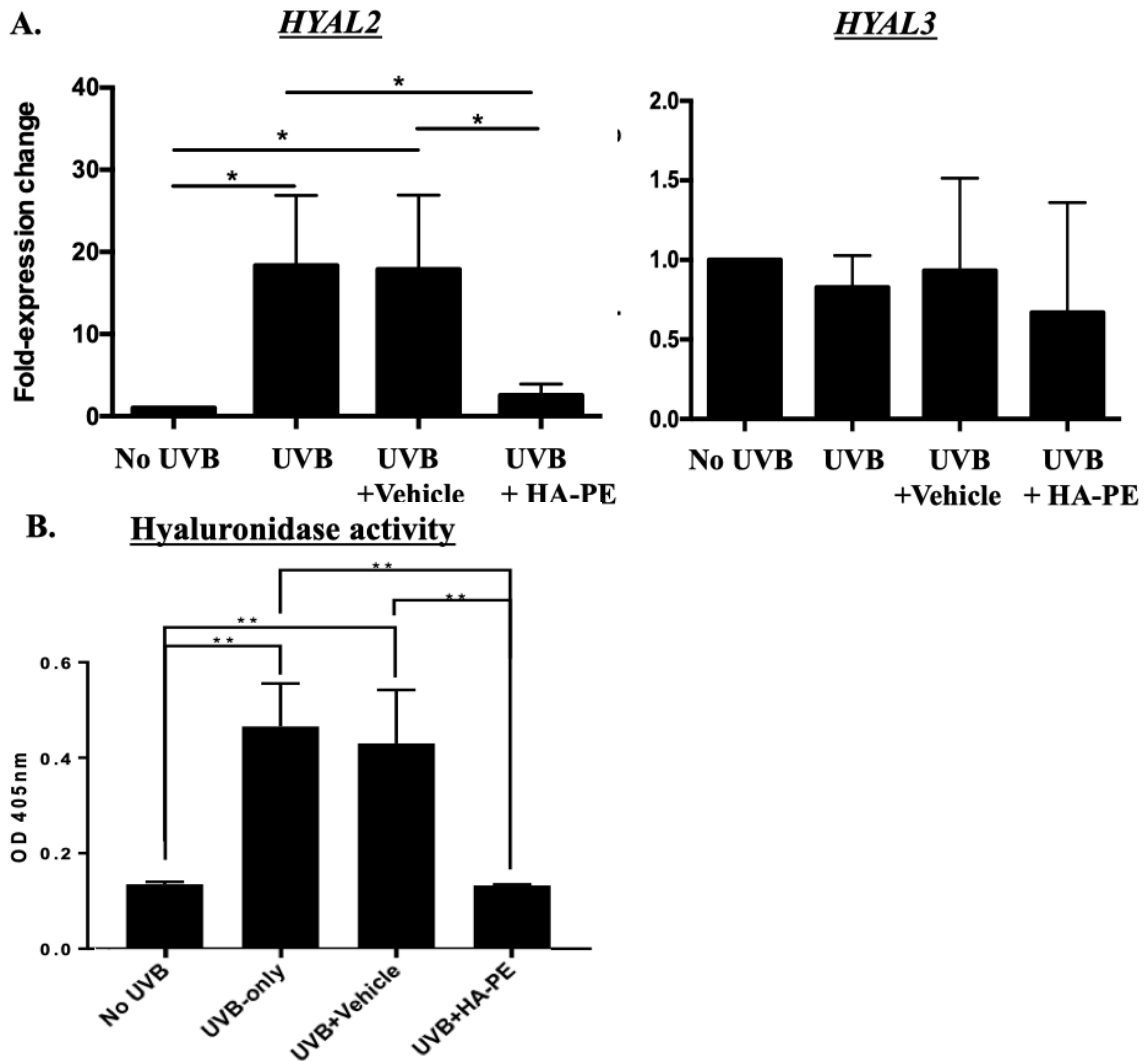


Figure 4: Effects of topical HA-PE administration on hyaluronidase expression and activity. **A.** *HYAL2* and *HYAL3* mRNA expression in susceptible mice after 4 weeks of UVB irradiation. HA-PE application significantly prevented UVB-induced *HYAL2* expression. No changes in *HYAL3* mRNA level were observed (n=3 animals/treatment group, 4 replicates; two-sample t-test, * p<0.05); **B.** Total hyaluronidase activity of murine skin biopsy samples after 4 weeks of irradiation, detected via an ELISA-like assay. Statistical significance was detected via one-way ANOVA, followed by Tukey's test (n=3 animals/treatment group, 3 replicates; ** p<0.01). For A. and B, all values are displayed as mean \pm SEM of samples.

3.2 Suppressive effects of HA-PE on sonic hedgehog signaling

To explore the role of epidermal HA accumulation in preventing keratinocyte tumor initiation, activation of the oncogenic driver pathway, sonic hedgehog signaling, was investigated in *Ptch*^{+/*LacZ*/*Hr*^{-/-} mice. The insertion of a promoterless *LacZ-neo* fusion gene replaced part of exon 1 and the entire exon 2 in *Ptch1*, thus producing a heterozygous loss-of-function mutation and allowing β -gal to be used as a marker for sonic hedgehog signaling, since *Ptch1* gene expression is induced by the activation of this pathway¹⁸⁶. HA-PE significantly prevented β -gal overexpression in the interfollicular epidermis (IFE) and hair follicles of UVB-exposed mice compared to both UVB- and vehicle-treated controls, which exhibit aberrant overexpression of β -gal in IFE, sebaceous gland, the bulge region and outer root sheath of hair follicles (Figure 5.A,B). To verify HA-PE mediated shutdown of this oncogenic pathway in the epidermis and associated epidermal structures, I next examined the expression pattern of GLI1, which is a hedgehog target and transcriptional factor that is a well-characterized indicator of sonic hedgehog signaling activation. Strong nuclear staining for GLI1 is evident in the epidermis and hair follicles of UVB- and vehicle-treated controls, indicating increased expression and nuclear translocation of this transcription factor. In comparison, HA-PE significantly restricted GLI1 expression and nuclear accumulation in the IFE and hair follicles back to non-irradiated control levels (Figure 6. A,B). GLI1 is minimally expressed in the ORS by both non-irradiated age-matched control and HA-PE treatment group, whereas aberrant expression is observed in all compartments of the hair follicle by UVB- and vehicle-control groups.}

Given *LacZ* insertion in susceptible mice does not affect the protein product of the second *Ptch* allele, functional tumor-suppressor at the cell membrane can still inhibit downstream sonic hedgehog signaling. Therefore, I investigated the expression of SHH, the ligand that binds and triggers PTCH1 endocytosis at the membrane. SHH expression was significantly reduced post-HA-PE treatment comparing to UVB-treated, vehicle-treated and non-irradiated controls (Figure 6. C). Taken together, these findings suggest topical HA-PE application substantially decrease inappropriate oncogenic sonic hedgehog signaling in the

epidermis of UVB-exposed susceptible mice, possibly through the inhibition of SHH expression. Since dysregulated hedgehog signaling often results in hyperproliferation^{29,46,66}, I next investigated the proliferative responses of keratinocytes to HA-PE application.

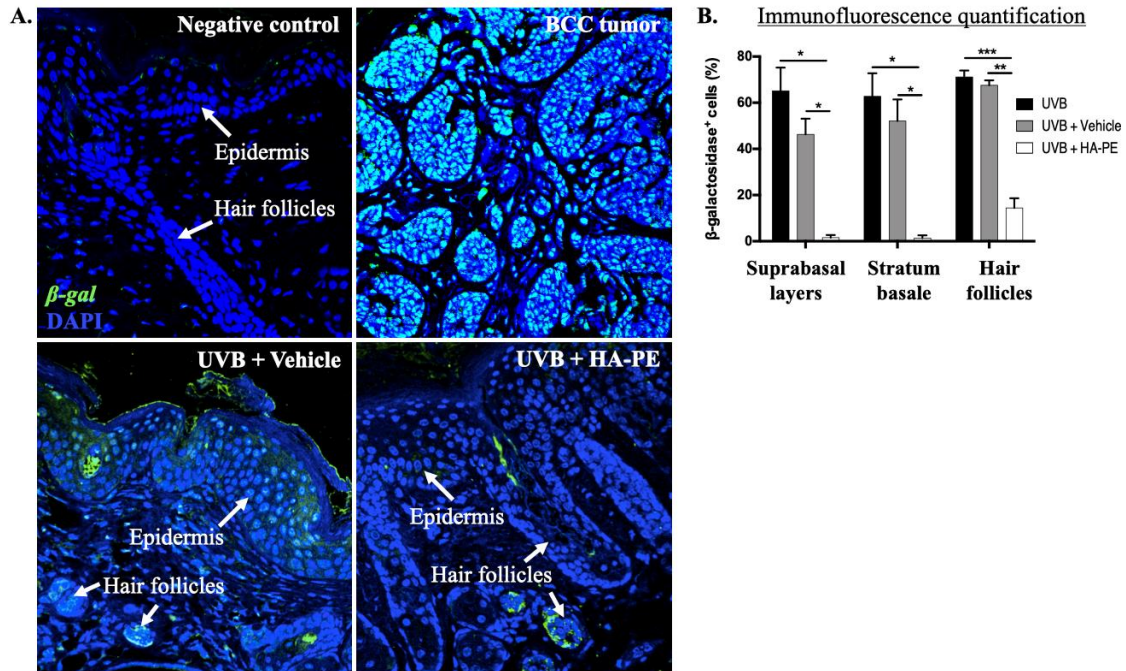


Figure 5: Suppressive effect of HA-PE application on UVB-induced BCC initiation using *E.coli LacZ* expression as a marker in susceptible mice. **A.** Immuno-staining of bacterial β -galactosidase (green) in murine skin sections counterstained with DAPI (blue). Negative and positive controls are established using a mouse that does not express the bacterial transgene and a tumor section from a *Ptch*^{+/*LacZ*};*Hr*^{-/-} mouse in the vehicle control group, respectively. HA-PE significantly prevented inappropriate expression of β -gal in the epidermis in susceptible mice subjected to 26 of chronic UVB irradiation; **B.** Quantitative analysis of β -galactosidase immuno-staining. Cells in the interfollicular epidermis and hair follicles were quantified based on positive immunoreactivity of bacterial β -gal through counting in QuPath. All values are displayed as mean \pm SEM of samples, and statistical significance was analyzed using two-sample t test (n=3 animals/treatment group, 5 replicates/animal; * p<0.05, ** p<0.01, *** p<0.001).

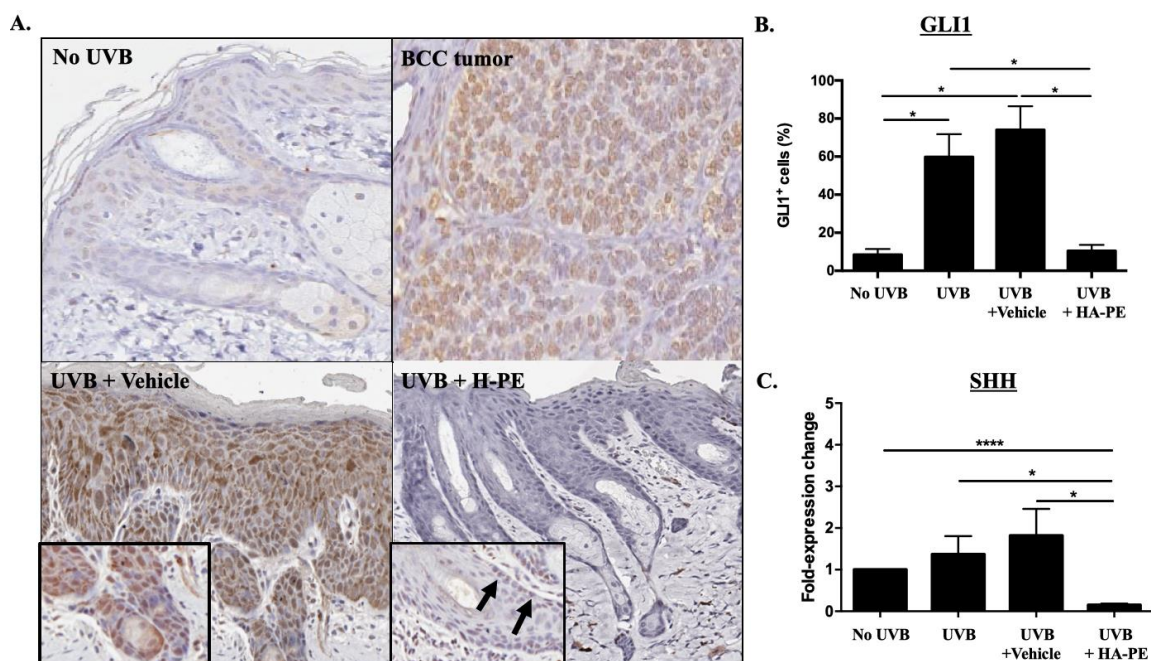


Figure 6: HA-PE prevents oncogenic sonic hedgehog signaling in UVB-exposed murine epidermis. **A.** Global prevention of inappropriate GLI1 expression and nuclear accumulation in susceptible mice receiving 26 weeks of irradiation following HA-PE administration. Slides are counterstained with hematoxylin and eosin (blue). Brown staining indicates positive GLI1 expression by DAB detection. Hair follicle structure is depicted in insets with black arrowheads indicating GLI1⁺ cells. **B.** Quantitative analysis of GLI1 in the interfollicular epidermis and hair follicles. GLI1 expression in each epidermal compartment was quantified by counting cells with positive GLI1 immunoreactivity in the nucleus using QuPath (n=3 animals/treatment group, 5 replicates/animals; two-sample t test, * p<0.05); **C.** SHH mRNA expression assessed through RT-qPCR. Epidermal enhancement of modified HMW-HA significantly reduced SHH expression in skin samples of susceptible mice exposed to 4 weeks of irradiation (n=3 animals/treatment group, 4 replicates/animal; two-sample t-test, * p<0.05, **** p<0.0001). For B. and C, all values are displayed as mean \pm SEM of samples.

3.3 HA- PE restricts cell cycle progression in susceptible mice

To elucidate the proliferative response of keratinocytes of UVB-exposed susceptible mice to HA-PE administration, I conducted immunohistochemistry of cyclin D1 and Ki67 on paraffin-embedded tissue sections (Figure 7, 8). Cyclin D1 is a target gene of sonic hedgehog signaling, and is often upregulated in BCC tumors and pre-neoplastic skin lesion following UVB irradiation¹⁹⁹. Quantification of immunohistochemistry demonstrated a significant reduction in cyclin D1 expression in the hair follicles by HA-PE (Figure 7.B) compared to UVB and vehicle controls, indicating prevention of UVB-induced proliferation. As an additional proliferation marker, Ki67 expression in hair follicles was quantified by immunohistochemistry (Figure 8.A). No difference of Ki67 expression was observed in the suprabasal and basal layer of the interfollicular epidermis between irradiated control, vehicle control and HA-PE treatment¹⁹². Instead, Ki67 expression in the hair follicle following HA-PE treatment was less than that of the UVB and vehicle controls (Figure 8.B), especially in the bulge region, where the cancer-initiating cytokeratin-15 positive stem cells reside (Supplemental Figure 2). Further, HA-PE treatment maintained the typical skin architecture of a distinctive stratum basale separated from suprabasal layers. In contrast, this organized tissue architecture is absent in irradiated controls (Figure 7 A), marked by the loss of a distinctive boundary between the stratum basale and suprabasal layers. Together, these findings predict HA-PE restricts the oncogenic potential of UVB-exposed hair follicles by inducing mitotic quiescence, possibly via regulating cyclin D1 expression to restrict G0/G1 progression. Since HA is an extracellular agent and requires receptor binding to induce intracellular signaling, I next examined the major HA receptor expression in UVB-exposed mice.

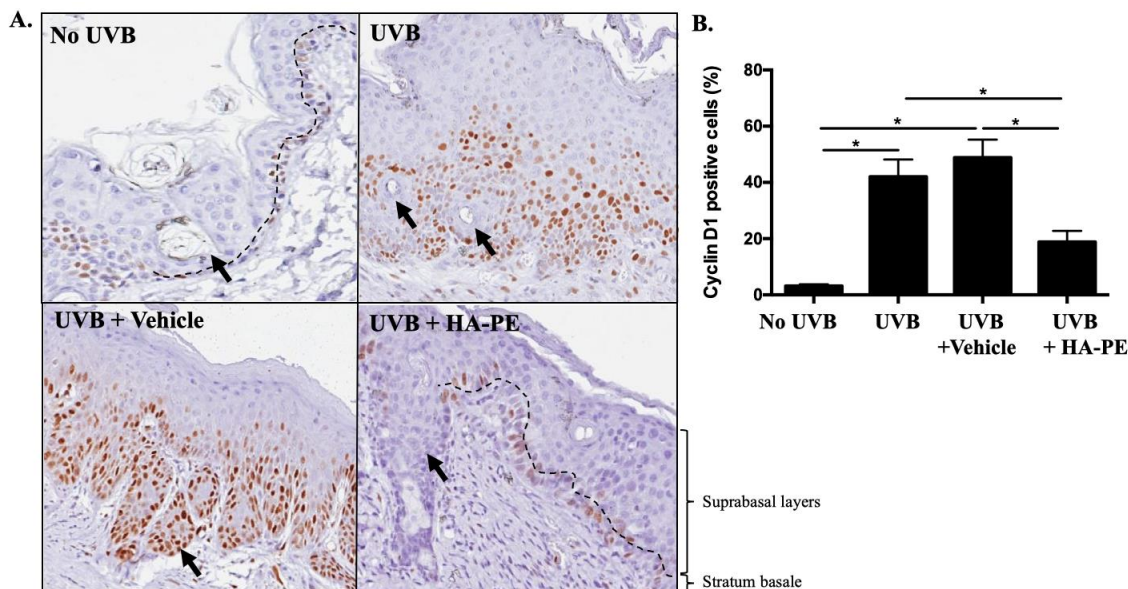


Figure 7: HA-PE promotes quiescence in hair follicles. **A.** Immunohistochemistry of Cyclin D1 expression in susceptible mice exposed to 26 weeks of irradiation. Slides were counterstained with hematoxylin (blue) with cyclin D1 detected via DAB (brown). HA-PE significantly prevented cyclin D1 overexpression in the hair follicles (black arrowheads) comparing irradiated controls. The distinct separation between suprabasal layers and stratum basale, a characteristic indicative of a homeostatic epidermis, is maintained by HA-PE (black dashed line separating suprabasal layers and stratum basale), whereas irradiated controls do not display clear boundaries between the basal and suprabasal layer. **B.** Quantitative analyses of cyclin D1 staining in hair follicles. Cells in each epidermal compartment positive for cyclin D1 expression were counted, and the percentage of cyclin D1 positive cells per animal was analyzed via two-sample t test (* $p < 0.05$, $n = 3$ animals/treatment group, 5 replicates/animal). All values are displayed as mean \pm SEM of samples.

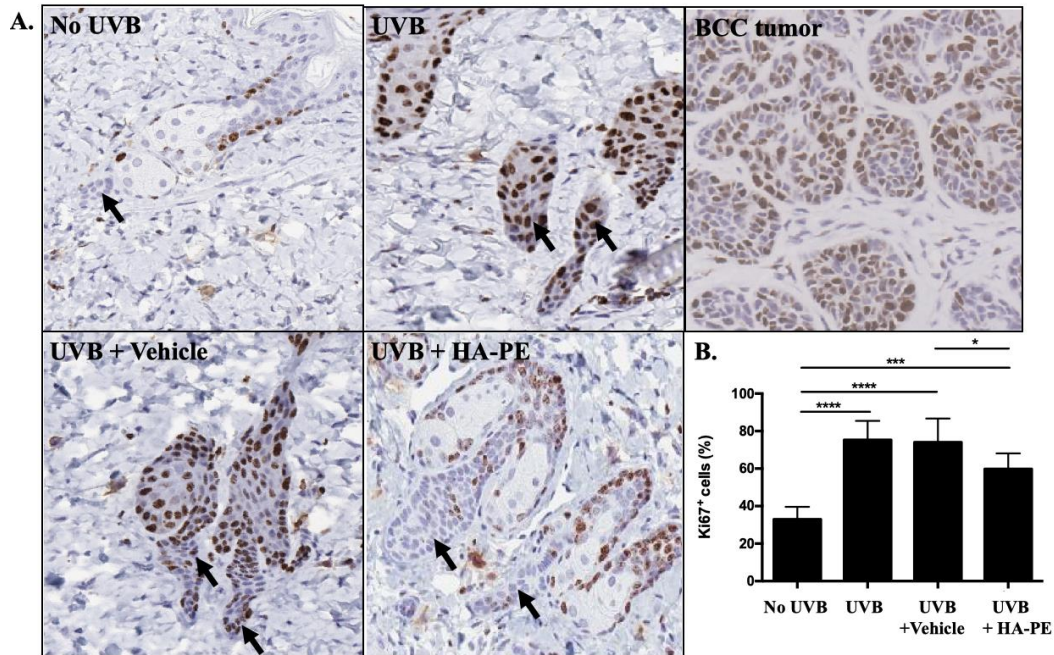


Figure 8: Immunohistochemistry analysis of Ki67 expression in hair follicles of UVB irradiated mice after HA-PE application. **A.** Immunohistochemistry of Ki67 (brown), showing decreased expression in the bulge region of hair follicles after HA-PE application in susceptible mice following 4 weeks of irradiation. Arrowhead indicates the bulge region where adult stem cells reside. **B.** Quantitative analyses of Ki67 staining in hair follicles. Ki67-positive cells in each image were counted in QuPath, and the percentages of Ki67⁺ cells per animal were analyzed via two-sample t test (* $p < 0.05$, *** $p < 0.001$, **** $p < 0.0001$; $n = 6$ animals/treatment group, 5 replicates/animal). All values are displayed as mean \pm SEM of samples.

3.4 CD44 and RHAMM expression in HA-PE treated skin

Since HMW-HA mediates downstream signaling through interaction with cell surface receptors, the expression of CD44 and RHAMM were examined. Immuno-staining demonstrated upregulated expression of pan-CD44 in the epidermis and hair follicles (Figure 9.A, B), whereas RHAMM expression was unaltered at both the protein and mRNA level (Figure 9.B, 10.B). To determine if specific CD44 isoform expression is altered by HA-PE administration, RT-PCR experiments were conducted using primers flanking the variable regions to identify alternatively spliced variants of CD44 (Figure 10.A). HA-PE administration resulted in upregulated CD44v3 isoform expression, which is characteristic of homeostatic keratinocytes (Figure 10.A). In contrast, no differences were observed in the CD44 standard form (CD44s, Figure 9.A) or variant isoforms (CD44v4, v8, v10) in UVB-exposed vehicle and HA-PE treated skin (Supplemental Figure 1). To investigate the connection between CD44, HA and prevention of sonic hedgehog signaling in susceptible mice, the signaling pathways modulating SHH expression were examined next.

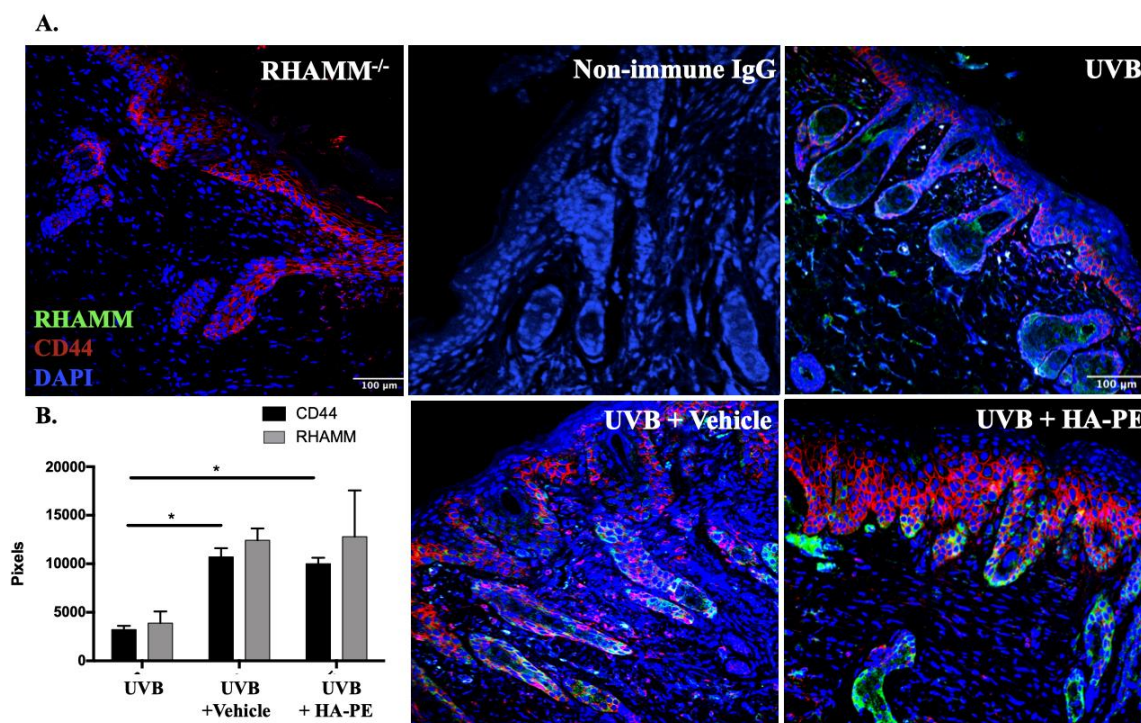


Figure 9: CD44 and RHAMM expression in chronically UVB irradiated epidermis following HA-PE application. **A.** Double immunofluorescent labelling of CD44 (red) and RHAMM (green) in epidermis using pan-antibodies. Slides were counterstained with DAPI shown in blue. *RHAMM*^{-/-} mouse skin section stained with both CD44 and RHAMM to establish a negative control to confirm antibody specificity. HA-PE application enhanced CD44 expression in the epidermis of susceptible mice after 26 weeks of irradiation, whereas RHAMM expression remains unaltered. In contrast to CD44, RHAMM is primarily expressed in sebaceous glands and the outer root sheath of hair follicles. **B.** Quantitative analysis of CD44 and RHAMM expression levels. Intensity of immunoreactivity in the interfollicular epidermis was quantified using ImageJ. All values are displayed as mean \pm SEM of samples (n=3 animals/treatment group, 5 replicates/animal; two-sample t test, * p<0.05).

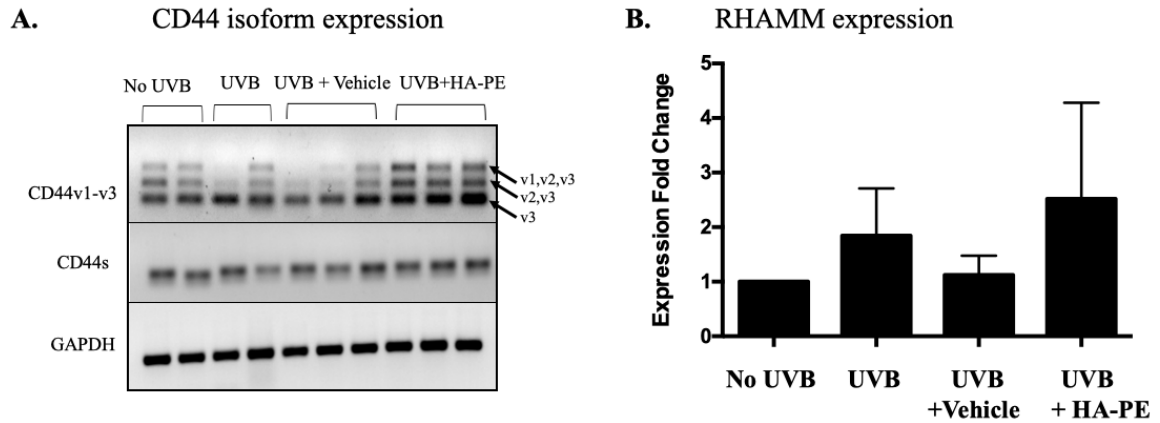


Figure 10: Alterations in HA receptor mRNA expression after HA-PE treatment. A. CD44v3 expression is increased by HA-PE in susceptible mice after 4 weeks of UVB irradiation. Black arrowheads indicate v3 expression (n=3 animals/treatment group, 3 replicates/animal. Experiment was repeated 3 times); **B.** mRNA expression level of RHAMM assessed by RT-qPCR. No statistically significant differences were observed between HA-PE and control groups (n=3 animals/treatment group, 4 replicates/animal; two-sample t test). For A. and B, all values are displayed as mean \pm SEM of samples.

3.5 Effects of HA-PE on NF- κ B signaling

Although current literature does not provide a direct connection between HMW-HA/CD44 interaction and sonic hedgehog signaling, HMW-HA/CD44 is a well-established negative regulator of canonical NF- κ B signaling^{121,140}, which is a pathway that can induce SHH expression to activate the oncogenic driver sonic hedgehog signaling^{174,175}. Moreover, mutational inactivation of *Hr* results in sustained inflammation driven by NF- κ B signaling, which accelerates BCC tumorigenesis in *Ptch*^{+/LacZ}/*Hr*^{-/-} mice¹⁸⁶. To explore the role of NF- κ B signaling in relation to HA-mediated inhibition of oncogenic sonic hedgehog signaling, nuclear localization of the p50 and p65 subunits were assessed through immunostaining analysis of paraffin-embedded tissue sections. HA-PE significantly prevented UVB-induced nuclear localization of p50 in the interfollicular epidermis and hair follicles of UVB-exposed mice (Figure 11). However, no difference in p65 localization was detected between vehicle control and HA-PE-treated mice as evident by its nuclear translocation. Since only p65 in the p65/p50 heterodimer possesses a trans-activating domain that can promote the expression of pro-inflammatory genes²⁰⁰, these results indicate that HA-PE does not suppress the canonical NF- κ B pathway. Therefore, I next assessed whether HA-PE suppressed UVB-induced DNA damage as a mechanism of tumor prevention.

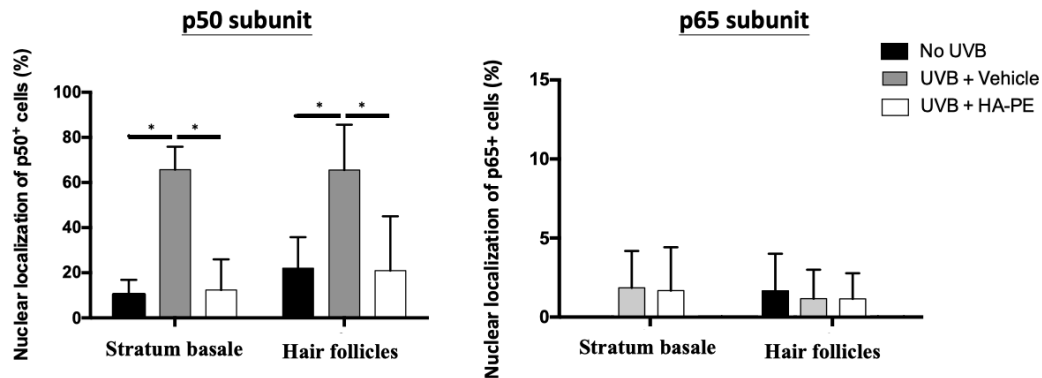


Figure 11: Nuclear NFκB localization in the epidermis of *Ptch*^{+/LacZ}/*Hr*^{-/-} mice after 4 weeks of UVB irradiation. HA-PE significantly prevented UVB-induced nuclear localization of both subunits in the interfollicular epidermis. However, this prevention of p65 localization was not unique to HA-PE application since vehicle control demonstrated similar suppressive effects. Quantitative analyses of p50 and p65 nuclear localization was conducted by counting cells exhibiting positive immunoreactivity in the nucleus. All cells in the interfollicular epidermis and hair follicles per image were quantified in QuPath. Statistical analysis was conducted using two-sample t test (n=3 animals/treatment group, 5 replicates/animal; * p<0.05). All values are displayed as mean ± SEM of samples.

3.6 Keratinocytes are not protected from DNA damage by HA-PE in susceptible mice

To investigate the potential genoprotective role of HMW-HA^{114-116,166-168}, on keratinocytes and adult stem cells in susceptible mice, DSBs and UVB-/ROS-signature mutations were quantified by immunohistochemistry and ELISA assays. Interestingly, the suppression of BCC initiation is not associated with a detectable reduction in DNA damage (Figure 12, 13). A significant increase in γ -H2AX foci formation in cells within the interfollicular epidermis and hair follicles was associated with UVB treatments, possibly due to the collapse of replication forks. However, a similar level of DSBs was observed in both the vehicle control and HA-PE-treated mice (Figure 12.A,B). To assess whether differences in ROS-induced and direct UVB-induced damage existed between the control and experimental groups, ELISA was performed to examine 8-oxo-dG and CPD formations in susceptible mice (Figure 13. A, B). Again, no significant differences in UVB- and ROS-induced DNA damage were detected between the irradiated vehicle control and HA-PE-treated group. Vertical lineage tracing of proliferating progenitor cells originating from the stratum basale was used as a preliminary method to assess DSB repair activity in the epidermis. However, these analyses demonstrated no significant differences between all experimental groups (Figure 12. C). predicting similar repair activities between control and experimental groups are similar. Collectively, these findings demonstrate that the mice receiving HA-PE treatment exhibit a similar DNA damage load in IFE and hair follicles as the UVB- and vehicle-treated controls, and that differences in DNA damage, and potentially mutational load, do not account for HA-PE suppression of BCC. Since the accumulation of DNA damage may overwhelm the repair machinery and trigger programmed cell death, I next examined apoptosis as a potential mechanism in the removal of these harmful cells.

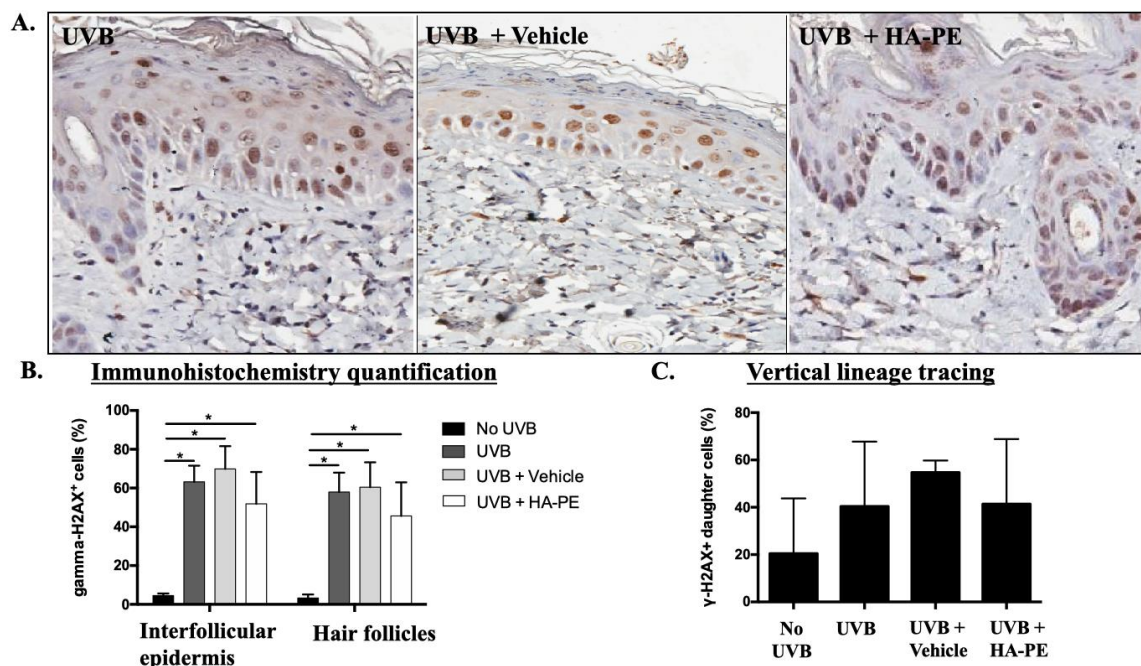


Figure 12: HA-PE does not alter the double-stranded breaks in the epidermis of susceptible mice after 4 weeks of UVB irradiation. **A.** Immunohistochemistry of γ -H2AX in paraffin-embedded tissue counterstained with hematoxylin (blue). Brown staining is indicative of γ -H2AX foci formation. **B.** Quantitative analysis of γ -H2AX foci, a marker for double-stranded DNA breaks, in the epidermis and hair follicles. Cells in the interfollicular epidermis with strong γ -H2AX immunoreactivity were quantified, and the percentage of γ -H2AX positive cells in each epidermal compartments were analyzed for statistical significance. However, foci formation is not significantly different between control and treatment groups; **C.** Vertical lineage tracing of damage-sustaining progenitor cells and γ -H2AX⁺ daughter cells in the interfollicular epidermis. The percentage of daughter cells positive for γ -H2AX foci within a lineage was quantified through QuPath by counting. For B, and C, two-sample t test was conducted to assess statistical significance (* $p < 0.05$; $n = 3$ animals/treatment group, 5 replicates/animal). All values are displayed as mean \pm SEM of samples.

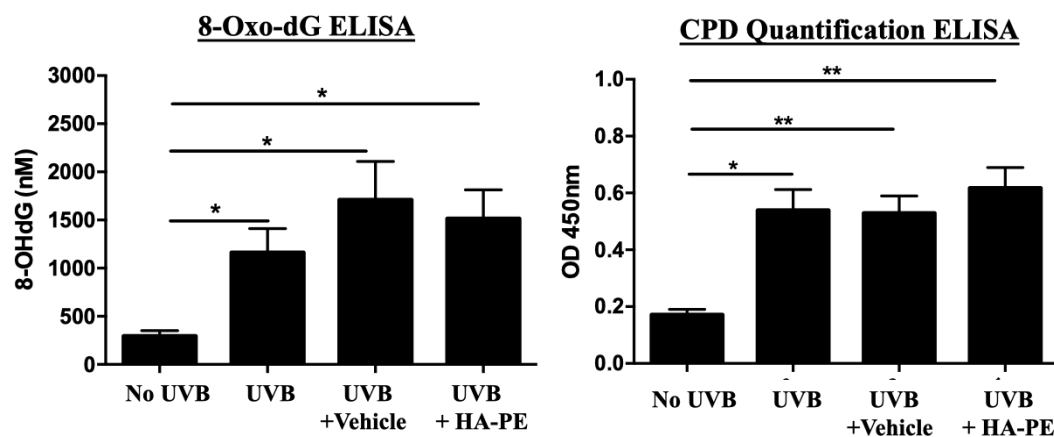


Figure 13: ROS- and UVB-induced DNA damages are not altered by HA-PE application following 4 weeks of irradiation. ROS/UVB-induced DNA damages are measured by the ROS-adduct 8-oxo-dG and cyclobutane pyrimidine dimer (CPD) formation in extracted DNA, respectively. No statistically significant difference in DNA damages are observed between irradiated, vehicle-treated controls, and HA-PE treated group. Statistical analysis was conducted by two-sample t test, experiments were repeated 3 times (* $p < 0.05$, ** $p < 0.01$; $n = 3$ animals/treatment group, 5 replicates/animal). All values are displayed as mean \pm SEM of samples.

3.7 HA-PE application promotes selective apoptosis in hair follicles

BCL2 is a pro-survival protein and a target gene that is upregulated by sonic hedgehog signaling in BCC tumorigenesis, and is often over-expressed to facilitate cancer cell survival by preventing cytochrome c release from the mitochondria^{201,202}. To elucidate whether apoptosis contributes to HMW-HA-mediated resistance against BCC initiation, I first quantified BCL2 expression in the epidermis and hair follicles of susceptible mice. Expression of epidermal and follicular BCL2 was suppressed following HA-PE application in UVB-irradiated mice, whereas UVB- and vehicle-treated controls exhibited an elevation of this pro-survival protein in the epidermis and hair follicles (Figure 14). BCL2 is an early participant in the apoptosis cascade²⁰². To verify these results and to establish whether keratinocyte apoptosis is altered by HA-PE, TUNEL assay, which marks late-stage apoptosis, was quantified. Interestingly, HA-PE promotes apoptosis in cell subsets within the outer root sheath and bulge of hair follicles, where the K15⁺ stem cells that are known to be cancer-initiating in the *Ptch*^{+/LacZ} mouse model reside (Supplemental Figure 2)^{58,60-62}. Apoptosis in these hair follicle regions was uniquely observed in HA-PE treatment, whereas control groups only exhibited apoptosis of suprabasal keratinocytes near the stratum corneum that is typical of normal keratinocyte turnover (Figure 15).

To further identify the nature of these hair follicle stem cells, I double-labeled paraffin-embedded tissue sections with a marker for BuSCs, K15, together with a marker for apoptosis, caspase 3. Immunofluorescent co-localization analyses demonstrated that 40% of total K15⁺ cells in the hair follicles are apoptotic, as indicated by positive caspase 3 expression at week 26 of irradiation (Figure 16.A,B). Consistent with these data, K15⁺ cells were continuously lost between week 6 and 26 following HA-PE administration, while the number of K15⁺ cells in non-irradiated, UVB-exposed and vehicle controls remained constant (Figure 16.C). Given K15 is a well-established marker of BuSCs^{61,203,204} that can give rise to BCC^{58,60,62}, these data suggest HA-PE promotes the removal of these K15⁺ stem cell via apoptosis as a mechanism of cancer prevention. To verify K15⁺ cells are the cancer-initiating cells in this model, I next investigated the origin of tumors through examining the histopathology of identified BCCs in *Ptch*^{+/LacZ/Hr}^{-/-} mice.

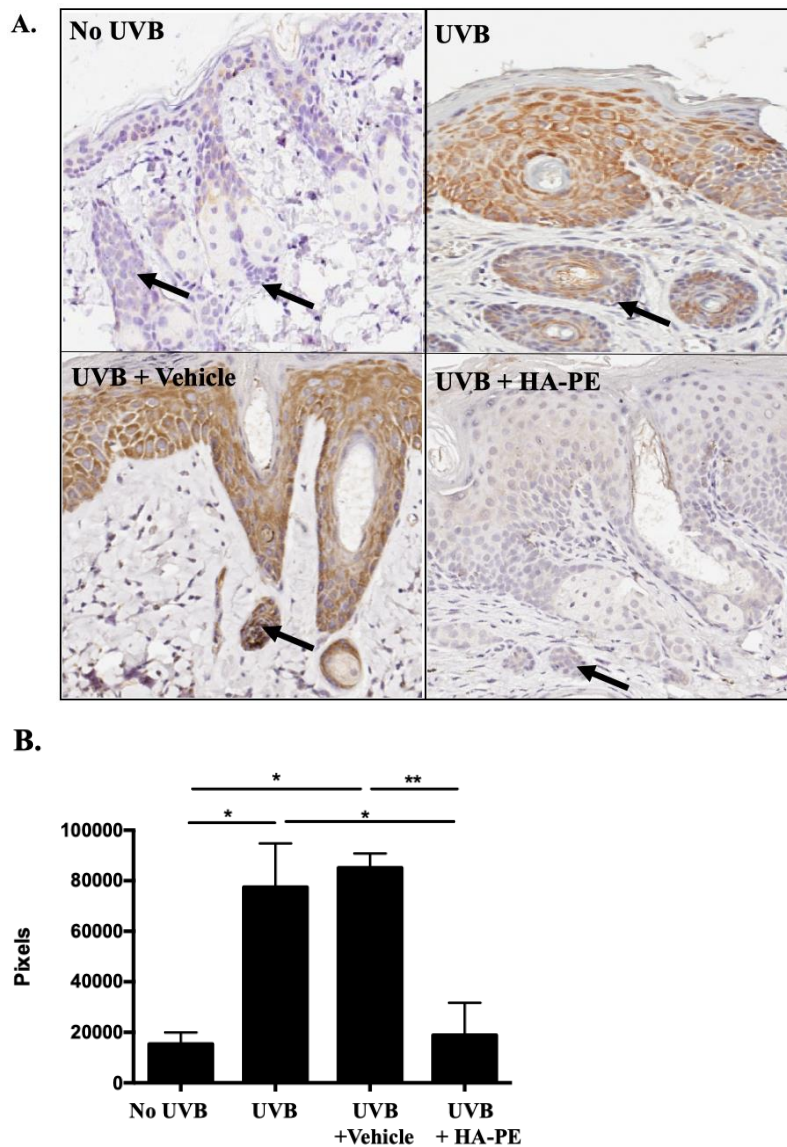


Figure 14: HA-PE reduces pro-survival BCL2 expression in the interfollicular epidermis and hair follicles of susceptible mice after 26 weeks of UVB irradiation. A. Immunohistochemistry of BCL2 detected via DAB (brown). Black arrowheads indicate BCL2⁺ cells in the bulge of hair follicles; **B.** Quantitative analyses of BCL2 expression in the epidermis and hair follicles. Percentage of cells positive for BCL2 immunoreactivity in the interfollicular epidermis and hair follicles was quantified via counting in QuPath. All values are displayed as mean \pm SEM of samples, and analyzed using two-sampled t test (* $p < 0.05$, ** $p < 0.01$; $n = 3$ animals/treatment group, 5 replicates/animal).

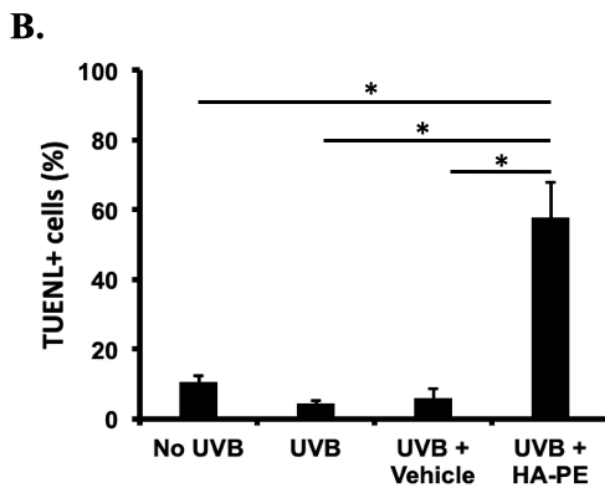
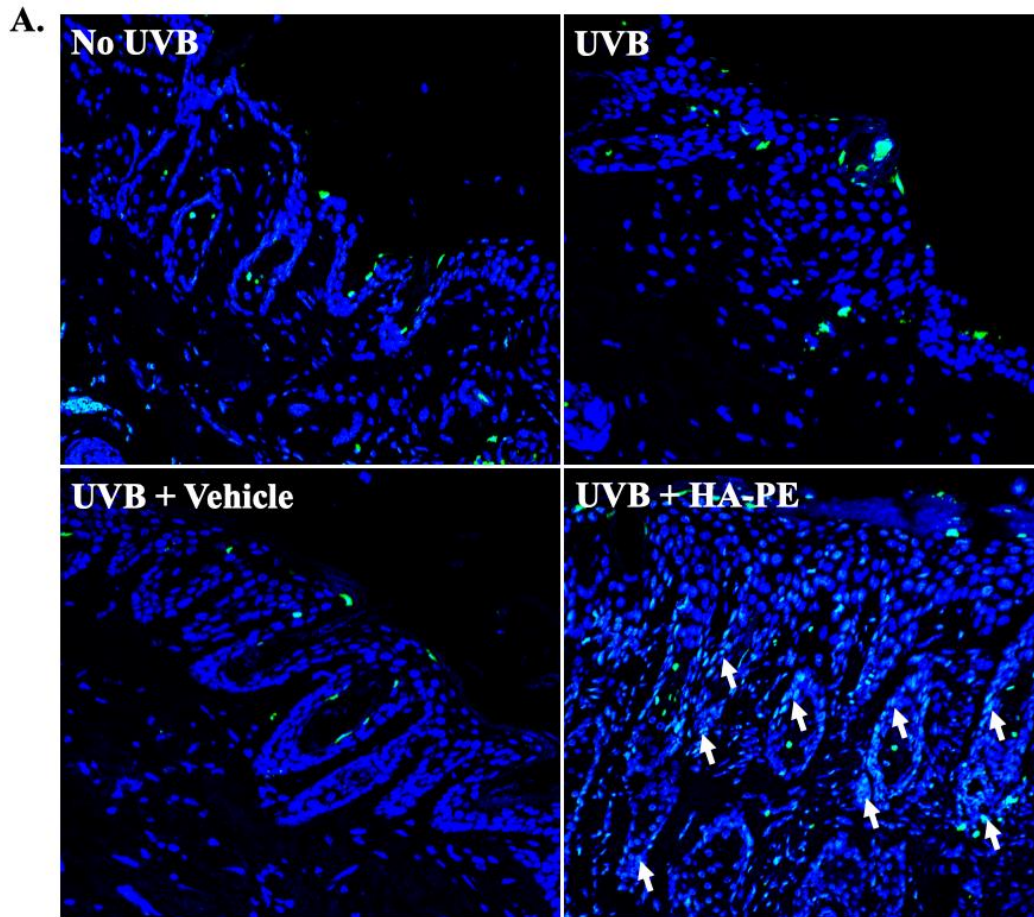


Figure 15: HA-PE enhances apoptosis in the outer root sheath and bulge region of hair follicles of mice following 26 weeks of irradiation. A. TUNEL analysis of paraffin-embedded tissue. Apoptotic cells are labeled in green and counterstained with DAPI (blue). White arrowheads indicate apoptotic cells in hair follicles; **B.** Quantitative analysis of

apoptotic cells in the hair follicle. Five images were taken per sample, and the percentage of apoptotic cells in was quantified through counting cells with green fluorescence per image. All values are displayed as mean \pm SEM of samples. Two-sample t test was conducted to assess significance (* $p < 0.05$, $n = 3$ animals/treatment group, 5 replicates/animal).

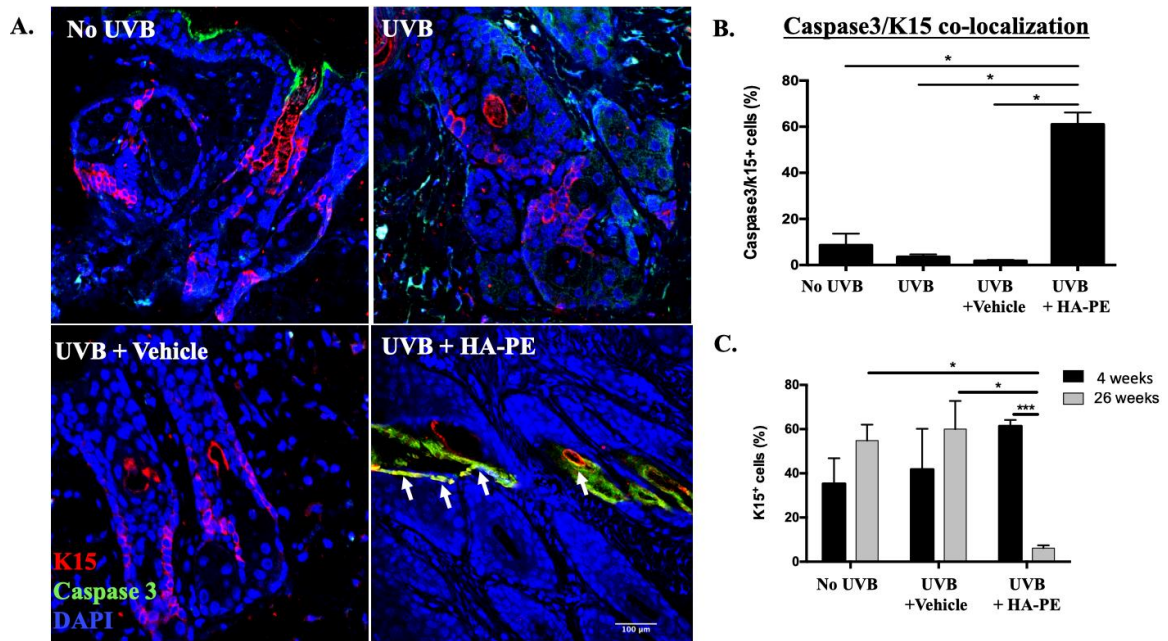
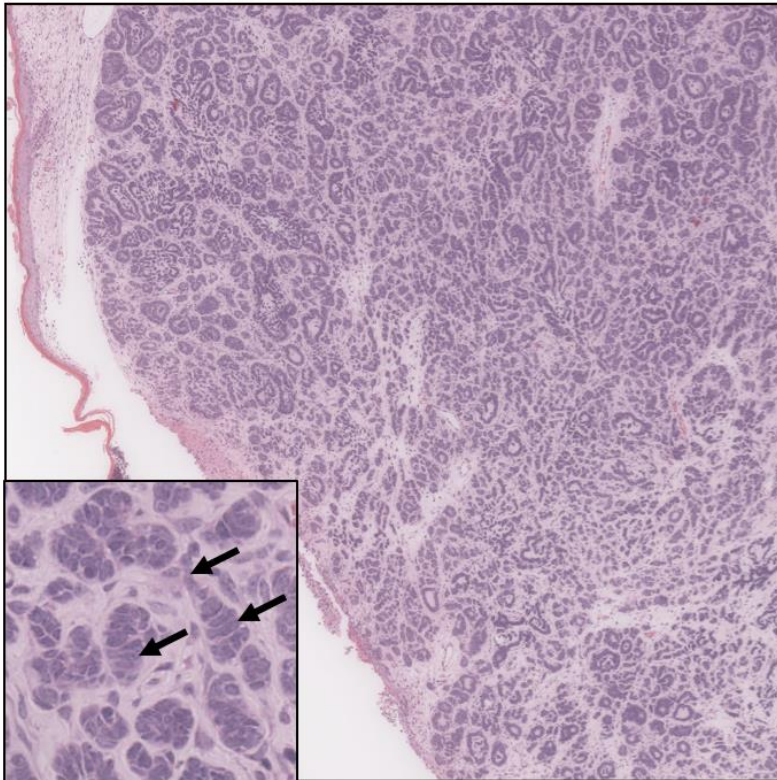


Figure 16: HA-PE enhances apoptosis in K15⁺ adult stem cells in hair follicles of UVB-irradiated susceptible mice. **A.** Double-labeled immunofluorescent analysis of K15 (red) and caspase 3 (green), counterstained with DAPI (blue). White arrowheads indicate co-localization of K15 and caspase 3 in hair follicles of *Ptch*^{+/*LacZ*}/*Hr*^{-/-} mice after 26 weeks of irradiation; **B.** Quantitative analyses of immunofluorescent staining. All K15 cells positive for caspase 3 staining in hair follicles were counted, and analyzed via two-sample t test (* $p < 0.05$; $n = 3$ animals/treatment group, 5 replicates/animal); **C.** Number of K15⁺ cells in hair follicles of susceptible mice after 4 and 26 weeks of irradiation. Cells displaying positive immunoreactivity for K15 in each image were counted (approximately 500 cells per image) and analyzed via two-sample t test (* $p < 0.05$, *** $p < 0.001$; $n = 3$ animals/treatment group, 5 replicates/animal). For B. and C, all values are displayed as mean \pm SEM of samples.

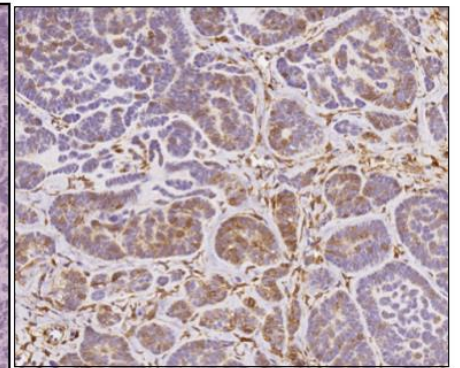
3.8 Immunohistochemical analysis of UVB-induced BCC tumors in *Ptch*^{+/*LacZ*}/*Hr*^{-/-} mice

To elucidate the epidermal compartment and verify the cancer-initiating cell of BCC tumorigenesis in our mouse model, I examined the histopathology of paraffin-embedded macroscopic tumor sections from the two control groups as described previously^{58,62}. BCC tumors driven by *Ptch1* loss are characterized by a radiating, branching organization reminiscent of hair follicle differentiation in this model. These micronodular tumors displayed scarce stroma and sparse blood vessels, with cells organized into irregularly shaped nests. In certain portions of the tumor, elongated or spindle-like cells with a minimal degree of nuclear palisading were observed (Figure 17.A, inset), while a prominent cleavage was present between surrounding connective tissue and tumor stroma (Figure 17. A). Interestingly, BCCs originating from the follicles often display inappropriate myoepithelial differentiation, as seen in sporadic human BCC and susceptible mouse models^{62,205,206}. Since smooth muscle actin (SMA) is a well-established marker for myoepithelial differentiation, I therefore conducted immunohistochemistry to examine SMA expression in macroscopic BCC tumors. Strong intracytoplasmic SMA immunoreactivity is detected in BCCs and hair follicles of UVB-exposed tumor-adjacent skin, but was absent in the stratum basale and suprabasal layers of *Ptch*^{+/*LacZ*}/*Hr*^{-/-} mice (Figure 17.B,C). Interestingly, a direct association between these keratinocyte tumors and hair follicles was often observed. Rare initial phases of this keratinocyte tumor originating from the bulge region (Figure 17.D) and ORS (Figure 17. D, inset) of hair follicles were detected in irradiated *Ptch*^{+/*LacZ*} mice, with strong K15 immunoreactivity in peripheral cells. Similarly, K15 expression was also detected in the peripheral cells of tumor nests in macroscopic BCCs identified as BCC by pathologists (Figure 17.E). Together, these data suggest that the UVB-induced BCCs in *Ptch*^{+/*LacZ*}/*Hr*^{-/-} mice are associated with the hair follicles, and likely originate from the K15⁺ adult stem cells that are present in the bulge and ORS regions.

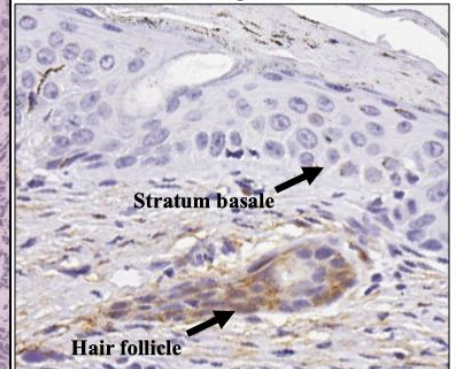
A. H&E



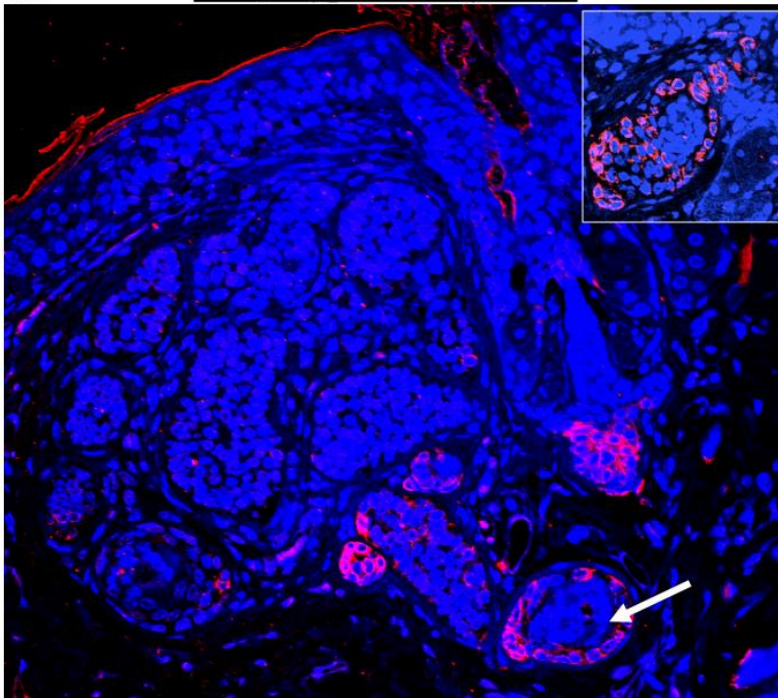
B. α -SMA, macroscopic BCC



C. α -SMA, adjacent skin



D. K15, atypical outgrowth



E. K15, macroscopic BCC

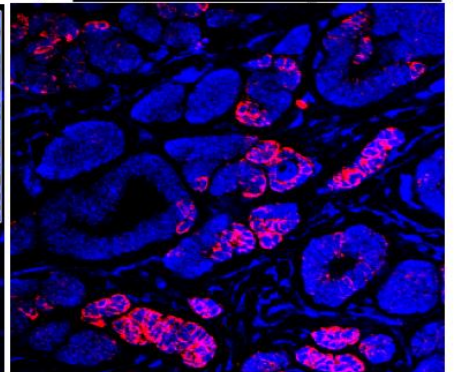


Figure 17: Immunohistochemistry analyses of UVB-induced BCC tumors. **A.** UVB-induced BCCs in *Ptch*^{+/*LacZ*/*Hr*^{-/-} mice are characterized by irregularly shaped nests organized in a radiating pattern, with scarce stroma and blood vessels. Insets and arrowheads show elongated cells in small, irregular nests with minimal nuclear palisading. **B.** Expression pattern of smooth muscle actin (SMA) in macroscopic BCC tumors. SMA was present in both the tumor stroma and the cytoplasm of tumor cells. **C.** Strong SMA expression detected in the tumor-adjacent hair follicle of UVB-exposed vehicle control. No SMA immunoreactivity was observed in stratum basale or suprabasal epidermis. **D.** BCC tumors in *Ptch*^{+/*LacZ*/*Hr*^{-/-} mice are directly associated with the hair follicles. Rare initial stages of BCC exhibit atypical outgrowth arising from the approximate region of the bulge (white arrowhead) or outer root layer sheath (inset) that are focally-positive for K15 expression (red). **E.** K15 expression (red) in macroscopic BCCs. Similar to K15 expression in the atypical outgrowth originating from hair follicles, peripheral cells in macroscopic BCC are strongly positive for K15 immunoreactivity.}}

Chapter 4

4 Discussion

4.1 HA-PE phenocopies the cancer-resistant naked mole-rat to prevent carcinogenesis in susceptible mice

Once thought to be an inert component of the ECM, HA is now recognized as a dynamic molecule that facilitates extracellular protein-protein interaction and intracellular signaling^{106,131,146}. The loss of native HA in epidermis is characteristic in aging, inflammation, chronic UV exposure, and tumorigenesis^{106,107,118}. Previous studies report HMW-HA accumulation elicits suppressive effects on murine astrocytoma and colon carcinoma xenograft tumor growth^{169,170}. Further, HMW-HA arrests breast cancer cell growth *in vitro* and spheroid growth, marked by downregulated cyclin D1 and PCNA expression^{95,176}. To our knowledge, this is the first study to examine the effects of epidermal HMW-HA enhancement on keratinocyte carcinoma initiation. I demonstrated hyaluronan-phosphatidylethanolamine polymers (HA-PE) significantly increase large HA polymer content in the epidermis (Figure 3). HA-PE application suppresses hyaluronidase activity and *HYAL2* expression (Figure 4), an extracellular hyaluronidase that degrades native HA, predicting the accumulated epidermal HA is the high molecular-weight species. Moreover, the topical application of HA-PE prevented UVB-induced histologically-detectable BCC tumor initiation as detected by histology and inhibition of and significantly blocked *Ptch1* promoter expression in susceptible mice (Figure 5).

Previous *in vivo* and cell studies demonstrate sonic hedgehog hyperactivation drives BCC tumorigenesis^{28,29,33,207}, and its inhibition leads to reduced proliferative capacity and tumor growth^{208,209}. Specifically, animal studies suggest sonic hedgehog signaling driven by loss-of-function mutation in *Ptch1* directly causes BCC originating from the bulge^{58,60,62}, but an IFE with hyperactive sonic hedgehog signaling may also constitute a permissive microenvironment for BCC initiation^{58,59,61}. Moreover, HA is a recognized agent in mediating maintenance and support of stem-cell niches, including the bulge within hair

follicles²¹⁰. In association with HA accumulation, we show that β -gal staining measuring *Ptch1* promoter expression is significantly reduced in the IFE and hair follicles (Figure 5), indicating suppression of sonic hedgehog signaling in UVB-exposed *Ptch1*^{+/-} mice. The expression and nuclear translocation of the transcriptional factor GLI1, another well-established marker for sonic hedgehog activation, is similarly suppressed by HA-PE in IFE and follicles (Figure 6.A,B). Decrease in sonic hedgehog signaling is further verified by assessing target gene *CNND1* (Figure 7) and *BCL2* (Figure 14) expression, which were significantly diminished in susceptible mice after HA-PE application. Interestingly, HA-PE reduced the activating ligand SHH expression (Figure 6.C), suggesting a mechanism of suppressing the hedgehog pathway. Taken together, our data predict HA-PE prevents UVB-induced BCC by inhibiting aberrant sonic hedgehog signaling in two epidermal compartments: the hair follicle bulge, and the IFE. HA-PE targets SCs in the bulge via restricting sonic hedgehog signaling to a level similarly observed in non-irradiated controls, and limits the tumorigenic potential of stem cells in stratum basale via preventing sonic hedgehog signaling in IFE.

This prevention of tumorigenicity was associated with restricted cyclin D1 and Ki67 expression in the hair follicles of susceptible mice (Figure 7, 8). *CCND1*, a target gene of sonic hedgehog signaling and mediator of G1-S progression, was significantly restricted but not extinguished in the hair follicles (Figure 7), thus further verifying decreased sonic hedgehog signaling following HA-PE application. Similarly, Ki67 expression was also significantly reduced by HA-PE application in the bulge region of hair follicles, where the adult stem cells reside (Figure 8). Together, these data predict HA-PE promotes mitotic quiescence in UVB-irradiated hair follicles to limit their oncogenic potential.

In naked mole-rats, large HA polymers are also protected from degradation by reduced extracellular hyaluronidase activities⁹⁴. HMW-HA accumulation confers cancer resistance in this species via promoting contact inhibition hypersensitivity through inducing cyclin-dependent kinase inhibitor p16^{INK4A/B} expression^{94, 95}, thereby promoting quiescence *in vitro* as reflected by the decreased PCNA expression⁹⁵. The effects of HA-PE reported here therefore phenocopy the properties of HMW-HA in the long-lived rodent naked-mole rat by increasing HA polymer accumulation, downregulating hyaluronidase activity, inducing

relative mitotic quiescence, and exerting an anti-tumorigenic effect. However, the protein isoform (p16^{INK4A/B}) responsible for ECI in naked mole-rats is not expressed in mice^{93,94}. Thus, further examinations of mammalian contact inhibition pathways (i.e: Hippo/YAP) may shed new lights on the involvement of contact inhibition in the prevention of keratinocyte carcinogenesis. Moreover, HA-PE elicited apoptotic responses in the known cancer-initiating subpopulation of adult stem cells in this susceptible model, whereas HMW-HA produced by *H. glaber* was reported to induce apoptosis in breast cancer cells non-specifically⁹⁵. To my knowledge, the effects of *H. glaber* HMW-HA on cancer stem cells have not been investigated. Here, the promotion of mitotic quiescence and apoptosis appear to be linked to an effect of HA-PE on sonic hedgehog signaling, as cyclin D1 and BCL2 are target genes of this oncogenic signaling pathway.

To begin to identify the mechanisms behind HA-PE block in hedgehog signaling and BCC initiation, I examined the expression of the major HA receptors in keratinocyte. CD44 is the major keratinocyte HA receptor^{133,135} and is a promising target in facilitating the tumor suppressive effect of HA-PE because CD44 mediates the cancer resistance of HMW-HA in naked mole-rats^{94,95}. Moreover, CD44 is essential for several HMW-HA-mediated suppression of proliferation^{126,138}, tumor growth^{126,169,170}, and invasion^{125,157}. Keratinocytes in homeostatic epidermis primarily express CD44v3-v10, with v3 being the most prominent isoform¹³⁵. Here, we report that HA-PE increased CD44 protein expression in the epidermis and hair follicles (Figure 9) and maintained CD44v3 isoform expression, which is characteristic of homeostatic keratinocytes (Figure 10.A) that was lost in UVB exposed controls. In addition, immunohistochemistry demonstrated that the interfollicular epidermis of HA-PE treated mice retained a distinct stratum basale and organized suprabasal layers following UVB exposure. In contrast, this tissue architecture indicative of a homeostatic epidermis was lost in irradiated controls, as the stratum basale cannot be distinguished from suprabasal layers in the epidermis (Figure 7.A). Taken together, the findings here predict epidermal HA maintains homeostasis in the interfollicular epidermis via promoting CD44v3 isoform expression and maintaining the appropriate epidermal architecture. Since CD44 is the primary receptor that is responsible for the HA-mediated cancer resistance in naked mole-rats^{93,94}, it is possible that HA-PE exerts its anti-tumorigenic effects through interaction with CD44 in the epidermis and hair follicles.

4.2 HA-PE mediated suppression is not orchestrated through canonical NF- κ B signaling

A direct effect of CD44 on sonic hedgehog pathway activity has not been previously reported to my knowledge. However, HMW-HA/CD44 signaling is a well-established inhibitor of canonical NF κ B signaling, a pro-inflammatory pathway that promotes SHH expression and activation of sonic hedgehog signaling^{174,175}. Previous studies report canonical NF κ B signaling, activated by the p65/p50 heterodimer, is essential for skin carcinogenesis in mice^{75,186}. For example, the p65 inhibitor SSZ significantly reduces the nuclear translocation of canonical NF κ B and UVB-induced BCC tumor load in *Ptch*^{+/LacZ}/*Hr*^{-/-} mice, although SSZ does not completely prevent tumor initiation in these susceptible mice¹⁸⁶. Unexpectedly, HA-PE did not alter p65 nuclear translocation (Figure 11), possibly due to altered receptor clustering at the membrane. Since canonical NF κ B signaling requires the dimerization and translocation of p65/p50 subunits, the lack of difference in p65 translocation suggests that canonical NF κ B signaling was not significantly affected by HA-PE treatment. In contrast, p50 nuclear translocation in susceptible mice was significantly prevented by HA-PE application relative to UVB-exposed vehicle control (Figure 11), predicting suppression of the non-canonical NF κ B pathway. Nuclear p50 homodimer accumulation and constitutive kappaB-binding mediated by non-canonical signaling are characteristic of skin neoplasms in mice^{211,212}. In *Ptch*^{+/LacZ}/*Hr*^{-/-} mice, non-canonical NF κ B signaling is reported to accelerate tumor growth by creating a pro-inflammatory microenvironment, and augment BCC pathogenesis through upregulating the activating ligand SHH expression to sustain sonic hedgehog signaling²¹². It is well-established that the p50 subunit does not contain a trans-activating domain. Therefore, an additional trans-activator, such as BCL3, is required for p50 homodimer to acquire transcriptional activity^{212,213}. BCL3 overexpression is associated with stabilization of the p50 homodimer in squamous cell carcinoma²¹¹, and enhanced BCL3 activity is associated pathogenesis of various neoplasms^{214,215}. Moreover, BCL3 knockdown significantly reduces PTCH1, GLI1 and GLI2 expression in murine BCC cells, thus predicting crosstalk between the two pathways²¹². In this context, HA-PE may suppress sonic hedgehog signaling by preventing non-canonical NF κ B-induced SHH

expression²¹². Future experiments should be conducted to investigate the role of HMW-HA, CD44 and possibly other HA receptors (i.e: Toll-like receptors) in modulating the non-canonical NFκB pathway in the context of BCC tumorigenesis, and further examine the relationship between p50 homodimers and sonic hedgehog signaling.

4.3 HA-PE promotes apoptosis of DNA-damaged K15⁺ cancer-initiating stem cells in hair follicles

UVB is a well-documented environmental carcinogen that threatens genome integrity via directly inflicting structural alterations in DNA, such as promoting dimer formation also add ROS damage, which is not a direct effect. Mice and humans employ various strategies to ensure genome integrity against UVB insults, such as the production of UV-absorbing pigments, expression of anti-oxidants, and repair mechanisms including base and nucleotide excision repair^{67,68,76}. However, these mechanisms do not completely protect DNA from UV, and damage accumulation is regarded as the primary skin carcinogen^{69,71}. Previous studies have characterized HMW-HA as a genoprotective agent by its ability to scavenge epidermal ROS. For example, HMW-HA reduced γ-H2AX foci formation, intracellular ROS levels, and damage-induced apoptosis of human corneal and alveolar epithelial cells^{114,171,172}. It is therefore surprising that HA-PE-mediated suppression of BCC is not associated with reduced DNA damage in UVB-exposed mice (Figure 12, 13). No significant differences were observed in γ-H2AX foci formation, nuclear DNA-associated ROS adduct 8-oxo-DG, and UVB-induced CPD in UVB controls and HA-PE treated epidermis and hair follicles. As a preliminary assessment of DSB repair in the epidermis, I performed a vertical lineage tracing of proliferating γ-H2AX⁺ progenitor cells in the stratum basale and associated γ-H2AX⁺ daughter cells (Figure 12. C). The number of γ-H2AX-positive daughter cells that originated from the same basal stem cell served as a reflection of DSB escaping DNA repair in the epidermis. The number of γ-H2AX⁺ progenies in the suprabasal layers was not significantly different between experimental groups, suggesting the efficiency of DSB repair was not significantly altered by HA-PE application in the epidermis. Although my findings do not support previous reports of the genoprotective function of HA, they are consistent with previous studies showing that

UVB-exposed eyelid keratinocytes sustain a high level of DNA damage but do not undergo neoplastic transformation^{79–83}. Deep next-generation sequencing shows a prevalent and high mutational load in oncogenic driver mutations of phenotypically-normal skin without detectable tumor development, suggesting that an innate barrier exist that restricts the carcinogenic potential of driver mutations^{79,83,86}.

Although the precise downstream mechanism remains unclear, apoptosis is a well-established mechanism of preventing carcinogenesis. Apoptosis is triggered when DNA damage accumulation overwhelms the repair machinery, or by blocking signaling of pathways that normal or tumor cells rely upon for proliferation, survival, and renewal. In UVB-exposed *Ptch*^{+/LacZ}/*Hr*^{-/-} mice, HA-PE restricts proliferation (as detected by decreased Ki67 expression, Figure 8) and promoted apoptosis cell subsets in the ORS and bulge of hair follicles, which were uniquely observed in HA-PE treated groups (Figure 15). In human and mouse, the ORS and bulge regions contain slow-cycling K15-expressing stem cells, which can migrate into the stratum basale to transiently participate in wound healing upon stimulated by sonic hedgehog signaling. In *Ptch*^{+/-} mice, K15⁺ cells and their progenies have the potential to give rise to BCC after chronic UVB exposure. Here, double-labelling immunofluorescence demonstrated these apoptotic subsets in the hair follicles were K15-positive (Figure 16). Intriguingly, apoptotic K15⁺ cells were not observed in the stratum basale following HA-PE treatment (Figure 16. A), possibly due to the lack of migration into the interfollicular epidermis (Supplemental Figure 2.B). HA-PE suppression of sonic hedgehog signal in the microenvironment may prevent K15⁺ stem cell migration into the IFE, since paracrine sonic hedgehog signal from the dermis and innervated neurons are required to initiate this process. Moreover, approximately 40% of total K15⁺ adult stem cells were apoptotic after 26 weeks of irradiation and HA-PE application. Consistent with this finding, the number of K15⁺ cells in UVB-irradiated HA-PE-treated mice was similar to controls at 4 weeks, but reduced significantly after 26 weeks of irradiation (Figure 16, C). This finding indicates that the adult stem cells were gradually lost due to cell death over 26 weeks. This apoptosis was associated with suppression of the pro-survival BCL2 expression in the epidermis and hair follicles (Figure 14). Evasion of apoptosis and sustained BCL2 expression are a hallmark of BCC carcinogenesis^{199,201,216}, all of which were absent in HA-PE treated group.

Previous studies report that the cell of origin in BCC pathogenesis depends on the component of sonic hedgehog signaling that is affected. For example, mutational inactivation of PTCH1 gives rise to BCCs originating from the K15⁺ BuSCs in the hair follicles. In contrast, constitutive activation of SMO or GLI2 produce BCCs arising from the K14⁺ adult stem cells in the interfollicular epidermis. Interestingly, BCCs arising from different epidermal compartments exhibit unique histopathological characteristics, which can be used to provide clues of the cell of origin when studying these keratinocyte tumors. Therefore, to investigate the epidermal compartment and the identity of cancer-initiating cells, I examined the histopathological characteristics of macroscopic BCC tumors as described previously^{58,62}. The BCC tumors in *Ptch*^{+/*LacZ*/*Hr*^{-/-} mice displayed irregularly shaped nests organized in a radiating, branching pattern resembling follicular differentiation (Figure 17.A), consistent with previous reports of micronodular BCC arising from hair follicles^{56,58,59}. Further, smooth muscle actin (SMA) expression in hair follicle cells is suggestive of inappropriate myoepithelial differentiation, a prominent feature in sporadic BCC patients and susceptible mice driven by sonic hedgehog activation under the K15 promoter⁵⁸. Interestingly, strong intracytoplasmic SMA reactivity was observed in BCC tumors (Figure 17.B) and the tumor-adjacent hair follicles (Figure 17. C), but was absent from the tumor-adjacent interfollicular epidermis, thus predicting a connection between BCCs in *Ptch*^{+/*LacZ*/*Hr*^{-/-} mice and hair follicles. Further, rare initial phases of neoplasm development demonstrated a direct association with the hair follicles (Figure 17.D). Strong K15 expression was detected in peripheral cells of developed tumor nests (Figure 17.E) and at early stages of atypical outgrowth from the bulge (Figure 17.C), thus predictive of BCCs arising from the hair follicles. This is supported by previous studies reporting prominent K15 immunoreactivity in human nodular BCCs, a subtype commonly associated with the bulge^{204,217}. Taken together, the findings here predict the macroscopic BCC tumors likely arise from the K15-expressing stem cells in hair follicles in *Ptch*^{+/*LacZ*/*Hr*^{-/-} mice.}}}

Since cancer-initiating cells rely on sonic hedgehog signaling to drive BCC tumorigenesis, the loss of the oncogenic driver triggers apoptosis in pre-malignant cells. Previous *in vivo* and cell culture studies show the depletion of sonic hedgehog by an inhibitor (cyclopamine) leads to adult stem cell quiescence and apoptosis^{46,47}. In this study, sonic hedgehog

signaling in the bulge and ORS was reduced by HA-PE application, which coincided with enhanced apoptosis in K15⁺ adult stem cells that rely on sonic hedgehog hyperactivation for tumorigenesis. Further, the data in this study demonstrated the activating ligand mRNA expression, SHH, was inhibited by HA-PE application (Figure 6.C), suggesting signaling inhibition occurs at the PTCH receptor level. In this context, CD44 is a promising candidate of signal transduction mediated by HA binding. CD44 is a well-established HA receptor that regulates downstream pathways, such as Wnt/beta-catenin^{218,219}, that modulate SHH transcription²²⁰⁻²²². Further, signaling downstream of CD44 is dependent on the identity of CD44 variant^{132,134,223}, thus adding an additional layer of complexity. Therefore, future experiments should be conducted to elucidate the mechanism underlying HMW-HA-mediated inhibition of sonic hedgehog activation and the role of CD44.

4.4 Future directions

Causation of HA-PE application and sonic hedgehog suppression should be established in future experiments. K15⁺ cells isolated from *Ptch*^{+/-} mice will be irradiated and treated with HA-PE. It is expected that HA-PE will reduce sonic hedgehog activation, restrict proliferation, and promote apoptosis. Since HA-PE reduced SHH transcription, an activating ligand that is not a hedgehog target gene, we speculate that pathway inhibition occurs at the Shh/PTCH1 level. Therefore, the addition of a downstream activator, such as an SMO agonist, is expected to override the effects of HA-PE in K15⁺ cells. Further, we speculate that this HA suppression of BCC initiation is orchestrated by CD44 in the hair follicles. To that end, CD44 standard- and variant-specific antibodies that interfere with HA-binding should be added to the *Ptch*^{+/-} K15⁺ cells as additional controls, and examined to assess whether HA-mediated suppression is conducted through CD44 binding. It is expected that interference with CD44/HA interaction will abolish the suppressive effect of HA-PE on sonic hedgehog signaling and proliferation. Since dysregulated proliferation, survival and inappropriate differentiation of damage-sustaining cells in hair follicles were detected in this study, mutational analyses should also be conducted on skin biopsies to examine alterations in additional driver pathways that regulate proliferation, stem cell survival and differentiation, such as WNT/ β -catenin and Notch signaling, in the skin. Moreover, mutational analyses will provide data on the identity of the somatic mutations

in UVB-exposed susceptible mice, thus allowing us to examine whether HA-PE modifies the microenvironment to select for mutations to prevent carcinogenesis. Lastly, RNAseq analyses should be performed to provide an unbiased assessment of transcriptome and pathway alterations induced by HA-PE application.

5 Conclusions

Taken together, the data presented here suggest a novel mechanism of HA-mediated resistance against tumor initiation in the context of BCC carcinogenesis. The accumulation of HMW-HA in epidermis did not exert its protective functions through shielding epidermal cells from DNA damage. Instead, HA-PE inhibited the tumorigenic potential of mutations via restricting proliferation and promoting apoptosis. Specifically, HA-PE prevents oncogenic sonic hedgehog signaling in the hair follicles, where the K15⁺ cancer-initiating cells reside in the *Ptch*^{+/*LacZ*}/*Hr*^{-/-} model. This chronic loss of oncogenic driver signaling limited the proliferative capacity of K15⁺ BuSCs, and resulted in a gradual depletion of cancer-initiating cells via apoptosis. However, this reduction in proliferation and enhanced apoptosis did not interfere with homeostasis as indicated by CD44v3 expression. HA-PE also contributed to establishing proper tissue architecture by maintaining a distinctive stratum basale separated from suprabasal layers. Overall, the findings here implicate HA-PE as a promising BCC prophylactic that can reduce BCC-associated healthcare costs and improve quality of life in patients. Moreover, aberrant hedgehog signaling is implicated in cancer stem cell maintenance^{224,225,226} that is required for tumor initiation in the breast, prostate and colon cancer^{38,227,228}. Therefore, a mechanistic understanding of HA-PE mediated resistance will have broad applications for developing preventative therapies. HA-PE may be re-purposed to reduce the tumorigenic potential of at-risk patients, and permit the development of preventative medicines against breast, prostate, and colon cancer^{38,226,227,228}.

References or Bibliography

1. Robertson, F. M.-L. & Fitzgerald, L. Skin cancer in the youth population of the United Kingdom. *J. Cancer Policy* **12**, 67–71 (2017).
2. Rogers, H. W., Weinstock, M. A., Feldman, S. R. & Coldiron, B. M. Incidence Estimate of Nonmelanoma Skin Cancer (Keratinocyte Carcinomas) in the U.S. Population, 2012. *JAMA Dermatol.* **151**, 1081–1086 (2015).
3. Leiter, U. *et al.* Incidence, Mortality, and Trends of Nonmelanoma Skin Cancer in Germany. *J. Invest. Dermatol.* **137**, 1860–1867 (2017).
4. Situm, M. *et al.* The role of UV radiation in the development of basal cell carcinoma. *Coll. Antropol.* **32 Suppl 2**, 167–170 (2008).
5. Abbas, M. & Kalia, S. Trends in Non-Melanoma Skin Cancer (Basal Cell Carcinoma and Squamous Cell Carcinoma) in Canada: A Descriptive Analysis of Available Data. *J. Cutan. Med. Surg.* **20**, 166–175 (2016).
6. Souza, C. F. D. *et al.* Topography of basal cell carcinoma and their correlations with gender, age and histologic pattern: a retrospective study of 1042 lesions. *An. Bras. Dermatol.* **86**, 272–277 (2011).
7. Wu, S., Han, J., Li, W.-Q., Li, T. & Qureshi, A. A. Basal-cell carcinoma incidence and associated risk factors in U.S. women and men. *Am. J. Epidemiol.* **178**, 890–897 (2013).
8. Leiter, U., Eigentler, T. & Garbe, C. Epidemiology of skin cancer. *Adv. Exp. Med. Biol.* **810**, 120–140 (2014).
9. Eisemann, N. *et al.* Non-melanoma skin cancer incidence and impact of skin cancer screening on incidence. *J. Invest. Dermatol.* **134**, 43–50 (2014).
10. Gloster, H. M. & Neal, K. Skin cancer in skin of color. *J. Am. Acad. Dermatol.* **55**, 741–760; quiz 761–764 (2006).
11. Kim, G. K., Del Rosso, J. Q. & Bellew, S. Skin cancer in asians: part 1: nonmelanoma skin cancer. *J. Clin. Aesthetic Dermatol.* **2**, 39–42 (2009).
12. Apalla, Z., Lallas, A., Sotiriou, E., Lazaridou, E. & Ioannides, D. Epidemiological trends in skin cancer. *Dermatol. Pract. Concept.* **7**, 1–6 (2017).
13. Madigan, L. M. & Lim, H. W. Tanning beds: Impact on health, and recent regulations. *Clin. Dermatol.* **34**, 640–648 (2016).
14. Christenson, L. J. *et al.* Incidence of basal cell and squamous cell carcinomas in a population younger than 40 years. *JAMA* **294**, 681–690 (2005).

15. Miller, S. J. *et al.* Basal Cell and Squamous Cell Skin Cancers. *J. Natl. Compr. Canc. Netw.* **8**, 836–864 (2010).
16. Nugent, Z., Demers, A. A., Wiseman, M. C., Mihalciou, C. & Kliever, E. V. Risk of second primary cancer and death following a diagnosis of nonmelanoma skin cancer. *Cancer Epidemiol. Biomark. Prev. Publ. Am. Assoc. Cancer Res. Cosponsored Am. Soc. Prev. Oncol.* **14**, 2584–2590 (2005).
17. Song, F. *et al.* Risk of a Second Primary Cancer after Non-melanoma Skin Cancer in White Men and Women: A Prospective Cohort Study. *PLoS Med.* **10**, (2013).
18. Chen, J. *et al.* Nonmelanoma Skin Cancer and Risk for Subsequent Malignancy. *JNCI J. Natl. Cancer Inst.* **100**, 1215–1222 (2008).
19. Epstein, E. H. Basal cell carcinomas: attack of the hedgehog. *Nat. Rev. Cancer* **8**, 743–754 (2008).
20. Aasi, S. *et al.* New Onset of Keratoacanthomas After Vismodegib Treatment for Locally Advanced Basal Cell Carcinomas: A Report of 2 Cases. *JAMA Dermatol. Chic. Ill* **149**, 242–243 (2013).
21. Mohan, S. V. *et al.* Increased Risk of Cutaneous Squamous Cell Carcinoma After Vismodegib Therapy for Basal Cell Carcinoma. *JAMA Dermatol.* **152**, 527–532 (2016).
22. Lara, F., Santamaría, J. R. & Garbers, L. E. F. de M. Recurrence rate of basal cell carcinoma with positive histopathological margins and related risk factors. *An. Bras. Dermatol.* **92**, 58–62 (2017).
23. Chren, M.-M. *et al.* Recurrence After Treatment of Nonmelanoma Skin Cancer. *Arch. Dermatol.* **147**, 540–546 (2011).
24. Koelblinger, P. & Lang, R. New developments in the treatment of basal cell carcinoma: update on current and emerging treatment options with a focus on vismodegib. *OncoTargets Ther.* **11**, 8327–8340 (2018).
25. Vuong, W., Lin, J. & Wei, R. L. Palliative radiotherapy for skin malignancies. *Ann. Palliat. Med.* **6**, 165–172 (2017).
26. McGregor, S., Minni, J. & Herold, D. Superficial Radiation Therapy for the Treatment of Nonmelanoma Skin Cancers. *J. Clin. Aesthetic Dermatol.* **8**, 12–14 (2015).
27. Rogers, H. W. & Coldiron, B. M. A relative value unit-based cost comparison of treatment modalities for nonmelanoma skin cancer: effect of the loss of the Mohs multiple surgery reduction exemption. *J. Am. Acad. Dermatol.* **61**, 96–103 (2009).

28. Montagna, E. & Lopes, O. S. Molecular basis of basal cell carcinoma. *An. Bras. Dermatol.* **92**, 517–520 (2017).
29. Epstein, E. H. Basal cell carcinomas: attack of the hedgehog. *Nat. Rev. Cancer* **8**, 743–754 (2008).
30. Bale, A. E. & Yu, K. The hedgehog pathway and basal cell carcinomas. *Hum. Mol. Genet.* **10**, 757–762 (2001).
31. Abe, Y. & Tanaka, N. Roles of the Hedgehog Signaling Pathway in Epidermal and Hair Follicle Development, Homeostasis, and Cancer. *J. Dev. Biol.* **5**, (2017).
32. Saran, A. Basal cell carcinoma and the carcinogenic role of aberrant Hedgehog signaling. *Future Oncol. Lond. Engl.* **6**, 1003–1014 (2010).
33. Villavicencio, E. H., Walterhouse, D. O. & Iannaccone, P. M. The Sonic Hedgehog–Patched–Gli Pathway in Human Development and Disease. *Am. J. Hum. Genet.* **67**, 1047–1054 (2000).
34. Caro, I. & Low, J. A. The Role of the Hedgehog Signaling Pathway in the Development of Basal Cell Carcinoma and Opportunities for Treatment. *Clin. Cancer Res.* **16**, 3335–3339 (2010).
35. Tukachinsky, H., Petrov, K., Watanabe, M. & Salic, A. Mechanism of inhibition of the tumor suppressor Patched by Sonic Hedgehog. *Proc. Natl. Acad. Sci. U. S. A.* **113**, E5866–E5875 (2016).
36. Zeng, H., Jia, J. & Liu, A. Coordinated Translocation of Mammalian Gli Proteins and Suppressor of Fused to the Primary Cilium. *PLoS ONE* **5**, (2010).
37. Huang, S. *et al.* Activation of the hedgehog pathway in human hepatocellular carcinomas. *Carcinogenesis* **27**, 1334–1340 (2006).
38. Altaba, A. R. i. Hedgehog Signaling and the Gli Code in Stem Cells, Cancer, and Metastases. *Sci Signal* **4**, pt9–pt9 (2011).
39. Xu, J. *et al.* Hair Follicle Disruption Facilitates Pathogenesis to UVB-Induced Cutaneous Inflammation and Basal Cell Carcinoma Development in Ptch+/- Mice. *Am. J. Pathol.* **184**, 1529–1540 (2014).
40. Gailani, M. R. *et al.* The role of the human homologue of Drosophila patched in sporadic basal cell carcinomas. *Nat. Genet.* **14**, 78–81 (1996).
41. Aszterbaum, M. *et al.* Identification of mutations in the human PATCHED gene in sporadic basal cell carcinomas and in patients with the basal cell nevus syndrome. *J. Invest. Dermatol.* **110**, 885–888 (1998).

42. Reifengerger, J. *et al.* Somatic mutations in the PTCH, SMOH, SUFUH and TP53 genes in sporadic basal cell carcinomas. *Br. J. Dermatol.* **152**, 43–51 (2005).
43. Kim, M.-Y., Park, H. J., Baek, S.-C., Byun, D. G. & Houh, D. Mutations of the p53 and PTCH gene in basal cell carcinomas: UV mutation signature and strand bias. *J. Dermatol. Sci.* **29**, 1–9 (2002).
44. Grachtchouk, M. *et al.* Basal cell carcinomas in mice arise from hair follicle stem cells and multiple epithelial progenitor populations. *J. Clin. Invest.* **121**, 1768–1781 (2011).
45. Cochrane, C. R., Szczepny, A., Watkins, D. N. & Cain, J. E. Hedgehog Signaling in the Maintenance of Cancer Stem Cells. *Cancers* **7**, 1554–1585 (2015).
46. Palma, V. *et al.* Sonic hedgehog controls stem cell behavior in the postnatal and adult brain. *Dev. Camb. Engl.* **132**, 335–344 (2005).
47. Araújo, G. L., Araújo, J. A., Schroeder, T., Tort, A. B. & Costa, M. R. Sonic hedgehog signaling regulates mode of cell division of early cerebral cortex progenitors and increases astroglialogenesis. *Front. Cell. Neurosci.* **8**, (2014).
48. Hsu, Y.-C., Li, L. & Fuchs, E. Transit-Amplifying Cells Orchestrate Stem Cell Activity and Tissue Regeneration. *Cell* **157**, 935–949 (2014).
49. Ambler, C. A. & Määttä, A. Epidermal stem cells: location, potential and contribution to cancer. *J. Pathol.* **217**, 206–216 (2009).
50. Boehnke, K., Falkowska-Hansen, B., Stark, H.-J. & Boukamp, P. Stem cells of the human epidermis and their niche: composition and function in epidermal regeneration and carcinogenesis. *Carcinogenesis* **33**, 1247–1258 (2012).
51. Plikus, M. V. *et al.* Epithelial Stem Cells and Implications for Wound Repair. *Semin. Cell Dev. Biol.* **23**, 946–953 (2012).
52. Hsu, Y.-C., Pasolli, H. A. & Fuchs, E. Dynamics between Stem Cells, Niche, and Progeny in the Hair Follicle. *Cell* **144**, 92–105 (2011).
53. Oro, A. E. & Higgins, K. Hair cycle regulation of Hedgehog signal reception. *Dev. Biol.* **255**, 238–248 (2003).
54. Brownell, I., Guevara, E., Bai, C. B., Loomis, C. A. & Joyner, A. L. Nerve-Derived Sonic Hedgehog Defines a Niche for Hair Follicle Stem Cells Capable of Becoming Epidermal Stem Cells. *Cell Stem Cell* **8**, 552–565 (2011).
55. St-Jacques, B. *et al.* Sonic hedgehog signaling is essential for hair development. *Curr. Biol.* **8**, 1058–1069 (1998).

56. Wang, L. C. *et al.* Regular articles: conditional disruption of hedgehog signaling pathway defines its critical role in hair development and regeneration. *J. Invest. Dermatol.* **114**, 901–908 (2000).
57. Dessinioti, C., Antoniou, C. & Stratigos, A. J. From basal cell carcinoma morphogenesis to the alopecia induced by hedgehog inhibitors: connecting the dots. *Br. J. Dermatol.* **177**, 1485–1494 (2017).
58. Wang, G. Y., Wang, J., Mancianti, M.-L. & Epstein, E. H. Basal cell carcinomas arise from hair follicle stem cells in Ptch1(+/-) mice. *Cancer Cell* **19**, 114–124 (2011).
59. Youssef, K. K. *et al.* Identification of the cell lineage at the origin of basal cell carcinoma. *Nat. Cell Biol.* **12**, 299–305 (2010).
60. Seykora, J. T. & Cotsarelis, G. Keratin 15-Positive Stem Cells Give Rise to Basal Cell Carcinomas in Irradiated Ptch1+/- Mice. *Cancer Cell* **19**, 5–6 (2011).
61. Jaks, V. *et al.* Lgr5 marks cycling, yet long-lived, hair follicle stem cells. *Nat. Genet.* **40**, 1291–1299 (2008).
62. Mancuso, M. *et al.* Hair cycle-dependent basal cell carcinoma tumorigenesis in Ptc1neo67/+ mice exposed to radiation. *Cancer Res.* **66**, 6606–6614 (2006).
63. Raasch, B. A., Buettner, P. G. & Garbe, C. Basal cell carcinoma: histological classification and body-site distribution. *Br. J. Dermatol.* **155**, 401–407 (2006).
64. Mackiewicz-Wysocka, M., Bowszyc-Dmochowska, M., Strzelecka-Węklar, D., Dańczak-Pazdrowska, A. & Adamski, Z. Basal cell carcinoma – diagnosis. *Contemp. Oncol.* **17**, 337–342 (2013).
65. Kadono, T., Okada, H., Okuno, T. & Ohara, K. Basal cell carcinoma with neuroid type nuclear palisading: a report of three cases. *Br. J. Dermatol.* **138**, 1064–1066 (1998).
66. Pellegrini, C. *et al.* Understanding the Molecular Genetics of Basal Cell Carcinoma. *Int. J. Mol. Sci.* **18**, (2017).
67. D’Orazio, J., Jarrett, S., Amaro-Ortiz, A. & Scott, T. UV Radiation and the Skin. *Int. J. Mol. Sci.* **14**, 12222–12248 (2013).
68. Pfeifer, G. P. & Besaratinia, A. UV wavelength-dependent DNA damage and human non-melanoma and melanoma skin cancer. *Photochem. Photobiol. Sci. Off. J. Eur. Photochem. Assoc. Eur. Soc. Photobiol.* **11**, 90–97 (2012).
69. Kim, I. & He, Y.-Y. Ultraviolet radiation-induced non-melanoma skin cancer: Regulation of DNA damage repair and inflammation. *Genes Dis.* **1**, 188–198 (2014).

70. Courdavault, S. *et al.* Repair of the three main types of bipyrimidine DNA photoproducts in human keratinocytes exposed to UVB and UVA radiations. *DNA Repair* **4**, 836–844 (2005).
71. Anna, B. *et al.* Mechanism of UV-related carcinogenesis and its contribution to nevi/melanoma. *Expert Rev. Dermatol.* **2**, 451–469 (2007).
72. Situm, M. *et al.* The role of UV radiation in the development of basal cell carcinoma. *Coll. Antropol.* **32 Suppl 2**, 167–170 (2008).
73. Wu, C.-S. *et al.* Differential regulation of nuclear factor-kappa B subunits on epidermal keratinocytes by ultraviolet B and tacrolimus. *Kaohsiung J. Med. Sci.* **28**, 577–585 (2012).
74. Kripke, M. L. Effects of UV radiation on the immune system: consequences for UV carcinogenesis. *Adv. Exp. Med. Biol.* **121**, 589–598 (1979).
75. Kim, C. & Pasparakis, M. Epidermal p65/NF- κ B signalling is essential for skin carcinogenesis. *EMBO Mol. Med.* **6**, 970–983 (2014).
76. Narendhirakannan, R. T. & Hannah, M. A. C. Oxidative Stress and Skin Cancer: An Overview. *Indian J. Clin. Biochem.* **28**, 110–115 (2013).
77. Chalmers, Z. R. *et al.* Analysis of 100,000 human cancer genomes reveals the landscape of tumor mutational burden. *Genome Med.* **9**, 34 (2017).
78. Goodman, A. M. *et al.* Genomic landscape of advanced basal cell carcinoma: Implications for precision treatment with targeted and immune therapies. *Oncoimmunology* **7**, (2017).
79. Martincorena, I. *et al.* Tumor evolution. High burden and pervasive positive selection of somatic mutations in normal human skin. *Science* **348**, 880–886 (2015).
80. Kuhner, M. K., Kostadinov, R. & Reid, B. J. Limitations of the Driver/Passenger Model in Cancer Prevention. *Cancer Prev. Res. Phila. Pa* **9**, 335–338 (2016).
81. Risques, R. A. & Kennedy, S. R. Aging and the rise of somatic cancer-associated mutations in normal tissues. *PLOS Genet.* **14**, e1007108 (2018).
82. Adjiri, A. DNA Mutations May Not Be the Cause of Cancer. *Oncol. Ther.* **5**, 85–101 (2017).
83. Anglesio, M. S. *et al.* Cancer-Associated Mutations in Endometriosis without Cancer. *N. Engl. J. Med.* **376**, 1835–1848 (2017).
84. Zhang, W., Remenyik, E., Zelterman, D., Brash, D. E. & Wikonkal, N. M. Escaping the stem cell compartment: Sustained UVB exposure allows p53-mutant

- keratinocytes to colonize adjacent epidermal proliferating units without incurring additional mutations. *Proc. Natl. Acad. Sci. U. S. A.* **98**, 13948–13953 (2001).
85. Velic, D. *et al.* DNA Damage Signalling and Repair Inhibitors: The Long-Sought-After Achilles' Heel of Cancer. *Biomolecules* **5**, 3204–3259 (2015).
 86. Wang, F. *et al.* Phenotypic reversion or death of cancer cells by altering signaling pathways in three-dimensional contexts. *J. Natl. Cancer Inst.* **94**, 1494–1503 (2002).
 87. Bhat, R. & Bissell, M. J. Of plasticity and specificity: dialectics of the micro- and macro-environment and the organ phenotype. *Wiley Interdiscip. Rev. Membr. Transp. Signal.* **3**, 147–163 (2014).
 88. van der Pols, J. C., Williams, G. M., Pandeya, N., Logan, V. & Green, A. C. Prolonged prevention of squamous cell carcinoma of the skin by regular sunscreen use. *Cancer Epidemiol. Biomark. Prev. Publ. Am. Assoc. Cancer Res. Cosponsored Am. Soc. Prev. Oncol.* **15**, 2546–2548 (2006).
 89. Zak-Prelich, M., Narbutt, J. & Sysa-Jedrzejowska, A. Environmental risk factors predisposing to the development of basal cell carcinoma. *Dermatol. Surg. Off. Publ. Am. Soc. Dermatol. Surg. Al* **30**, 248–252 (2004).
 90. Chesnut, C. & Kim, J. Is There Truly No Benefit with Sunscreen Use and Basal Cell Carcinoma? A Critical Review of the Literature and the Application of New Sunscreen Labeling Rules to Real-World Sunscreen Practices. *Journal of Skin Cancer* (2012). doi:10.1155/2012/480985
 91. Lewis, K. N., Rubinstein, N. D. & Buffenstein, R. A window into extreme longevity; the circulating metabolomic signature of the naked mole-rat, a mammal that shows negligible senescence. *GeroScience* **40**, 105–121 (2018).
 92. Taylor, K. R., Milone, N. A. & Rodriguez, C. E. Four Cases of Spontaneous Neoplasia in the Naked Mole-Rat (*Heterocephalus glaber*), A Putative Cancer-Resistant Species. *J. Gerontol. A. Biol. Sci. Med. Sci.* **72**, 38–43 (2017).
 93. Seluanov, A. *et al.* Hypersensitivity to contact inhibition provides a clue to cancer resistance of naked mole-rat. *Proc. Natl. Acad. Sci. U. S. A.* **106**, 19352–19357 (2009).
 94. Tian, X. *et al.* High molecular weight hyaluronan mediates the cancer resistance of the naked mole-rat. *Nature* **499**, 346–349 (2013).
 95. Zhao, Y. *et al.* Bioengineered tumor microenvironments with naked mole rats high-molecular-weight hyaluronan induces apoptosis in breast cancer cells. *Oncogene* **1** (2019). doi:10.1038/s41388-019-0719-4
 96. Barcellos-Hoff, M. H. It takes a tissue to make a tumor: epigenetics, cancer and the microenvironment. *J. Mammary Gland Biol. Neoplasia* **6**, 213–221 (2001).

97. Weaver, V. M. & Gilbert, P. Watch thy neighbor: cancer is a communal affair. *J. Cell Sci.* **117**, 1287–1290 (2004).
98. Cyphert, J. M., Trempus, C. S. & Garantziotis, S. Size Matters: Molecular Weight Specificity of Hyaluronan Effects in Cell Biology. *International Journal of Cell Biology* (2015). doi:10.1155/2015/563818
99. Schwertfeger, K. L., Cowman, M. K., Telmer, P. G., Turley, E. A. & McCarthy, J. B. Hyaluronan, Inflammation, and Breast Cancer Progression. *Front. Immunol.* **6**, 236 (2015).
100. Monslow, J., Govindaraju, P. & Puré, E. Hyaluronan - a functional and structural sweet spot in the tissue microenvironment. *Front. Immunol.* **6**, 231 (2015).
101. Stern, R. & Maibach, H. I. Hyaluronan in skin: aspects of aging and its pharmacologic modulation. *Clin. Dermatol.* **26**, 106–122 (2008).
102. Tian, X. *et al.* High-molecular-mass hyaluronan mediates the cancer resistance of the naked mole rat. *Nature* **499**, 346–349 (2013).
103. Csoka, A. B., Frost, G. I. & Stern, R. The six hyaluronidase-like genes in the human and mouse genomes. *Matrix Biol. J. Int. Soc. Matrix Biol.* **20**, 499–508 (2001).
104. NOBLE, P. W., LIANG, J. & JIANG, D. Hyaluronan as an Immune Regulator in Human Diseases. *Physiol. Rev.* **91**, 221–264 (2011).
105. Cyphert, J. M., Trempus, C. S. & Garantziotis, S. Size Matters: Molecular Weight Specificity of Hyaluronan Effects in Cell Biology. *Int. J. Cell Biol.* **2015**, 563818 (2015).
106. Papakonstantinou, E., Roth, M. & Karakiulakis, G. Hyaluronic acid: A key molecule in skin aging. *Dermatoendocrinol.* **4**, 253–258 (2012).
107. Robert, L., Robert, A.-M. & Renard, G. Biological effects of hyaluronan in connective tissues, eye, skin, venous wall. Role in aging. *Pathol. Biol. (Paris)* **58**, 187–198 (2010).
108. Reed, R. K., Lilja, K. & Laurent, T. C. Hyaluronan in the rat with special reference to the skin. *Acta Physiol. Scand.* **134**, 405–411 (1988).
109. Weigel, P. H. Hyaluronan Synthase: The Mechanism of Initiation at the Reducing End and a Pendulum Model for Polysaccharide Translocation to the Cell Exterior. *Int. J. Cell Biol.* **2015**, (2015).
110. Törrönen, K. *et al.* Tissue distribution and subcellular localization of hyaluronan synthase isoenzymes. *Histochem. Cell Biol.* **141**, 17–31 (2014).

111. Itano, N. *et al.* Three isoforms of mammalian hyaluronan synthases have distinct enzymatic properties. *J. Biol. Chem.* **274**, 25085–25092 (1999).
112. Lepperdinger, G., Müllegger, J. & Kreil, G. Hyal2 — less active, but more versatile? *Matrix Biol.* **20**, 509–514 (2001).
113. Noble, P. W. Hyaluronan and its catabolic products in tissue injury and repair. *Matrix Biol.* **21**, 25–29 (2002).
114. Wu, W. *et al.* The Protective Role of Hyaluronic Acid in Cr(VI)-Induced Oxidative Damage in Corneal Epithelial Cells. *Journal of Ophthalmology* (2017). doi:10.1155/2017/3678586
115. Pauloin, T., Dutot, M., Warnet, J.-M. & Rat, P. In vitro modulation of preservative toxicity: high molecular weight hyaluronan decreases apoptosis and oxidative stress induced by benzalkonium chloride. *Eur. J. Pharm. Sci. Off. J. Eur. Fed. Pharm. Sci.* **34**, 263–273 (2008).
116. Chen, W. Y. & Abatangelo, G. Functions of hyaluronan in wound repair. *Wound Repair Regen. Off. Publ. Wound Heal. Soc. Eur. Tissue Repair Soc.* **7**, 79–89 (1999).
117. Scheibner, K. A. *et al.* Hyaluronan fragments act as an endogenous danger signal by engaging TLR2. *J. Immunol. Baltim. Md 1950* **177**, 1272–1281 (2006).
118. Dai, G. *et al.* Chronic Ultraviolet B Irradiation Causes Loss of Hyaluronic Acid from Mouse Dermis Because of Down-Regulation of Hyaluronic Acid Synthases. *Am. J. Pathol.* **171**, 1451–1461 (2007).
119. Tobiishi, M. *et al.* Changes in epidermal hyaluronan metabolism following UVB irradiation. *J. Dermatol. Sci.* **64**, 31–38 (2011).
120. Ultraviolet-B Irradiation Induces Differential Regulations of Hyaluronidase Expression and Activity in Normal Human Keratinocytes | Request PDF. *ResearchGate* Available at: https://www.researchgate.net/publication/51244397_Ultraviolet-B_Irradiation_Induces_Differential_Regulations_of_Hyaluronidase_Expression_and_Activity_in_Normal_Human_Keratinocytes. (Accessed: 7th March 2019)
121. Price, Z. K., Lokman, N. A. & Ricciardelli, C. Differing Roles of Hyaluronan Molecular Weight on Cancer Cell Behavior and Chemotherapy Resistance. *Cancers* **10**, (2018).
122. Iijima, J., Konno, K. & Itano, N. Inflammatory Alterations of the Extracellular Matrix in the Tumor Microenvironment. *Cancers* **3**, 3189–3205 (2011).
123. Bourguignon, L. Y. W., Wong, G., Earle, C. A. & Xia, W. Interaction of Low Molecular Weight Hyaluronan (LMW-HA) with CD44 and Toll-Like Receptors

- Promotes the Actin Filament-Associated Protein (AFAP-110)-Actin Binding and MyD88-NFκB Signaling Leading to Pro-inflammatory Cytokine/Chemokine Production and Breast Tumor Invasion. *Cytoskelet. Hoboken Nj* **68**, 671–693 (2011).
124. Du, Y. *et al.* Low-molecular-weight hyaluronan (LMW-HA) accelerates lymph node metastasis of melanoma cells by inducing disruption of lymphatic intercellular adhesion. *Oncoimmunology* **5**, (2016).
 125. Yu, M. *et al.* Hyaluroan-regulated lymphatic permeability through S1P receptors is crucial for cancer metastasis. *Med. Oncol. Northwood Lond. Engl.* **32**, 381 (2015).
 126. Misra, S., Hascall, V. C., Markwald, R. R. & Ghatak, S. Interactions between Hyaluronan and Its Receptors (CD44, RHAMM) Regulate the Activities of Inflammation and Cancer. *Front. Immunol.* **6**, (2015).
 127. Yang, C. *et al.* The High and Low Molecular Weight Forms of Hyaluronan Have Distinct Effects on CD44 Clustering. *J. Biol. Chem.* **287**, 43094–43107 (2012).
 128. Yamada, Y. *et al.* Elevated transcript level of hyaluronan synthase1 gene correlates with poor prognosis of human colon cancer. *Clin. Exp. Metastasis* **21**, 57–63 (2004).
 129. Bourguignon, L. Y. W., Gilad, E. & Peyrollier, K. Heregulin-mediated ErbB2-ERK Signaling Activates Hyaluronan Synthases Leading to CD44-dependent Ovarian Tumor Cell Growth and Migration. *J. Biol. Chem.* **282**, 19426–19441 (2007).
 130. Bertrand, P. *et al.* Increased hyaluronidase levels in breast tumor metastases. *Int. J. Cancer* **73**, 327–331 (1997).
 131. Viola, M. *et al.* Biology and biotechnology of hyaluronan. *Glycoconj. J.* **32**, 93–103 (2015).
 132. Tölg, C., Hofmann, M., Herrlich, P. & Ponta, H. Splicing choice from ten variant exons establishes CD44 variability. *Nucleic Acids Res.* **21**, 1225–1229 (1993).
 133. Tuhkanen, A.-L., Ågren, U. M., Tammi, M. I. & Tammi, R. H. CD44 Expression Marks the Onset of Keratinocyte Stratification and Mesenchymal Maturation into Fibrous Dermis in Fetal Human Skin. *J. Histochem. Cytochem.* **47**, 1617–1624 (1999).
 134. Bennett, K. L. *et al.* CD44 isoforms containing exon V3 are responsible for the presentation of heparin-binding growth factor. *J. Cell Biol.* **128**, 687–698 (1995).
 135. Teye, K. *et al.* Isolation of All CD44 Transcripts in Human Epidermis and Regulation of Their Expression by Various Agents. *PLOS ONE* **11**, e0160952 (2016).

136. Misra, S., Hascall, V. C., Markwald, R. R. & Ghatak, S. Interactions between Hyaluronan and Its Receptors (CD44, RHAMM) Regulate the Activities of Inflammation and Cancer. *Front. Immunol.* **6**, 201 (2015).
137. Yang, C. *et al.* The high and low molecular weight forms of hyaluronan have distinct effects on CD44 clustering. *J. Biol. Chem.* **287**, 43094–43107 (2012).
138. Kothapalli, D., Flowers, J., Xu, T., Puré, E. & Assoian, R. K. Differential activation of ERK and Rac mediates the proliferative and anti-proliferative effects of hyaluronan and CD44. *J. Biol. Chem.* **283**, 31823–31829 (2008).
139. Bourguignon, L. Y. W., Wong, G., Earle, C. A. & Xia, W. Interaction of Low Molecular Weight Hyaluronan (LMW-HA) with CD44 and Toll-Like Receptors Promotes the Actin Filament-Associated Protein (AFAP-110)-Actin Binding and MyD88-NFκB Signaling Leading to Pro-inflammatory Cytokine/Chemokine Production and Breast Tumor Invasion. *Cytoskelet. Hoboken Nj* **68**, 671–693 (2011).
140. Pauloin, T., Dutot, M., Joly, F., Warnet, J.-M. & Rat, P. High molecular weight hyaluronan decreases UVB-induced apoptosis and inflammation in human epithelial corneal cells. *Mol. Vis.* **15**, 577–583 (2009).
141. Noble, P. W., McKee, C. M., Cowman, M. & Shin, H. S. Hyaluronan fragments activate an NF-kappa B/I-kappa B alpha autoregulatory loop in murine macrophages. *J. Exp. Med.* **183**, 2373–2378 (1996).
142. McKee, C. M. *et al.* Hyaluronan fragments induce nitric-oxide synthase in murine macrophages through a nuclear factor kappaB-dependent mechanism. *J. Biol. Chem.* **272**, 8013–8018 (1997).
143. Alaniz, L. *et al.* Modulation of matrix metalloproteinase-9 activity by hyaluronan is dependent on NF-kappaB activity in lymphoma cell lines with dissimilar invasive behavior. *Biochem. Biophys. Res. Commun.* **324**, 736–743 (2004).
144. Ohno, S., Im, H.-J., Knudson, C. B. & Knudson, W. Hyaluronan oligosaccharides induce matrix metalloproteinase 13 via transcriptional activation of NFkappaB and p38 MAP kinase in articular chondrocytes. *J. Biol. Chem.* **281**, 17952–17960 (2006).
145. Chen, Y.-T., Chen, Z. & Du, Y.-C. N. Immunohistochemical analysis of RHAMM expression in normal and neoplastic human tissues: a cell cycle protein with distinctive expression in mitotic cells and testicular germ cells. *Oncotarget* **9**, 20941–20952 (2018).
146. Tolg, C., McCarthy, J. B., Yazdani, A. & Turley, E. A. Hyaluronan and RHAMM in Wound Repair and the “Cancerization” of Stromal Tissues. *BioMed Res. Int.* **2014**, (2014).

147. Hall, C. L. & Turley, E. A. Hyaluronan: RHAMM mediated cell locomotion and signaling in tumorigenesis. *J. Neurooncol.* **26**, 221–229 (1995).
148. Kouvidi, K., Nikitovic, D., Berdiaki, A. & Tzanakakis, G. N. Hyaluronan/RHAMM interactions in mesenchymal tumor pathogenesis: role of growth factors. *Adv. Cancer Res.* **123**, 319–349 (2014).
149. Hall, C. L. *et al.* Overexpression of the hyaluronan receptor RHAMM is transforming and is also required for H-ras transformation. *Cell* **82**, 19–28 (1995).
150. Chen, H. *et al.* Spatial regulation of Aurora A activity during mitotic spindle assembly requires RHAMM to correctly localize TPX2. *Cell Cycle Georget. Tex* **13**, 2248–2261 (2014).
151. Tzellos, T. G. *et al.* Nodular basal cell carcinoma is associated with increased hyaluronan homeostasis. *J. Eur. Acad. Dermatol. Venereol. JEADV* **25**, 679–687 (2011).
152. Turley, E. A., Wood, D. K. & McCarthy, J. B. Carcinoma Cell Hyaluronan as a ‘Portable’ Cancerized Prometastatic Microenvironment. *Cancer Res.* **76**, 2507–2512 (2016).
153. Wang, Z. *et al.* Interplay of mevalonate and Hippo pathways regulates RHAMM transcription via YAP to modulate breast cancer cell motility. *Proc. Natl. Acad. Sci. U. S. A.* **111**, E89-98 (2014).
154. Hamilton, S. R. *et al.* The hyaluronan receptors CD44 and Rhamm (CD168) form complexes with ERK1,2 that sustain high basal motility in breast cancer cells. *J. Biol. Chem.* **282**, 16667–16680 (2007).
155. Tolg, C. *et al.* Rhamm^{-/-} fibroblasts are defective in CD44-mediated ERK1,2 mitogenic signaling, leading to defective skin wound repair. *J. Cell Biol.* **175**, 1017–1028 (2006).
156. Wu, M. *et al.* A novel role of low molecular weight hyaluronan in breast cancer metastasis. *FASEB J.* **29**, 1290–1298 (2014).
157. Berdiaki, A. *et al.* bFGF induces changes in hyaluronan synthase and hyaluronidase isoform expression and modulates the migration capacity of fibrosarcoma cells. *Biochim. Biophys. Acta* **1790**, 1258–1265 (2009).
158. Posey, J. T. *et al.* Evaluation of the prognostic potential of hyaluronic acid and hyaluronidase (HYAL1) for prostate cancer. *Cancer Res.* **63**, 2638–2644 (2003).
159. Tan, J.-X. *et al.* HYAL1 overexpression is correlated with the malignant behavior of human breast cancer. *Int. J. Cancer* **128**, 1303–1315 (2011).

160. Lokeshwar, V. B., Cerwinka, W. H., Isoyama, T. & Lokeshwar, B. L. HYAL1 hyaluronidase in prostate cancer: a tumor promoter and suppressor. *Cancer Res.* **65**, 7782–7789 (2005).
161. Ekici, S. *et al.* Comparison of the prognostic potential of hyaluronic acid, hyaluronidase (HYAL-1), CD44v6 and microvessel density for prostate cancer. *Int. J. Cancer* **112**, 121–129 (2004).
162. Gomez, C. S. *et al.* Hyaluronic acid and HYAL-1 in prostate biopsy specimens: predictors of biochemical recurrence. *J. Urol.* **182**, 1350–1356 (2009).
163. Udabage, L., Brownlee, G. R., Nilsson, S. K. & Brown, T. J. The over-expression of HAS2, Hyal-2 and CD44 is implicated in the invasiveness of breast cancer. *Exp. Cell Res.* **310**, 205–217 (2005).
164. Siiskonen, H., Poukka, M., Tynnelä-Korhonen, K., Sironen, R. & Pasonen-Seppänen, S. Inverse expression of hyaluronidase 2 and hyaluronan synthases 1-3 is associated with reduced hyaluronan content in malignant cutaneous melanoma. *BMC Cancer* **13**, 181 (2013).
165. Kovar, J. L., Johnson, M. A., Volcheck, W. M., Chen, J. & Simpson, M. A. Hyaluronidase expression induces prostate tumor metastasis in an orthotopic mouse model. *Am. J. Pathol.* **169**, 1415–1426 (2006).
166. Patel, S. *et al.* Hyaluronidase gene profiling and role of hyal-1 overexpression in an orthotopic model of prostate cancer. *Int. J. Cancer* **97**, 416–424 (2002).
167. Bharadwaj, A. G. *et al.* Spontaneous metastasis of prostate cancer is promoted by excess hyaluronan synthesis and processing. *Am. J. Pathol.* **174**, 1027–1036 (2009).
168. Tiainen, S. *et al.* High numbers of macrophages, especially M2-like (CD163-positive), correlate with hyaluronan accumulation and poor outcome in breast cancer. *Histopathology* **66**, 873–883 (2015).
169. Enegd, B. *et al.* Overexpression of hyaluronan synthase-2 reduces the tumorigenic potential of glioma cells lacking hyaluronidase activity. *Neurosurgery* **50**, 1311–1318 (2002).
170. Mueller, B. M. *et al.* Hyaluronan Inhibits Postchemotherapy Tumor Regrowth in a Colon Carcinoma Xenograft Model. *Mol. Cancer Ther.* **9**, 3024–3032 (2010).
171. Ye, J. *et al.* High molecular weight hyaluronan decreases oxidative DNA damage induced by EDTA in human corneal epithelial cells. *Eye* **26**, 1012–1020 (2012).
172. ZHAO, H. *et al.* Protective effect of hyaluronate on oxidative DNA damage in WI-38 and A549 cells. *Int. J. Oncol.* **32**, 1159–1167 (2008).

173. Solis, M. A. *et al.* Hyaluronan Regulates Cell Behavior: A Potential Niche Matrix for Stem Cells. *Biochemistry Research International* (2012). doi:10.1155/2012/346972
174. Nakashima, H. *et al.* Nuclear factor-kappaB contributes to hedgehog signaling pathway activation through sonic hedgehog induction in pancreatic cancer. *Cancer Res.* **66**, 7041–7049 (2006).
175. Kasperczyk, H., Baumann, B., Debatin, K.-M. & Fulda, S. Characterization of sonic hedgehog as a novel NF-kappaB target gene that promotes NF-kappaB-mediated apoptosis resistance and tumor growth in vivo. *FASEB J. Off. Publ. Fed. Am. Soc. Exp. Biol.* **23**, 21–33 (2009).
176. Chen, X. *et al.* Hyaluronan arrests human breast cancer cell growth by prolonging the G0/G1 phase of the cell cycle. *Acta Biochim. Biophys. Sin.* **50**, 1181–1189 (2018).
177. Albano, G. D. *et al.* Effect of High, Medium, and Low Molecular Weight Hyaluronan on Inflammation and Oxidative Stress in an In Vitro Model of Human Nasal Epithelial Cells. *Mediators of Inflammation* (2016). doi:10.1155/2016/8727289
178. Bourguignon, L. Y. W. *et al.* Selective matrix (hyaluronan) interaction with CD44 and RhoGTPase signaling promotes keratinocyte functions and overcomes age-related epidermal dysfunction. *J. Dermatol. Sci.* **72**, 32–44 (2013).
179. Morganti, P. *et al.* A phosphatidylcholine hyaluronic acid chitin–nanofibrils complex for a fast skin remodeling and a rejuvenating look. *Clinical, Cosmetic and Investigational Dermatology* (2012). doi:10.2147/CCID.S29664
180. Pavicic, T. *et al.* Efficacy of cream-based novel formulations of hyaluronic acid of different molecular weights in anti-wrinkle treatment. *J. Drugs Dermatol. JDD* **10**, 990–1000 (2011).
181. Brown, M. B. & Jones, S. A. Hyaluronic acid: a unique topical vehicle for the localized delivery of drugs to the skin. *J. Eur. Acad. Dermatol. Venereol.* **19**, 308–318 (2005).
182. Brown, T. J., Alcorn, D. & Fraser, J. R. E. Absorption of Hyaluronan Applied to the Surface of Intact Skin. *J. Invest. Dermatol.* **113**, 740–746 (1999).
183. Symonette, C. J. *et al.* Hyaluronan-Phosphatidylethanolamine Polymers Form Pericellular Coats on Keratinocytes and Promote Basal Keratinocyte Proliferation. *BioMed Research International* (2014). doi:10.1155/2014/727459
184. Xu, J. *et al.* Hair follicle disruption facilitates pathogenesis to UVB-induced cutaneous inflammation and basal cell carcinoma development in Ptch(+/-) mice. *Am. J. Pathol.* **184**, 1529–1540 (2014).

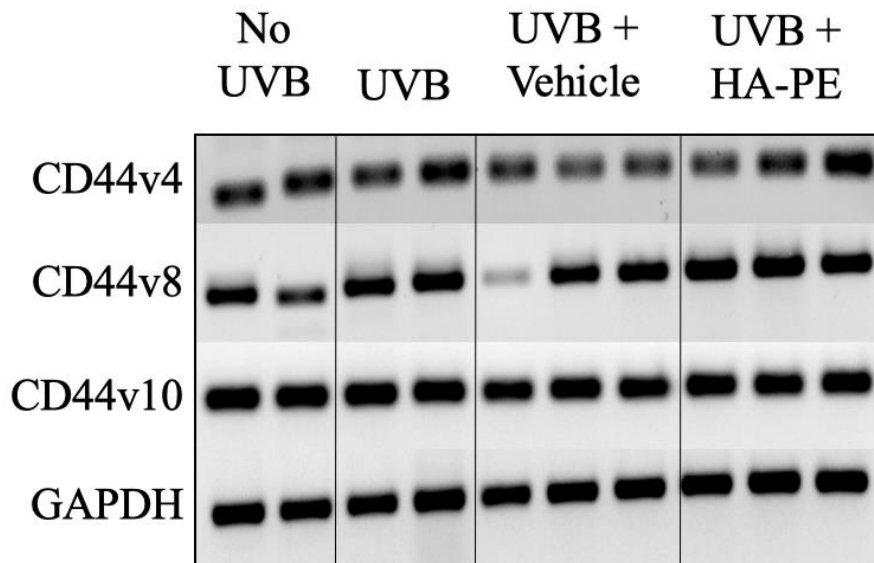
185. Kim, H. *et al.* Loss of Hairless Confers Susceptibility to UVB-Induced Tumorigenesis via Disruption of NF-kappaB Signaling. *PLOS ONE* **7**, e39691 (2012).
186. Xu, J. *et al.* Hair follicle disruption facilitates pathogenesis to UVB-induced cutaneous inflammation and basal cell carcinoma development in Ptch(+/-) mice. *Am. J. Pathol.* **184**, 1529–1540 (2014).
187. Kim, B.-K. *et al.* Hairless Plays a Role in Formation of Inner Root Sheath via Regulation of Dlx3 Gene. *J. Biol. Chem.* **287**, 16681–16688 (2012).
188. Panteleyev, A. A., Paus, R. & Christiano, A. M. Patterns of Hairless (hr) Gene Expression in Mouse Hair Follicle Morphogenesis and Cycling. *Am. J. Pathol.* **157**, 1071–1079 (2000).
189. Kim, J. K., Kim, B. K., Park, J. K., Choi, J. H. & Kim Yoon, S. The Hairless Gene: A Putative Navigator of Hair Follicle Development. *Genomics Inform.* **9**, 93–101
190. Benavides, F., Oberyszyn, T. M., VanBuskirk, A. M., Reeve, V. E. & Kusewitt, D. F. The hairless mouse in skin research. *J. Dermatol. Sci.* **53**, 10–18 (2009).
191. Panteleyev, A. A., Botchkareva, N. V., Sundberg, J. P., Christiano, A. M. & Paus, R. The Role of the Hairless (hr) Gene in the Regulation of Hair Follicle Catagen Transformation. *Am. J. Pathol.* **155**, 159–171 (1999).
192. Cousteils, K. Role of High Molecular Weight Hyaluronan in Ultraviolet B Light-Induced Transformation. *Electron. Thesis Diss. Repos.* (2017).
193. Symonette, C. J. *et al.* Hyaluronan-Phosphatidylethanolamine Polymers Form Pericellular Coats on Keratinocytes and Promote Basal Keratinocyte Proliferation. *BioMed Res. Int.* **2014**, (2014).
194. Bankhead, P. *et al.* QuPath: Open source software for digital pathology image analysis. *Sci. Rep.* **7**, 16878 (2017).
195. Tan, J.-X. *et al.* Upregulation of HYAL1 Expression in Breast Cancer Promoted Tumor Cell Proliferation, Migration, Invasion and Angiogenesis. *PLOS ONE* **6**, e22836 (2011).
196. Lokeshwar, V. B., Lokeshwar, B. L., Pham, H. T. & Block, N. L. Association of elevated levels of hyaluronidase, a matrix-degrading enzyme, with prostate cancer progression. *Cancer Res.* **56**, 651–657 (1996).
197. Bhilocha, S. *et al.* Agarose and Polyacrylamide Gel Electrophoresis Methods for Molecular Mass Analysis of 5–500 kDa Hyaluronan. *Anal. Biochem.* **417**, 41–49 (2011).

198. Li, Y., Li, L., Brown, T. J. & Heldin, P. Silencing of hyaluronan synthase 2 suppresses the malignant phenotype of invasive breast cancer cells. *Int. J. Cancer* **120**, 2557–2567 (2007).
199. N. Sivrikoz, O. & Kandiloğlu, G. The Effects of Cyclin D1 and Bcl-2 Expression on Aggressive Behavior in Basal Cell and Basosquamous Carcinoma. *Iran. J. Pathol.* **10**, 185–191 (2015).
200. Hoesel, B. & Schmid, J. A. The complexity of NF- κ B signaling in inflammation and cancer. *Mol. Cancer* **12**, 86 (2013).
201. Bartoš, V. & Kullová, M. EXPRESSION OF ANTI-APOPTOTIC PROTEIN BCL-2 IN CUTANEOUS BASAL CELL CARCINOMA. *J. Cancer Allied Spec.* **4**, (2018).
202. Czabotar, P. E., Lessene, G., Strasser, A. & Adams, J. M. Control of apoptosis by the BCL-2 protein family: implications for physiology and therapy. *Nat. Rev. Mol. Cell Biol.* **15**, 49–63 (2014).
203. Inoue, K. *et al.* Differential expression of stem-cell-associated markers in human hair follicle epithelial cells. *Lab. Invest.* **89**, 844–856 (2009).
204. Bose, A., Teh, M.-T., Mackenzie, I. C. & Waseem, A. Keratin K15 as a Biomarker of Epidermal Stem Cells. *Int. J. Mol. Sci.* **14**, 19385–19398 (2013).
205. Cohen, P. R. Basal Cell Carcinoma with Myoepithelial Differentiation: Case Report and Literature Review. *Cureus* **10**,
206. Mentzel, T. *et al.* Cutaneous myoepithelial neoplasms: clinicopathologic and immunohistochemical study of 20 cases suggesting a continuous spectrum ranging from benign mixed tumor of the skin to cutaneous myoepithelioma and myoepithelial carcinoma. *J. Cutan. Pathol.* **30**, 294–302 (2003).
207. Xie, J. *et al.* Activating Smoothed mutations in sporadic basal-cell carcinoma. *Nature* **391**, 90–92 (1998).
208. Sandhiya, S., Melvin, G., Kumar, S. S. & Dkhar, S. A. The dawn of hedgehog inhibitors: Vismodegib. *J. Pharmacol. Pharmacother.* **4**, 4–7 (2013).
209. Ghirga, F., Mori, M. & Infante, P. Current trends in Hedgehog signaling pathway inhibition by small molecules. *Bioorg. Med. Chem. Lett.* **28**, 3131–3140 (2018).
210. Stern, R. Complicated Hyaluronan Patterns in Skin: Enlightenment by UVB? *J. Invest. Dermatol.* **127**, 512–513 (2007).
211. Budunova, I. V. *et al.* Increased expression of p50-NF-kappaB and constitutive activation of NF-kappaB transcription factors during mouse skin carcinogenesis. *Oncogene* **18**, 7423–7431 (1999).

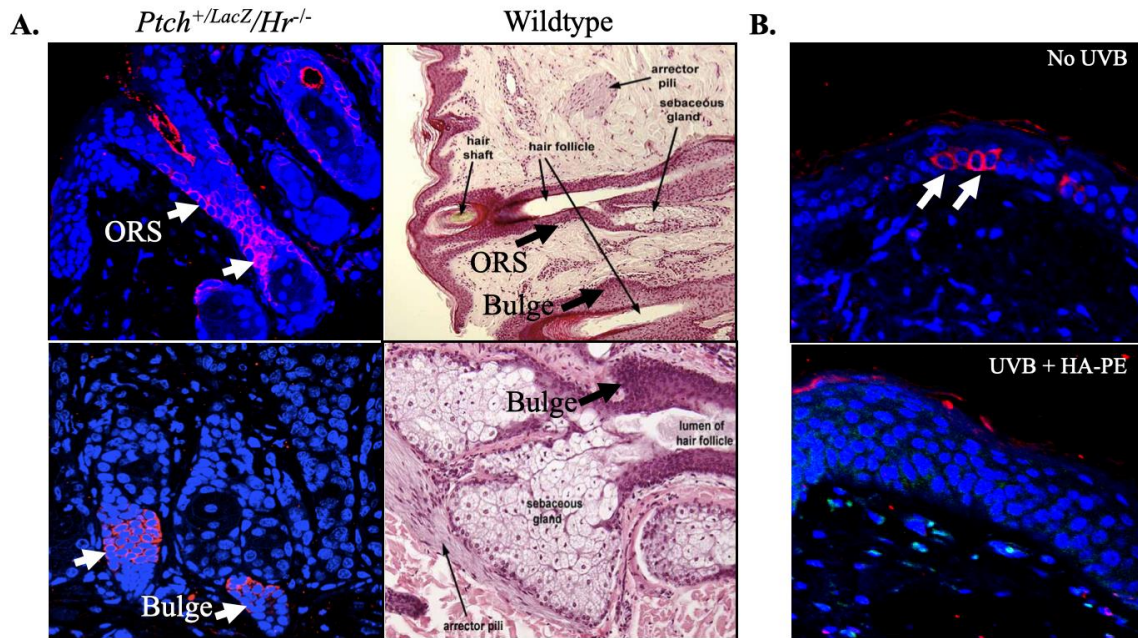
212. Chaudhary, S. C. *et al.* Shh and p50/Bcl3 signaling crosstalk drives pathogenesis of BCCs in gorlin syndrome. *Oncotarget* **6**, 36789–36814 (2015).
213. Yu, Y., Wan, Y. & Huang, C. The Biological Functions of NF- κ B1 (p50) and its Potential as an Anti-Cancer Target. *Curr. Cancer Drug Targets* **9**, 566–571 (2009).
214. Ahlqvist, K., Saamarthy, K., Syed Khaja, A. S., Bjartell, A. & Massoumi, R. Expression of Id proteins is regulated by the Bcl-3 proto-oncogene in prostate cancer. *Oncogene* **32**, 1601–1608 (2013).
215. Wakefield, A. *et al.* Bcl3 selectively promotes metastasis of ERBB2-driven mammary tumors. *Cancer Res.* **73**, 745–755 (2013).
216. Corrêa, M. de P. D., Ferreira, A. P., Gollner, Â. M., Rodrigues, M. F. & Guerra, M. C. de S. Markers expression of cell proliferation and apoptosis in basal cell carcinoma. *An. Bras. Dermatol.* **84**, 606–614 (2009).
217. Grachtchouk, M. *et al.* Basal cell carcinomas in mice arise from hair follicle stem cells and multiple epithelial progenitor populations. *J. Clin. Invest.* **121**, 1768–1781 (2011).
218. Orian-Rousseau, V. CD44 Acts as a Signaling Platform Controlling Tumor Progression and Metastasis. *Front. Immunol.* **6**, (2015).
219. Chang, G. *et al.* CD44 targets Wnt/ β -catenin pathway to mediate the proliferation of K562 cells. *Cancer Cell Int.* **13**, 117 (2013).
220. Veltri, A., Lang, C. & Lien, W.-H. Concise Review: Wnt Signaling Pathways in Skin Development and Epidermal Stem Cells. *Stem Cells Dayt. Ohio* **36**, 22–35 (2018).
221. Suzuki, K. *et al.* Embryonic hair follicle fate change by augmented beta-catenin through Shh and Bmp signaling. *Dev. Camb. Engl.* **136**, 367–372 (2009).
222. Gat, U., DasGupta, R., Degenstein, L. & Fuchs, E. De Novo hair follicle morphogenesis and hair tumors in mice expressing a truncated beta-catenin in skin. *Cell* **95**, 605–614 (1998).
223. Soukka, T. *et al.* Regulation of CD44v6-containing isoforms during proliferation of normal and malignant epithelial cells. *Cancer Res.* **57**, 2281–2289 (1997).
224. Solis, M. A. *et al.* Hyaluronan Regulates Cell Behavior: A Potential Niche Matrix for Stem Cells. *Biochem. Res. Int.* **2012**, (2012).
225. Merchant, A. & Matsui, W. Targeting Hedgehog - a Cancer Stem Cell Pathway. *Clin. Cancer Res. Off. J. Am. Assoc. Cancer Res.* **16**, 3130–3140 (2010).

226. Cochrane, C. R., Szczepny, A., Watkins, D. N. & Cain, J. E. Hedgehog Signaling in the Maintenance of Cancer Stem Cells. *Cancers* **7**, 1554–1585 (2015).
227. Riaz, S. K. *et al.* Involvement of hedgehog pathway in early onset, aggressive molecular subtypes and metastatic potential of breast cancer. *Cell Commun. Signal. CCS* **16**, 3 (2018).
228. Chang, H.-H. *et al.* Hedgehog overexpression leads to the formation of prostate cancer stem cells with metastatic property irrespective of androgen receptor expression in the mouse model. *J. Biomed. Sci.* **18**, 6 (2011).

Appendix A: Supplemental materials



Supplemental Figure 1. HA-PE on CD44 isoform expression. mRNA expression of CD44s, v4, v8, v10 were assessed through RT-PCR using primers flanking the variable region in *CD44*, and compared with the housekeeping gene GAPDH. Isoform expression of CD44v4, v8, v10 were unchanged by HA-PE application in susceptible mice after 4 weeks of UVB irradiation. Experiments described in A. and B. were repeated three times.



Supplemental Figure 2. K15-expressing bulge stem cells are not lost in disrupted hair follicles in *Ptch*^{+/LacZ}/*Hr*^{-/-} mice after 4 weeks of irradiation. **A.** K15 expression (red) in hair follicles, and; **B.** in stratum basale of control and treatment groups. All slides counterstained with DAPI (blue). In normal follicles, the outer root sheath extends past the bulge region into the hair bulb, and the bulge region is located above the sebaceous gland. The hair bulb disintegrates after the first hair cycle in *Hr*^{-/-} mice, and the bulge region is often located at the bottom of the disrupted hair follicle. However, these K15⁺ stem cells are not lost despite the disrupted morphology. Further, K15⁺ stem cells can migrate into stratum basale to participate in interfollicular epidermis renewal. However, no K15⁺ cells in stratum basale were observed in HA-PE treated group. Histology sections of wildtype epidermis are adapted from Blue Histology, University of Western Australia (<http://www.lab.anhb.uwa.edu.au/mb140/>). Arrowheads indicate the outer root sheath (ORS) and bulge region in disrupted and wildtype hair follicles.

Curriculum Vitae

Muhan Liu

EDUCATION

- 2018-2019** **Master of Science**
The University of Western Ontario, London, Ontario, Canada
- 2014-2018** **Bachelor of Medical Sciences**
The University of Western Ontario, London, Ontario, Canada

HONORS AND AWARDS

- 2019 Centre for Translational Cancer Research Travel Award (\$1,000)
- 2018-2019 Interdisciplinary Development Initiative in Stem Cells and Regenerative
Medicine Traineeship (\$10,000)
- 2018-2019 Translational Breast Cancer Research Unit Studentship (\$17,000)
- 2018 Western Graduate Research Scholarship (\$1,000)
- 2018 Inspiring Young Women in STEM – Poster Award (\$100)
- 2016 University of Tokyo Summer Internship Scholarship (\$1,300)
- 2014-2018 Western Scholars
- 2014-2018 Deans' Honor List
- 2014 Western Scholarship of Excellence (\$2,000)

RELATED WORK EXPERIENCES

- 2016 **Intern**, University of Tokyo
Project: Verification of CRISPR/Cas9 knockout system efficiency in Oryzias latipes

PUBLICATIONS

Liu, M., Tolg, C., and Turley, E. (2019). Dissecting the Dual Nature of Hyaluronan in the Tumor Microenvironment. *Front. Immunol.* *10*. 947

Truong J, **Liu M**, Tolg C, Barr M, Dai C, Raissi T, Wong E, Delyzer T, Yazdani A, Turley E. (2019) Creating a favorable micro-environment for fat grafting in a novel model of radiation induced mammary fat pad fibrosis. *Plast. Reconstr. Surg.* (accepted)

Wu J, Kim S, **Liu M**, Sabino A, Yazdani A, Turley E. (2019). Function-blocking RHAMM peptides attenuate fibrosis and promote anti-fibrotic adipokines in bleomycin-induced systemic sclerosis. *J Invest Dermatol.* (in revision)

Tolg C, **Liu, M.**, Telmer P, Alam K1, Ma J, Mendina L, McCarthy J, Morris, V, Turley, E. RHAMM regulates the timing of keratinocyte and fibroblast migration initiation during excisional wound repair by controlling ERK1,2 scaffolding. (In preparation)